Clays and Clay Minerals, Vol. 62, No. 1, 1–12, 2014.

COMPARISON OF THREE SMALL-SCALE DEVICES FOR THE INVESTIGATION OF THE ELECTRICAL CONDUCTIVITY/RESISTIVITY OF SWELLING AND OTHER CLAYS

S. KAUFHOLD[1,*], C. GRISSEMANN[2], R. DOHRMANN[1,2], M. KLINKENBERG[3], AND A. DECHER[4]

[1] BGR, Bundesanstalt für Geowissenschaften und Rohstoffe, Stilleweg 2, D-30655 Hannover, Germany
[2] LBEG, Landesamt für Bergbau, Energie und Geologie, Stilleweg 2, D-30655 Hannover, Germany
[3] Institute of Energy and Climate Research (IEK-6) – Nuclear Waste Management and Reactor Safety, Research Centre Jülich GmbH, 52425 Jülich, Germany
[4] SandB Industrial Minerals GmbH, Schmielefeldstr. 78, D-45772 Marl, Germany

Abstract—Electrical measurements are used in various fields of geoscience and technology, *e.g.* gas/oil exploration or landslide-barrier monitoring. Although clays are amongst the most conducting geomaterials their electrical properties are not yet fully understood. For example, in a recent high-level-radioactive-waste repository large-scale test, a bentonite barrier was monitored geoelectrically. To facilitate interpretation of the results, the reasons for the observed differences in the electrical conductivity must be understood (*e.g.* changes in water content, temperature, salinity of pore water, *etc.*). To improve understanding of the electrical properties of clay minerals, *in situ* measurements must be combined with laboratory measurements. *In situ* measurements allow the characterization of the material in its natural state and laboratory measurements, for small sample amounts, allow the user to vary relevant parameters systematically such as water content, temperature, the salinity of the pore water, or even the cation population if swelling clay minerals are present. *In situ* measurements using different electrode distances, from m to cm range, proved that small-scale investigations are essential because of small-scale material heterogeneities. In the laboratory, all the relevant parameters mentioned above can be controlled more easily for small sample amounts. In the present study three different small-scale devices (SSM1–SSM3) were compared. The geometry factor, *K*, was determined both by calculation and by a calibration against solutions of different conductivity. Calculated and measured geometry factors were in good agreement. SSM1 and SSM2 – both with four pin-shaped electrodes – were found to be particularly applicable for *in situ* measurements. SSM2, with point contacts at the tips of the pins, was considered to be an improvement over SSM1 because the effects of both water content and temperature gradients (which are particularly relevant near the surface) were less pronounced using SSM2. SSM3, in which the contacts are placed at the bottom of a 4.5 mL trough, proved to be useful when systematically varying all of the parameters influencing the electrical properties in the laboratory.

Key Words—Electrical Conductivity of Clays, Electrical Resistivity of Clays, Smectite, Swelling Clay Minerals, Bentonite.

INTRODUCTION

Measurement of the electrical properties of clays is used in various fields of science and technology. As an example, electrical measurements are made for gas/oil exploration in drill holes. The electrical properties are also used for exploration of clay raw materials and water resources.

The electrical conductivity (*EC* = 1/electrical resistivity, *ER*) of clays is known to depend on 'volume conductivity' (≈water content) and 'surface conductivity' (≈diffuse double layer, DDL). The total electrical conductivity depends, therefore, on the DDL and the arrangement of clay-mineral particles in relation to each other (Tabbagh and Cosenza, 2006; Mojid and Cho, 2006; Garcia and Bazán, 2009).

* E-mail address of corresponding author:
s.kaufhold@bgr.de
DOI: 10.1346/CCMN.2014.0620101

Amongst all the clay minerals, swelling clay minerals (smectites) are known to play a special role in the electrical properties of clays and soils (Waxman and Smits, 1968). Their contribution to electrical conductivity is attributed to the mobility of the exchangeable cations in the interlayer. The tangential mobility (within the interlayer) of the exchangeable cations has been reported by many studies, *e.g.* Weiler and Chaussidon (1968) and Ishida *et al.* (2000). The reasons for differences in the electrical properties of clay minerals and clayey materials, however, are not yet fully understood (*e.g.* Kaufhold and Penner, 2006). For example, little is known about the effect of the variability of clay minerals (particle size, charge distribution, chemical composition, partly soluble admixtures, microstructure, *etc.*) on the electrical properties. The layer-charge density (Lagaly, 1994), the smectite content (Kaufhold *et al.*, 2002), the variable charge (Kaufhold and Dohrmann, 2013), and the cation exchange capacity (CEC) probably have an influence also.

To fill this gap, the differences in the electrical properties of clays need to be studied under well defined conditions which can be provided by a small-scale laboratory device allowing parameters to be varied, including water content, temperature, salinity of the pore water, texture, and type of clay mineral. For example, Taioli *et al.* (2006) published a report on a small-scale laboratory device but admitted that it may not be applicable to clay minerals and/or clayey soils. On the other hand, the electrical properties can be measured *in situ* in a flow-through cell to investigate the effect of permeation of solutions. Examples of such devices were presented by Slater and Lesmes (2002) and Binley *et al.* (1996).

Large- and medium-scale *in situ* or field measurements of the electrical properties are conducted routinely either by logging in a bore hole or at the surface. In both cases either galvanic methods (direct contacts) or inductive methods can be used, as described by Schulmeister *et al.* (2003). An electrode device was developed (Veris® 3100, Veris Technologies, Salina, Kansas, USA) which can be towed by a car or by hand for mapping soils. The inductive EM38 device (Geonics Ltd, Mississauga, Ontario, Canada) can be used for situations involving approximately the same scale. Both devices provide comparable values (Suddeth *et al.*, 1999). The heterogeneity of clays in the open pit is commonly on a smaller scale, however. A small-scale investigation of the electrical properties of soils (Igel, 2007) addressed the analytical challenges resulting from the small scale.

The aim of the present study was to assess the applicability of three different small-scale devices with respect to the systematic investigation of the electrical properties, both *in situ* and in the laboratory.

GEOELECTRICAL BACKGROUND

All electrical measurements of geomaterials (rocks, stones, *etc.*) require a minimum of four electrodes. Two of them, usually labeled A and B (or C1 and C2), respectively, are used to insert a current into the material to be investigated. The other two, labeled M and N (or P1 and P2, respectively) probe the resulting potential difference (voltage). For small-scale measurements, the current needs to be small to avoid overstressing the resistivity meter but also to prevent unwanted heating or electrochemical reactions at the electrode−soil/clay interfaces. The resistivity/conductivity of the material results from the relations illustrated in equations 1 and 1a.

$$ER\ [\Omega\text{m}] = K\ [\text{m}]\cdot U_{\text{MN}}\ [\mu\text{V}]/I_{\text{AB}}[\mu\text{A}] \quad (1)$$

$$EC\ [\text{S/m}] = 1/ER = 1/K\cdot I/U \quad (1a)$$

The factor K depends only on the geometry of the measurement device and is, therefore, referred to as a 'geometry' or 'configuration' factor; it has units of m. The K factor must be determined for each measurement device, calculated based on either the geometry or calibrated by materials of known resistivity, *e.g.* salt solutions.

The K factor for four-point electrodes placed at the surface of an infinite half space depends only on the distances r_i between the current electrodes and the potential electrodes (equation 2; *e.g.* Telford *et al.*, 1976). An infinite half space is the earth below when standing on the ground and a full space exists when buried deep in the ground with earth above and beneath.

$$K_{\text{half-space}} = 2\pi/(1/r_{\text{AM}} - 1/r_{\text{AN}} - 1/r_{\text{BM}} + 1/r_{\text{BN}}) \quad (2)$$

In the present study, the Wenner arrangement was used which means that all electrodes were arranged linearly with equal distances. In this case equation 2 is reduced to equation 3

$$K_{\text{half-space}} = 2\pi a \quad (3)$$

where a is the distance between electrodes (cm)

Equations 2 and 3 are valid for point electrodes, which means that the insertion depths of the electrodes are much smaller than the distance between them. This condition is rarely fulfilled in the case of small-scale arrangements.

If point-shaped electrodes are not placed at the surface but at a certain depth, t, then the geometry factor depends on both the separation a and the depth t and the following equation (4) can be used:

$$k(a,t) = 4\pi/\left[1/a + 2/\sqrt{a^2+4t^2} - 1/\sqrt{a^2+t^2}\right] \quad (4)$$

MATERIALS AND METHODS

To measure the electric resistivity (*ER*)/electrical conductivity (*EC*) the '4-Punkt-light' measurement device, developed and distributed by Dipl. Geol. E. Lippmann (LGM company, D-94571 Schaufling, Germany), was used. The electrical current is adjusted to 0.1, 1, or 10 μA and the resulting voltage (in μV) of both of the inner electrodes (M, N) is displayed. The measurements are conducted at a constant frequency of ~10 Hz.

Small-scale *in situ* electrical measurements were conducted in several German open pits with different types of clay: Bentonite (Hallertau, Bavaria: Kaufhold *et al.*, 2003), ceramic clay (Westerwald, Rhineland-Palatinate: Kaufhold and Penner, 2006), and marine (brick) clay (Sarstedt and Vöhrum, Lower Saxony and Friedland, Mecklenburg-Western Pomerania).

Samples of each of the different clays were collected at the exact point of measurement and sealed carefully in plastic bags to determine the water content by oven drying at 105ºC in the laboratory. In addition, the smectite content was determined either based on CEC data (Meier and Kahr, 1999) or by the methylene-blue

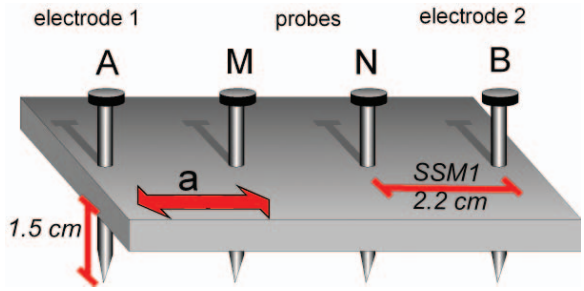

Figure 1. Schematic representation of the small-scale Wenner arrangement SSM1.

method. Both methods should be considered critically as discussed by Kaufhold and Dohrmann (2003).

Three different devices were used and are described below.

SSM1 (small-scale measurement device 1)

The first small-scale, *in situ* measurements were conducted to compare the electrical properties of bentonites with their mineralogical composition, *i.e.* the smectite content (Kaufhold *et al.*, 1998, 2003; DE 19839531). The aim was to use the data for quality control in bentonite mining. Measurements were performed in the open pits (*in situ*) on fresh and on smooth surfaces. The partially dried surfaces were removed with a shovel and measurements were performed quickly (within 1 min) to avoid drying effects. The temperature was recorded simultaneously. The electrodes were arranged according to Wenner, as described above (Figure 1). The distance between electrodes (a) was varied from 30 to 2 cm. The 2 cm device was termed SSM1; data shown in the present study were measured with a = 2.2 cm.

In a first approach, the distance between the electrodes (a) was 30 cm. This device was not applicable in the clay open pits because of: (1) the heterogeneity of the clay in this scale (cm−dm); (2) the difficulty in producing an even surface; and (3) the unavoidable occurrence of cracks between the electrodes. Therefore, a was decreased. In a second approach, a was varied from 2 to 6 cm (Figure 2). In this case the point electrode condition was obviously not fulfilled and the mutual interference between the electrodes was taken into account by calculating an appropriate K factor. Appropriate K factors for small-scale measurements were used, making use of a theorem of electrostatics which allows the user to approximate the electric field of a thin stick by the known electric field of an elongated half-ellipsoid, as derived by Igel (2007). His solution requires the numerical solution of an elliptical integral. Rücker and Günther (2011) developed an even more versatile 'Finite-Element' approach, which enables the model calculation of virtually any shape of the electrodes. The application requires intensive computer resources. According to Rücker and Günther (2011) however, the K factor of the complete electrode model of cylindrical electrodes is met quite closely by the K factor of point electrodes placed at a depth of ~60% of the length of the actual electrodes. Equation 4 with $t = 0.6 \cdot L$ was used to calculate the K factors of SSM1 (L = length of the electrode).

The curves (Figure 2) show a slight increase in ER depending on the distance between the electrodes, which may be related to near-surface material heterogeneities or vertically variable parameters such as temperature and/or humidity. Interestingly, curves of different shapes were observed. In some cases, perfect linears were observed but some curves, particularly of open pit 2,

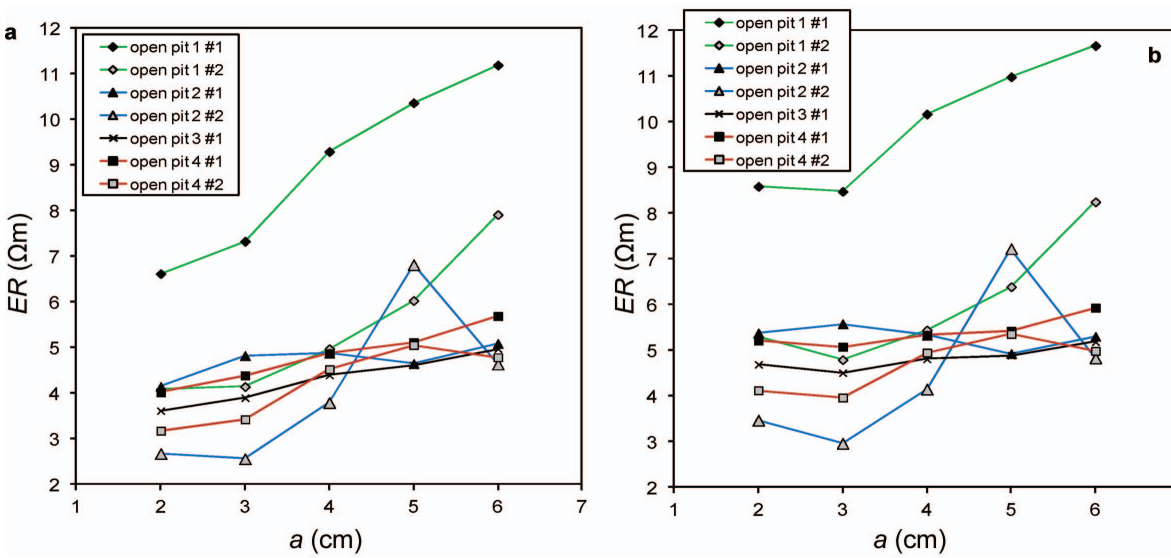

Figure 2. Dependence of apparent electrical resistivity (ER) of Bavarian bentonites on the distance of electrodes before (a) and after (b) K factor correction.

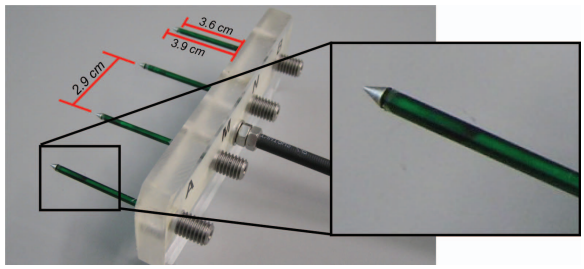

Figure 3. Photograph of the alternative device (SSM2) with real point electrodes (a = 2.9 cm).

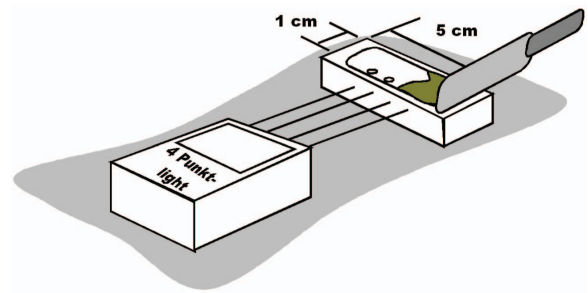

Figure 5. Schematic representation of the 4.5 mL small-scale laboratory measurement device (SSM3). The clay is smeared into the trough using a spatula.

indicated the lateral heterogeneity of the clay even on a small scale. Therefore, the smallest reasonable scale was selected. A distance (a) of 2 cm results in a length of the measured area of 6−10 cm and collecting the material which was penetrated by the electrodes results in a sample mass of 10−20 g, which is a typical amount of clay sample used in the laboratory for characterization after homogenization by grinding. Technically, a, the distance between the electrodes, may be decreased, but this would involve distances smaller than that commonly used in the laboratory. The distance between the electrodes and probes (a) should, therefore, be ~2 cm and for practical reasons was fixed at 2.2 cm.

SSM2 (small-scale measurement device 2)

Because of the lack of real point electrodes of SSM1 (Figure 1 and discussion thereafter), a different device was tested (Figure 3). The cylindrical part of the electrodes was surrounded by insulating plastic and only the tip of the electrode was in contact with the clay.

The conducting tips of the electrodes of SSM2 were intended to be surrounded entirely by rock to simulate point electrodes. The depth of the point electrodes of SSM2 was ~3.75 cm (average depth of the conductive pin). To calculate the K factor of SSM2, both the variable a and the depth t must be considered (according to equation 4). For a given electrode a, the K factor increases with depth of submersion of the point electrodes (Figure 4). For t = 0, the factor starts with the 'half space' value $K_0 = 2\pi a$ and at depths $t >> a$ it reaches the upper limit of the 'full space' value $K_\mu = 4\pi a$.

For measurements using SSM2 with a = 2.9 cm and t = 3.75 cm, the calculated geometry factor was K_{SSM2} = 0.328 m.

SSM3 (small-scale measurement device 3)

To investigate systematically the correlation of clay properties with electrical parameters, a further small-scale measurement device was developed in the shape of a small trough (Figure 5). To measure the electrical properties, the sample must be ductile (plastic) because it is smeared on the electrodes which are arranged at the bottom of the small trough (4.5 mL). The trough was made of insulating plastic, the electrodes were of steel and arranged according to Wenner. Care must be taken with respect to drying after smearing the clay gel in the trough. The measurements were performed quickly enough that no significant drying had occurred. Smearing the gel into the trough took ~5 s and after a few more seconds a stable value was obtained, noted, and ~1 mL of the material was used to determine the water content by oven drying (a dried and weighed cup

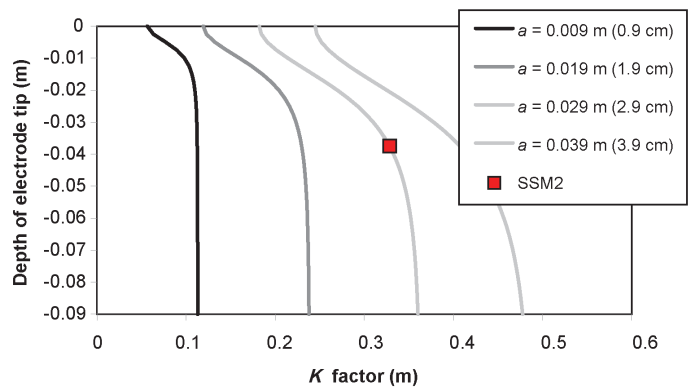

Figure 4. Calculation of the K factor for different electrode separation distances, a, and depths, t. The square represents the SSM2 parameters (a = 2.9, t = 3.75 cm).

was waiting on the nearby balance). The temperature was also a crucial factor influencing the electrical conductivity. All materials and the measurement devices were, therefore, carried out in a laboratory with constant temperature (22ºC).

The *K* factor of SSM3 could not be calculated because of the complex geometry. It deviates in two senses from the idealized point solution of equation 3: (1) the electrode buttons are not small compared to the electrode distance; and (2) the small volume of the trough imparts notable boundary conditions instead of the infinite half space.

Although the effect of this complex geometry could, in principle, be treated by a 'Finite-Element' modeling procedure, the best way to determine the applicable *K* factor in this case is experimental calibration with liquids of well known conductivities.

Calibration

The *K* factor can be calculated but ideally is determined empirically by calibration. To calibrate, a set of different solutions with different ionic strengths was used. SSM3 was calibrated with 4.5 mL of each solution but investigating the solutions with SSM1 and SSM2 turned out to be a challenge. In a first approach, a 5 L cup containing the different solutions was used and the electrodes were inserted as in a clay or soil. However, the ratio of the results of parallel measurements with all three SSMs obtained in the laboratory did not match with the ratio obtained from parallel measurements in the open pits (real half space). Therefore, in a second attempt, a 70 L vessel with 50 L of the different solutions was used and was adequate. The distance of the measurement location in the water bath to the walls was 25 cm and the distance to the bottom was ~35 cm. These distances were required to mimic a real half space. The room temperature was 22ºC and the temperature of the solutions was 25ºC. The reference conductivity of the solutions was measured with a calibrated laboratory conductivity meter (conductometer HI 9033 HANNA) which is applicable for solutions. The laboratory calibration started with tap water (commonly 18 Ωm as confirmed by the reference conductivity meter). As explained above the M-N voltage was measured with all devices and the reference value (measured with the conductivity meter) was also recorded. Different ionic strengths were adjusted by adding a defined amount of NaCl. All data are summarized in Table 1 and the calibrations are given in Figure 6. The pure water value measured with SSM3 was expected to be affected by traces of clay and salt on the surface of the plastic trough. These traces could not be removed by washing and so this value was not considered in the determination of the calibration factor.

The *K* factors for SSM1 and SSM2 were calculated based on equation 4. In the case of SSM1, with $a = 2.2$ cm and $L = 1.6$ cm, the equivalent depth of point electrodes

Table 1. Raw data and calculated calibrations for all three devices.

50 L lab. water	*T* (ºC) 25	Conductometer [µS/cm]	Conductometer [mS/m]	Conductometer [Ωm]	SSM1 (10^4 nA) [µV]	SSM1 (10^4 nA) [V/A]	SSM1 (10^4 nA) *K* [m]	SSM2 (10^4 nA) [µV]	SSM2 (10^4 nA) [V/A]	SSM2 (10^4 nA) *K* [m]	SSM3 (10^2 nA) [µV]	SSM3 (10^2 nA) [V/A]	SSM3 (10^2 nA) *K* [m]
0.02 mol/L (58 g NaCl/50 L)	25	531	53.1	18.8	946	94.6	0.20	547	54.7	0.34	543	5430	0.0035
0.04 mol/L (+58 g NaCl/50 L)	25	2880	288	3.5	193	19.3	0.18	105	10.5	0.33	136	1360	0.0026
0.06 mol/L (+58 g NaCl/50 L)	25	5030	503	2.0	115	11.5	0.17	61	6.1	0.33	84	840	0.0024
0.1 mol/L (+116 g NaCl/50 L)	25	7015	701.5	1.4	77.2	7.72	0.18	42.5	4.25	0.34	55.7	557	0.0026
0.2 mol/L (+290 g NaCl/50 L)	25	11240	1124	0.9	51.9	5.19	0.17	27.4	2.74	0.32	33.8	338	0.0026
	25	22000	2200	0.5	27.5	2.75	0.17	14.8	1.48	0.31	18.6	186	0.0024

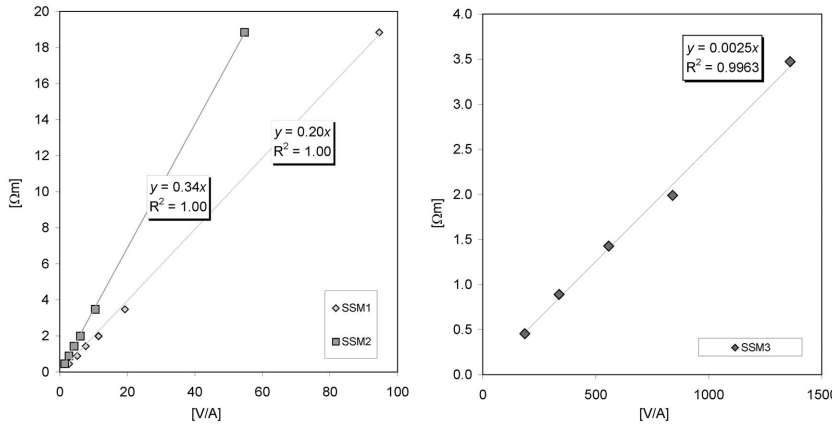

Figure 6. Calibration curves of all three devices.

becomes t = 0.96 cm and the calculated result is K_{SSM1} = 0.174 m. This corrected value is ~26% greater than the improper surface-point electrode approximation from equation 2. The experimental calibration of SSM1 (Table 1 and Figure 6) correspondingly yields K = 0.18 m (average value) and K = 0.20 m (derived from the slope in Figure 6), thus confirming the approximation algorithm. For SSM2, the calculated K value (0.33 m) was in particularly good agreement with the 0.34 m value determined empirically, probably because of the presence of point electrodes which are easier to consider quantitatively. This does not apply to the calibration point measured for tap water (the largest *ER*), which in all cases fails to follow exactly the trend evident from the other calibration points.

The K value of SSM3, however, due to the even more complex geometry, would be much more difficult to calculate and hence had to be determined empirically (0.0025 m).

In addition to the different solutions, clays or soils could also have been used for calibration. This could be important because of the different interface of the electrodes and the water compared to the electrodes and a solid (clay or soil). Theoretically, the K factor should depend only on the geometry. Strong evidence in support of the validity of the K factors determined with the solutions is the fact that the ratios of the values determined with all small-scale devices do not depend on whether a solid or a liquid is measured. In different open pits all three SSMs were used to measure the voltage necessary to maintain a specific current (*e.g.* 10 μA). The ratios of these values of the different SSMs were in good agreement with the ratios of the voltages determined in the solutions (which are listed in Table 1). No other materials were, therefore, needed as references.

RESULTS AND DISCUSSION

In situ measurements with SSM1 and SSM2

The plan was to use both devices for *in situ* determination of the electrical properties in open pits. SSM1 was used by Kaufhold *et al.* (1998) and Kaufhold *et al*. (2003) for the investigation of more than 200 different Bavarian bentonites. Based on these measurements, an empirical relation between *ER*, water content, and temperature and in turn a complementary method for quality control were established. Later, investigations of the Westerwald ceramic clays also proved a strong correlation between the *ER*/water content ratio and the CEC (smectite and smectitic layers content in mixed-layer minerals: Kaufhold and Penner, 2006). The clays in the present study, however, are dominated by low-CEC clay minerals (kaolinite, illite), which provide a more or less CEC-independent contribution to conductivity which explains the slightly lower *ER* values compared to the CEC and water content of the Bavarian bentonites (Kaufhold and Penner, 2006). The disadvantage of this method, however, is that a fresh surface has to be produced because the water content of the bentonite at the surface is smaller than within or even decreases during the measurements. Moreover, the temperature is known to affect the measurement and the temperature gradient is significant near the surface. Note, for quality-control purposes, no measurements of surfaces exposed to the sun were taken. These problems can be overcome to some degree by using device SSM2 because of the distance of the clay volume determining the electrical signal from both gradients (water content and temperature). To test both methods and investigate the compatibility, parallel measurements were conducted in different clay open pits (Figure 7).

Both devices (SSM1 + SSM2) are applicable in clay open pits with plastic/ductile clay. Note that neither can be used in the case of clayey material containing a network of small calcite or gypsum veins because these veins isolate the conducting clay. Such circumstances were found in some of the bentonite mines of Milos, Greece, but generally are rare. In principle, both devices could have been used as a reference measurement device for the present study. A typical measurement scenario is shown in Figure 8. Note that the temperature was also recorded to enable further interpretation of the data.

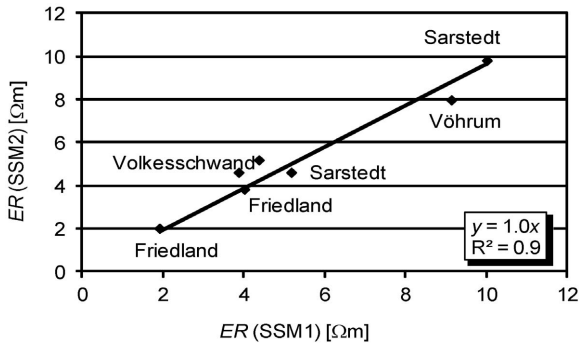

Figure 7. Comparison of SSM1 and SSM2 by means of seven parallel measurements in four different clay deposits.

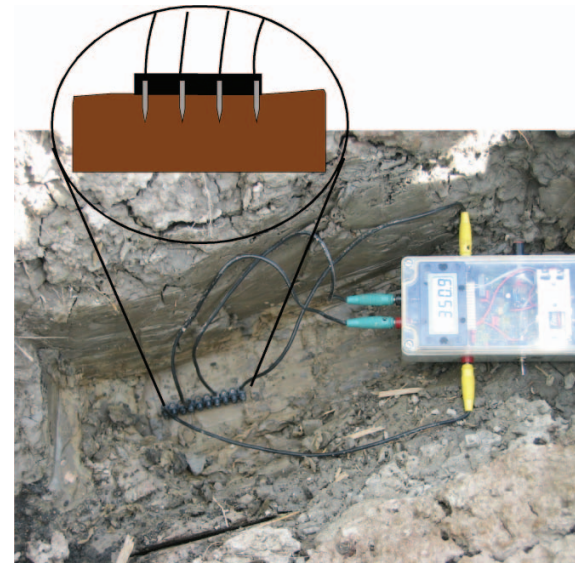

Figure 8. *In situ* measurement of electrical properties using the SSM1 device. At the same location, samples were also taken to determine water content and the temperature was measured.

Laboratory measurements with SSM3

The electrical properties of clays are known to depend on the water content, among other parameters (including the CEC). The small-scale laboratory device SSM3 permits investigation of this relation over a wide range of water contents (Figure 9). The water content (Figure 9) represents the so called 'mineralogical water content' (mass of water desorbed by drying compared to the initial total mass). Accordingly, a common clay with 90 wt.% water is a suspension (90 wt.% = 90 g water and 10 g clay). The 'technical water content' of this suspension would be 900%. Comparing literature data, the type of water content must be considered. To record the curves, the clays were mixed with excess water first. Values representing different water contents were then recorded stepwise and by slow drying of the clay gels and smearing them into the 4.5 mL plastic trough (SSM3). Therefore, the curves are discussed starting with large water contents and proceeding to smaller values. The curves shown (Figure 9) can be subdivided into three branches and these may be explained by the schematic model shown in Figure 10. The first branch, at large water contents (roughly >70 wt.%), reflects the electrical properties of a clay suspension which differs from a gel in that water forms the matrix and the clay particles are dispersed in the water matrix. At water contents of <60 wt.% (in most cases a clay gel) the properties start to depend on the clay particle interactions (and contacts) because the clay particles are expected to form the matrix (percolation theory; *e.g.* Kesten, 2006). For water contents of 30 to 60 wt.% a linear electrical conductivity range was observed (2nd branch). Because the conductivity–water relation is apparently linear in this range, considering the conductivity rather than the resistivity is reasonable. Note that in this linear range the electrical conductivity only increases if the conductivity of the pore water is significantly less than the conductivity of the clay minerals. In turn the electrical conductivity increases because (1) the smaller amount of (electrolyte poor)

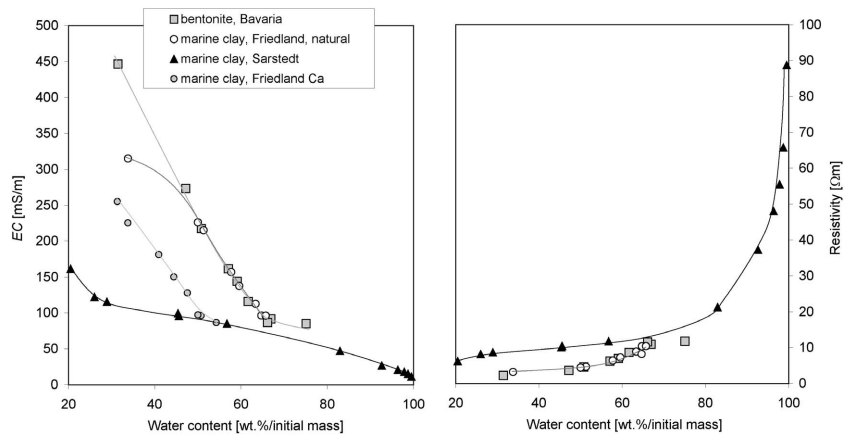

Figure 9. Dependence of the electrical conductivity and electrical resistivity on the water content of three different clays. The Friedland clay was investigated in its natural form (Na^+) and after exchange of the Na^+ by Ca^{2+}.

water and the larger amount of clay minerals and (2) the increased number of clay-particle bridges. Each clay reaches the plastic limit (at an individual water content) and hence cannot be smeared further without the formation of cracks and/or voids. These values were not considered further but represent the 3rd branch. No values are presented because of the macroscopically evident occurrence of cracks. The electrical properties would then depend more on the compaction caused by smearing the clay than on material properties. The maximum electrical conductivity is expected to correspond to water saturation.

Examination of the water content (*WC*)–*EC* curves obtained by SSM3 actually allows for the comparison of the *EC* values of different clays, *e.g.* the marine Friedland clay with bentonite from Bavaria. Interestingly, the natural Friedland marine clay had a larger *EC* value than the bentonite even though it had a significantly smaller CEC (Friedland = 30 meq/100 g, bentonite = 70 meq/100 g). According to Waxman and Smits (1968) the CEC is expected to affect the *EC* significantly. If CEC is to be the dominant factor then the bentonites should have shown much larger *EC* values than the Friedland clay. This unexpected result may be due at least partly to the type of exchangeable cation. The smectites (free smectite + smectitic layers of mixed-layer minerals) of the Friedland clay were dominated by exchangeable sodium, which contributes significantly to electrical conductivity because of the larger mobility of the Na^+ compared to Ca^{2+} and likewise the fact that more cations are present in the case of Na^+ in the interlayer (two permanent negative clay charges are compensated either by one Ca^{2+} or two Na^+ cations). After Ca^{2+} exchange of the Friedland smectites an electrical conductivity was observed as expected (less than that of the bentonite which is commonly dominated by Ca^{2+} and Mg^{2+}).

The aim of most of the measurements of the electrical properties is to rank different materials according to their conductivity or resistivity. The data presented (Figure 9) reinforces the idea that such a ranking cannot be made without defining a reference water content. For example, the Bavarian bentonite had a smaller conductivity value at 60 wt.% water than the Sarstedt clay at 20 wt.% water. Note that in the field, *i.e.* in a drill core or an open pit, the water content of the clays may vary depending on the ambient conditions.

To improve the comparability of the conductivity of different clays, defining a constant reference water content (*e.g.* 50 wt.%) or stating the slope or the *y* intercept of the linear part is suggested (Figure 10).

SSM3 could also be used in the open pit, although this may not be necessary. Regardless, to further test the applicability of this device, parallel measurements were performed with SSM1 and SSM3 in three different clay open pits (Figure 11).

First, SSM1 was used. Then, the plastic clay was smeared into SSM3 and the resistivity was measured.

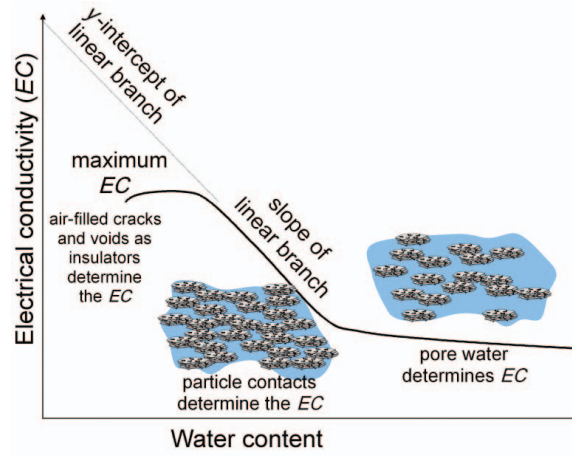

Figure 10. Model explaining the typical *WC–EC* curve of clays.

Finally, a sample was collected and sealed carefully for water-content determination in the laboratory.

A satisfying correlation was found (Figure 11) which proves the applicability of SSM3 for both *in situ* and laboratory investigations. However, the resistivities obtained with SSM3 were systematically larger than those measured with SSM1. This may be explained by the fact that smearing the mostly relatively dry materials leaves some voids which causes an increase in the resistivity. Therefore, SSM1 and SSM2 are preferred for *in situ* measurements.

Parameters influencing the electrical properties

The dependence of the electrical properties on the water content has been explained above. The *WC-EC* curves recorded with SSM3 were obtained by drying a clay gel or a suspension. The pore-water composition

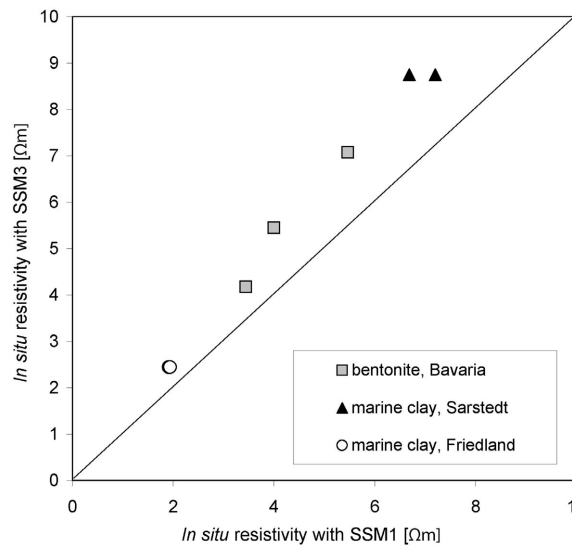

Figure 11. Comparison of the results of SSM1 and SSM3 when applied *in situ*.

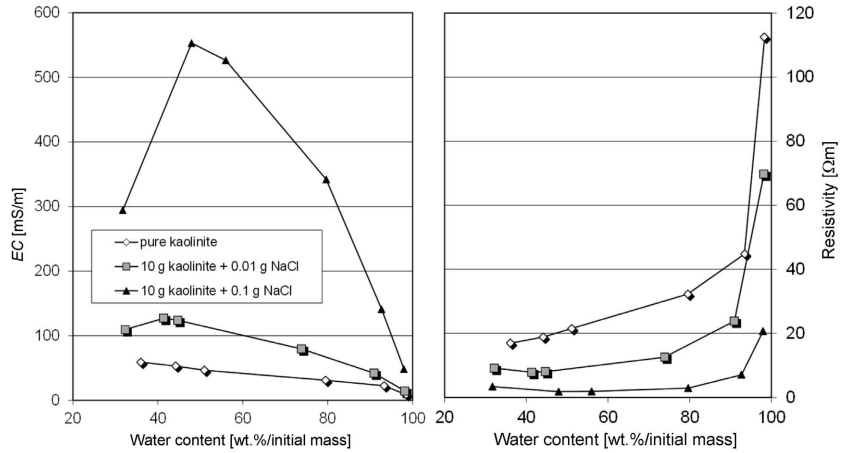

Figure 12. SSM3 measurements of the electrical properties of kaolinite to study the effect of soluble minerals.

and in turn the volume conductivity were, therefore, variable. For soils or sediments, however, a constant salinity of the pore water is commonly considered. This should not reflect reality because in a clay or clayey sediment a certain amount of soluble minerals is present and the amount of water depends on external factors (*e.g.* humidity, rainfall, groundwater level, *etc.*). Hence, the water-soluble minor component ratio is variable and determines the volume conductivity. To assume a certain type and amount of soluble mineral in the sample is more realistic (*e.g.* 0.1 wt.% NaCl, 1 wt.% calcite, *etc.*). In the case where carbonates and/or gypsum, which are partly soluble in water, are present, the pore-water composition depending on the variable water content is even more complex because the pore-water composition depends on the solid/liquid ratio. In turn, this determines the amount of soluble carbonate/gypsum. On the other hand, using the small-scale laboratory device also allows measurement of the *WC–EC* curve with constant electrical conductivity of the pore water. In this case, different suspensions, gels, or dry pastes must be prepared using different amounts of one solution. This was not investigated in the present study, however. Instead, the *WC-EC* curves of kaolinite with different amounts of soluble phases (model substance halite) were measured (Figure 12).

A further example of the usefulness of different small-scale devices is the investigation of the effect of preferred orientation (texture) of clays on the anisotropy of the electrical properties. In four open pits (Westerwald, Bavaria, Friedland, Sarstedt), measurements were performed both perpendicular and parallel to the bedding (Figure 13). At Westerwald, Bavaria, and Friedland no differences between perpendicular and parallel measurement results were observed. The clay minerals of these materials, therefore, were believed to be arranged more or less randomly and fine bedding was assumed to be absent.

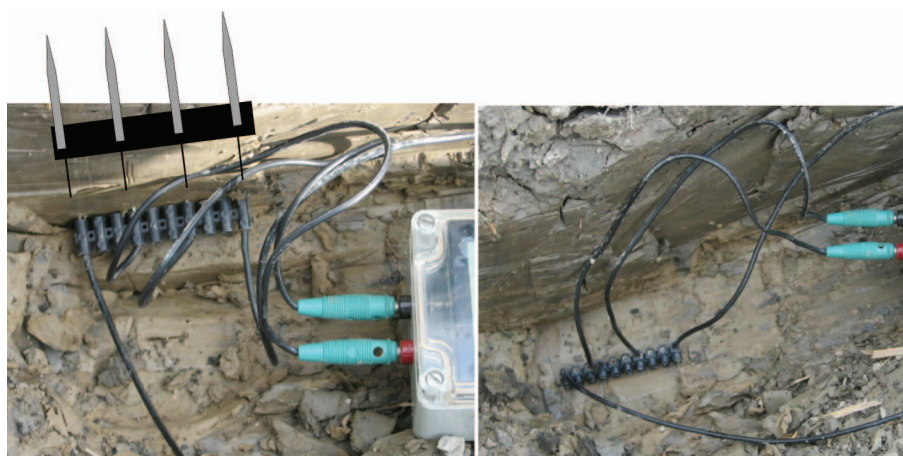

Figure 13. Photographs of parallel and perpendicular *ER* measurements using SSM1.

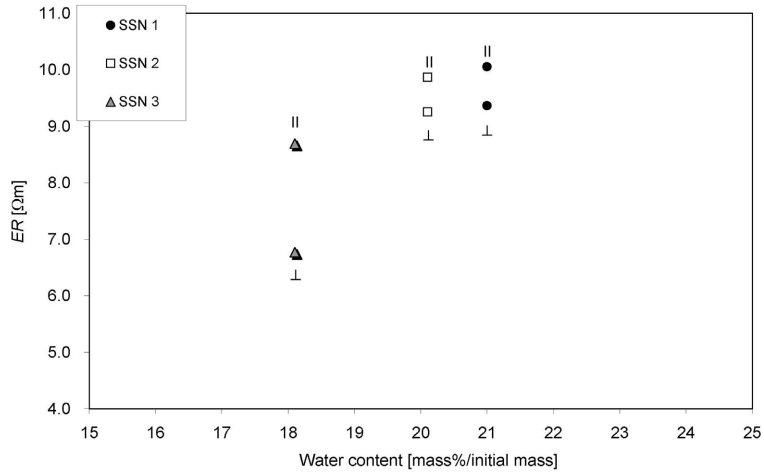

Figure 14. Investigation of the anisotropy of electrical properties at three sites in the Sarstedt clay deposit.

At the Sarstedt site, however, where macroscopically visible fine bedding occurs, the electrical behavior was different. A larger *EC* value was found when measuring perpendicular to the bedding (Figure 14). No proven explanation can be provided for this observation and further detailed investigations using SSM1 and SSM3 are required. Various interpretations are offered in the schematic Figure 15. On one hand, the insertion of electrodes parallel to bedding may cause some cracks because clays are known to break mainly parallel to the bedding. On the other hand, vertical insertion of the electrodes compresses the layers and might be expected to cause fewer microcracks.

Based on the assumption of fine bedding, the results observed may also be explained by the electrical short cut of layers with different conductivity in the case of perpendicular electrodes. This second model assumes that the fine bedding consists of a mixed layering of conducting (clay-rich) and more isolating layers (carbonate or quartz-rich), which is common in sediments. In the case of parallel insertion of the electrodes, the carbonate/quartz-rich layers would, to a certain extent, isolate the layer in which the electrodes are present. In contrast, electrodes inserted perpendicularly would shortcut the different conducting layers and, in a way, bridge the isolating layers. Most of the differences observed were not large (<1 Ωm) and different mechanisms are assumed to play different roles. Identification of the exact cause of these differences requires additional systematic investigations, ideally using SSM1 and SSM2, because the connecting effect would be small in the case of the second explanation and SSM2.

SUMMARY AND CONCLUSIONS

Three different small-scale devices (SSM1, SSM2, SSM3) were compared with respect to their applicability for both *in situ* and laboratory measurements of the electrical properties of clays. All devices were based on the Wenner arrangement and measurements were conducted with the '4-Punkt-light' apparatus. Variation of the electrodes and probes proved that a suitable distance, *a*, was ~2 cm (for technical reasons 2.2 cm was used). The volume determining the electrical properties in this case corresponded to the typical amount of clay sample investigated in the laboratory (after homogenization).

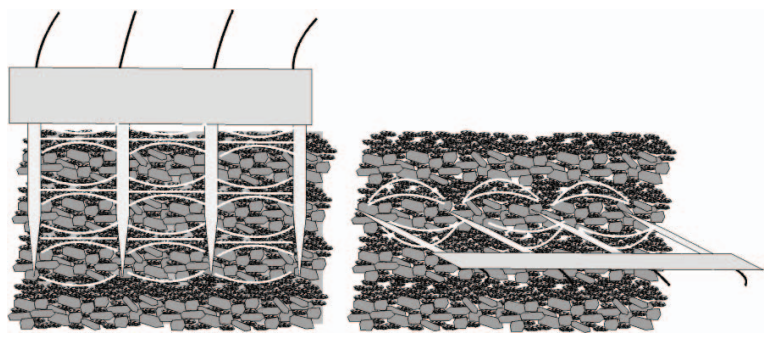

Figure 15. Model to explain the differences in parallel and perpendicular measurements.

The comparability of EC values measured *in situ* with parameters derived in the laboratory, such as the smectite content or CEC, is guaranteed. All three devices were calibrated against the same set of aqueous solutions. Interestingly, a volume of 50 L was required for the calibration tank in order to impede boundary effects from the walls. Using a 5 L tank only resulted in a different ratio of the electrical signals derived from the different devices compared to the ratio measured *in situ* with an infinite half space. Parallel to the experimental calibration, the *K* factors of SSM1 and SSM2 could be calculated analytically based on their geometry. Devices 1 and 2 were particularly applicable for *in situ* measurements whereas SSM3 was advantageous in the laboratory for the systematic investigation of some parameters affecting the *EC* of clays. SSM1 was used for complementary quality control throughout bentonite mining. One concern using this device was the direction of electrode insertion (parallel or perpendicular to bedding). Accordingly, in all open pits investigated in the present study, measurements were performed both parallel and perpendicular to the bedding. Only in one brick clay deposit (Lower Cretaceous clay in N. Germany, Sarstedt) was a significant difference observed. This requires further investigation. SSM2, with actual point electrodes, was considered to be an improvement over SSM1 because water content and temperature gradients which are particularly relevant near the surface were less pronounced using this device. SSM3, on the other hand, proved to be useful at recording the water content–electrical conductivity relation (*WC-EC* curves). All the clays investigated showed increasing *EC* (decreasing resistivity) with decreasing water content. Below water saturation of the clay, the *EC* values dropped because of the formation of cracks and voids. The curves measured suggested that comparisons of the *EC* values for different clays requires consideration of either a reference water content or, even better, the slope of the linear branch of the *WC-EC* curves. The effect of soluble phases (as minor constituents of the clays), which depend on the degree of drying and which determine the pore-water conductivity, was measured. Most of the clays were expected to contain <0.1 wt.% halite. Assuming a variable pore-water composition which can be described by the content of soluble phases (*e.g.* halite) in the dry state was more realistic than assuming a constant pore-water composition because the amount of water in soils and in sediments depends on the ambient conditions and, hence, is variable. Future work will be devoted to understanding the reasons for differences in the electrical properties of clays. The results of the present study (*e.g.* Friedland clay *vs*. bentonite) proved that the Waxman and Smits equation (Waxman and Smits, 1968) may be useful to explain the difference between sand, silt, and clay, but not to explain the differences between different clays.

ACKNOWLEDGMENTS

The authors are grateful to all the companies which allowed the investigation of their materials: SandB industrial minerals, WBB Fuchs GmbH and Co. KG, Theodor-Stephan KG, and Friedland industrial minerals.

REFERENCES

Binley, A., Henry-Poulter, S., and Shaw, B. (1996) Examination of solute transport in an undisturbed soil column using electrical resistance tomography. *Water Resources Research*, **32**, 763–769.

Garcia, N.J. and Bazán, J.C. (2009) Electrical conductivity of montmorillonite as a function of relative humidity: La-montmorillonite. *Clay Minerals*, **44**, 81–88.

Igel, J. (2007) On the small-scale variability of electrical soil properties and its influence on geophysical measurements. Dissertation der Universität Frankfurt am Main, Germany, 188 pp.

Ishida, T., Makinoo, T., and Wang, C. (2000) Dielectric-relaxation spectroscopy of kaolinite, montmorillonite, allophane, and imogolite under moist conditions. *Clays and Clay Minerals*, **48**, 75–84.

Kaufhold, S. and Dohrmann, R. (2003) Beyond the Methylene Blue method: determination of the smectite content using the Cu-triene method. *Zeitschrift für angewandte Geologie*, ISSN 0044-2259, 2/2003, **49**, 13–17.

Kaufhold, S. and Dohrmann, R. (2013) The variable charge of dioctahedral clay minerals. *Journal of Colloid and Interface Science*, **390**, 225–233.

Kaufhold, S. and Penner, D. (2006) Applicability of the SER method for quality control of clays from the German 'Westerwald'. *Applied Clay Science*, **32**, 53–63.

Kaufhold, S., Decher, A., and Dohrmann, R. (1998) Verfahren zur Bestimmung des Gehaltes an Tonmineralien in einem tonmineralhaltigen Material. Deutsches Patent DE 19839531.

Kaufhold, S., Dohrmann, R., Ufer, K., and Meyer, F.M. (2002) Comparison of methods for the quantification of montmorillonite in bentonites. *Applied Clay Science*, **22**, 145–151.

Kaufhold, S., Dohrmann, R., and Decher, A. (2003) The SER method: A new technique for the *in situ* estimation of the montmorillonite content of bentonites. *Zeitschrift für angewandte Geologie*, ISSN 0044-2259, 2/2003, **49**, 2–6.

Kesten, H. (2006) What is percolation? *Notices of the AMS*, **53**, 572–573.

Lagaly, G. (1994) Layer charge determination by alkylammonium ions. Pp. 2–42 in: *Layer Charge Characteristics of 2:1 Silicate Clay Minerals* (A. Mermut, editor). CMS workshop Lectures, vol. **6**, The Clay Minerals Society, Bloomington, Indiana, USA.

Meier, L.P. and Kahr, G. (1999) Determination of the cation exchange capacity (CEC) of clay minerals using the complexes of copper (II) ion with triethylenetetramine and tetraethylenepentamine. *Clays and Clay Minerals*, **47**, 386–388.

Mojid, M.A. and Cho, H. (2006) Estimating the fully developed diffuse double layer thickness from the bulk electrical conductivity in clay. *Applied Clay Science*, **33**, 278–286.

Rücker, C., and Günther, T. (2011) The simulation of finite ERT electrodes using the complete electrode model. *Geophysics*, **76**, 227–238.

Schulmeister, M.K., Butler, J.J., Healey, J.M., Zheng, L., Wysocki, D.A., and McCall, G.W. (2003) Direct-push electrical conductivity logging for high-resolution hydrostratigraphic characterisation. *Ground Water Monitoring and Remediation*, **23**, 52–62.

Slater, L. and Lesmes, D.P. (2002) Electrical-hydraulic relationships observed for unconsolidated sediments. *Water Resources Research*, **38**, 31-1–31-13.

Suddeth, K.A., Kitchen, N.R., and Drummond, S.T. (1999) Soil conductivity sensing on claypan soils: comparison of electromagnetic induction and direct methods. Pp. 971–990 in: *Proceedings of the 4th international conference on Precision Agriculture* (P.C. Robert *et al.*, editors). ASA Miscellaneous Publication, ASA, CSSA, and SSSA, Madison, Wisconsin, USA.

Tabbagh, A. and Cosenza, Ph. (2006) Effect of microstructure on the electrical conductivity of clay-rich systems. *Physics and Chemistry of the Earth*, **32**, 154–160.

Taioli, F., Gallas, J.D.F., Ribeiro, V., Toledo lezzi, P.B., and Nascimento, D.P.V. (2006) Desenvolvimento e testes de mini-sonda Wenner para avaliacao de contaminiacoes rasas. *Revista Brasileira de Geoofisica*, **24**, 525–534.

Telford, W.M., Geldart, L.P., Sheriff, R.E., and Keys, D.A. (1976) *Applied Geophysics.* Cambridge University Press, New York, 860 pp.

Waxman, M. and Smits, L. (1968) Electrical conductivities in oil-bearing shaly sands. *Society of Petroleum Engineers Journal*, **8**, 107–122.

Weiler, R.A. and Chaussidon, J. (1968) Surface conductivity and dielectrical properties of montmorillonite gels. *Clays and Clay Minerals*, **16**, 147–155.

(*Received 17 April 2013; revised 24 January 2014; Ms. 759; AE: J.W. Stucki*)

Clays and Clay Minerals, Vol. 62, No. 1, 13–19, 2014.

INFLUENCE OF MOLECULAR STRUCTURE OF QUATERNARY PHOSPHONIUM SALTS ON THAI BENTONITE INTERCALATION

CHUREERAT PRAHSARN[1,*], NANJAPORN ROUNGPAISAN[1], NATTAPHOP SUWANNAMEK[1], WATTANA KLINSUKHON[1], HIROMICHI HAYASHI[2], KAZUNORI KAWASAKI[2], AND TAKEO EBINA[2]

[1] National Metal and Materials Technology Center, 114 Paholyothin Rd., Klong 1, Klong Laung, Pathumthani 12120, Thailand
[2] Research Center for Compact Chemical Process, National Institute of Advanced Industrial Science and Technology, 4-2-1 Nigatake, Miyagino-ku, Sendai 983-8551, Japan

Abstract—A comprehensive study of the intercalation of organo-phosphonium salts into Thai bentonite (Mt) was conducted to investigate the influence of the molecular structures of organic moieties, including chain types (alkyl *vs*. aryl), chain length, and structural symmetry, on their intercalation. A series of quaternary phosphonium salts with systematically varied molecular structures (tetraphenyl phosphonium, TPP-Br; tetrabutyl phosphonium, TBP-Br; tetraoctyl phosphonium, TOP-Br; methyl triphenyl phosphonium, MTPP-Br; and butyl triphenyl phosphonium, BTPP-Br) was intercalated into Mt *via* an ion-exchange reaction. From thermogravimetric analysis results, tetrabutyl phosphonium-modified Mt (TBP) with shorter alkyl chain length began to decompose at a slightly lower temperature (263 *vs*. 351ºC), yet showed comparable thermal stability (*i.e.* maximum decomposition temperature) at 470ºC, compared to tetraoctyl phosphonium-modified Mt (TOP). Aryl phosphonium-modified Mt (TPP) showed a higher thermal decomposition temperature (576 *vs.* 470ºC) than those of alkyl phosphonium-modified Mts (TBP and TOP). Introducing short alkyl chains into the aryl phosphonium moiety (MTPP, BTPP) caused a slight decrease in thermal decomposition temperature, but an increase in cation loadings of their modified Mts (71 and 73%, respectively). X-ray diffraction analysis showed that the flexibility of alkyl chains in TBP yielded smaller increases in basal spacing, *i.e.* lower degree of intercalation, compared to the rigid aryl structure in TPP. Increasing chain length resulted in greater basal spacing in alkyl phosphonium-modified Mts (1.67 nm. in TBP *vs*. 2.46 nm. in TOP). Such an effect, however, was less significant in aryl phosphonium-modified Mt.

Key Words—Intercalation, Molecular Structure, Montmorillonite, Organo-clay, Phosphonium Salts.

INTRODUCTION

Organo-clays have been studied extensively in terms of their roles in enhancing thermal and mechanical properties of clay-polymer nanocomposites (Leszczynska *et al*., 2007a, 2007b; Paiva *et al*., 2008; Avalos *et al*., 2009; Feng *et al*., 2012; Garcia-Lopez *et al*., 2013; Suin *et al*., 2014). Many studies have been conducted on the modification of montmorillonite-rich clay to obtain organo-clay with high thermal stability, *i.e.* high decomposition temperature, using different types of organic modifiers such as ammonium salts, phosphonium salts, and imidazolium salts (Xie *et al*., 2002; Hedley *et al*., 2007; Leszczynska *et al*., 2007a, 2007b; Patel *et al*., 2007; Calderon *et al*., 2008; Paiva *et al*., 2008; Avalos *et al*., 2009; Feng *et al*., 2012; Garcia-Lopez *et al*., 2013; Suin *et al*., 2014). Organic modifiers helped to reduce the hydrophilic nature of the clay, resulting in better compatibility with organic polymers (Paiva *et al*., 2008). Properties of clay-polymer nanocomposites are mainly dependent on the dispersion of organo-clay in polymer matrix as well as interaction between organo-clay and polymer (Feng *et al*., 2012; Garcia-Lopez *et al*., 2013; Suin *et al*., 2014). Garcia-Lopez *et al*. (2012) reported different improvements in the thermomechanical properties of polyamide6/organo-sepiolite nanocomposites, which depended on modifier structures and contents. From their results, strong interaction between PA6 and the Diamin T modifier led to homogeneous dispersion of sepiolite-Diamin T in the nanocomposite, thus increasing the elastic modulus and heat deflection temperature.

For organo-clays modified with ammonium salts, which have low thermal stability, thermal degradation begins to occur when the polymer processing temperature exceeds 200ºC (Patel *et al*., 2007; Calderon *et al*., 2008). Other complex salts such as phosphonium, pyridinium, imminium, and imidazolium salts were later employed to achieve greater thermal stability of modified clays (Xie *et al*., 2002; Hedley *et al*., 2007; Leszczynska *et al*., 2007a; Patel *et al*., 2007; Calderon *et al*., 2008; Paiva *et al*., 2008; Avalos *et al*., 2009; Suin *et al*., 2014). Several factors including chemical structure, packing density, and type of cation in the organic modifier, as well as silicate layer thickness in the clay, were found to influence the space between the silicate layers and thermal stability of the organo-clays. Calderon *et al*. (2008) employed four alkylphosphonium

* E-mail address of corresponding author:
chureerp@mtec.or.th
DOI: 10.1346/CCMN.2014.0620102

salts with different molecular structures to investigate the effects of chemical composition and molecular weight of phosphonium salts on the thermal stability and basal spacing of modified clays. An organo-clay with tetra n-octyl phosphonium salt, which had the shortest chain length and smallest molecular weight of those examined, showed the smallest basal spacing compared to those with additions of higher molecular weight salts. The thermal stability and degradation mechanisms of modified montmorillonites of alkyl and aryl quaternary phosphonium salts (dodecyltriphenyl phosphonium, tetradecyltributyl phosphonium, hexadecyl tributyl phosphonium, octadecyltributyl phosphonium, tetraphenyl phosphonium, and tetraoctyl phosphonium) were investigated by Xie *et al.* (2002) and compared to clay modified with ammonium salt (tetraoctyl ammonium bromide). Unlike the ammonium salt system, the thermal stability of phosphonium-modified clay depended on the molecular structures of the organic salts. The symmetric tetraoctyl phosphonium-modified clay showed an increase in decomposition temperature of 30ºC, compared to that of asymmetric tributyl alkyl phosphonium-modified clay. The increased decomposition temperature was explained to result from an increase in steric resistance around the P center of the tetraoctyl phosphonium ion, thus reducing the susceptibility of the alkyl chains to β-elimination. For triphenyl alkyl phosphonium-modified clay, steric hindrance from phenyl groups contributed to the increased thermal stability. In addition, $p\pi-d\pi$ interactions between the P center and phenyl groups led to delocalization of the positive charge, thus inhibiting the alkyl chain from β-elimination. Patel *et al*. (2007) prepared modified montmorillonites (Mt) with different quaternary phosphonium cations (hexadecyl tributyl phosphonium, tetradecyl tributyl phosphonium, tetraphenyl phosphonium, methyl triphenyl phosphonium, ethyl triphenyl phosphonium, and propyl triphenyl phosphonium). Tetraphenyl phosphonium-modified Mt exhibited the highest decomposition temperature (350−400ºC). Substitution of the phenyl group with alkyl chains (methyl, ethyl, or propyl group) resulted in lower decomposition temperatures (300−350ºC). The thermal stability or decomposition temperature was found to increase with alkyl chain length. Tetrabutyl phosphonium-modified Mt, despite having relatively short chain length, showed an unexpectedly high decomposition temperature (up to 350ºC) due to the high thermal stability of the tetrabutyl phosphonium cation.

Though these earlier studies provided informative experimental data, they had been reported individually and their results had not been correlated. To develop a comprehensive understanding of the influence of organic modifiers on organo-clay, the present study employed a series of quaternary phosphonium salts with systematically varied molecular structures to intercalate into the Thai bentonite *via* a cation exchange reaction. The influence of molecular structures of organic modifiers on basal spacings and decomposition temperatures of phosphonium-modified Mts was investigated and discussed in relation to those reported by other research groups.

MATERIALS AND METHODS

Materials

Thai bentonite was provided by the Thai Nippon Co. Ltd (Thailand). The bentonite was further purified, using a method modified from Thuc *et al.* (2010): 10 g of bentonite was dispersed in 2 L of deionized water and stirred for 24 h, followed by sonication for 20 min. The resultant bentonite slurry was then left to settle for 50 h. The upper fraction of slurry with dispersed clay particles (~1500 mL) was collected and oven dried slowly at 90ºC. The cation exchange capacity (CEC) of the purified bentonite, determined by the standard ammonium acetate method, was 80 meq/100 g. Phosphonium bromide salts purchased from Aldrich were used as received. Their molecular structures as well as the molecular mass of the cations are shown in Table 1.

Preparation of phosphonium-modified montmorillonite

A 5 g portion of purified bentonite (Mt) was dispersed in 1 L of deionized water and stirred continuously for 30 min at room temperature, using a disperser (Ultra-Turrax® T50, IKA, Stauffen, Germany). Excess phosphonium salt (5 g) was added slowly to the bentonite slurry and stirred at high speed (~6000 rpm) for 30 min to allow intercalation of phosphonium cations into Mt *via* ion exchange before further stirring at medium speed (~3000 rpm) for another 3 h. The phosphonium-modified Mt was filtered and washed with deionized water until no residual bromide remained and then dried at 110ºC for 24 h. The modified Mts obtained (identified as in Table 1) were prepared as powder samples for analysis by X-ray diffraction (XRD) and thermal analysis.

Characterization

The thermal properties of purified Mt, organic phosphonium salts, and phosphonium-modified Mts were characterized by thermogravimetric analysis (TGA) using a Mettler Toledo (Leicester, UK) instrument (SDTA 851°). Samples were heated to 1200ºC (except for the phosphonium salts which were heated to 900ºC) at a heating rate of 10.0 ºC/min under a N_2 flow of 20 mL/min. The structures of Mt and phosphonium-modified Mts were characterized, using a wide-angle X-ray diffraction apparatus (JEOL, JDX3530) with CuKα source. Intensity distributions for diffraction angles (2θ) ranging from 3 to 80º2θ at a scanning rate of 0.02º2θ/min were recorded. The corresponding *d* values were then derived from the first-order reflections.

Table 1. List of phosphonium salts and their structures.

Phosphonium salts	Molecular structure	Cation MW (g/mol)	Organo-modified clay labeling
Tetrabutyl phosphonium bromide	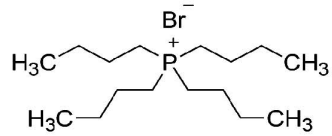	259	TBP
Tetraoctyl phosphonium bromide	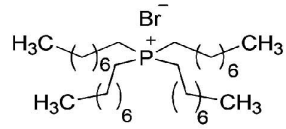	491	TOP
Tetraphenyl phosphonium bromide	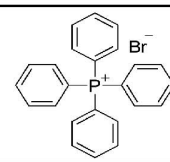	339	TPP
Methyltriphenyl phosphonium bromide	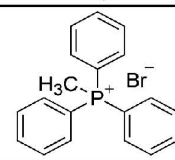	277	MTPP
Butyltriphenyl phosphonium bromide	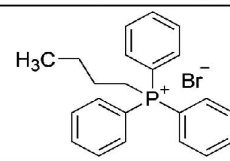	319	BTPP

RESULTS AND DISCUSSION

Thermogravimetric analysis

Derivative TGA mass-loss curves (Figure 1a) showed that the parent Mt maintained thermal stability, *i.e.* was not thermally decomposed, through the range of temperatures studied. The derivative mass-loss peaks which occurred below 200ºC were due to loss of interlayer water and the adsorbed gases such as N_2 (Xie *et al.*, 2002). Phosphonium-modified Mts exhibited greater thermal stabilities than their corresponding phosphonium salts (Figure 1a,b) such that decomposition temperatures occurred over the ranges 470−576ºC and 285−419ºC, respectively. Overall, the modified Mts showed gradual mass loss before a significant loss of mass occurred at a single particular temperature, except for tetraphenyl phosphonium-modified Mt (TPP) and tetraoctyl phosphonium-modified Mt (TOP) each of which showed two decomposition steps.

To investigate the influence of the alkyl chain length of organic moieties in phosphonium salts on the thermal stability of modified Mt, tetrabutyl phosphonium-modified Mt (TBP) and tetraoctyl phosphonium-modified Mt (TOP) were compared. In order to compare the resulting data with previous studies, the decomposition temperature was reported as the temperature range between two temperature points; the temperature at 5% mass loss (T_5) and the temperature at maximum rate of mass loss (T_{max}). The TBP underwent thermal decomposition over a temperature range of 263−471ºC whereas that of TOP occurred at a temperature range of 351−470ºC (Table 2). Although TBP began to decompose at a lower temperature than did TOP (T_5 = 263 *vs*. 351ºC), both showed comparable decomposition temperatures for maximum rate of mass loss (T_{max}) up to 470ºC. The lower initial temperature of decomposition was thought to be due to the shorter alkyl chain length in TBP, but the molecular symmetry of tetrabutyl- and tetraoctyl-phosphonium moieties ensured that for the thermal stabilities observed in their modified Mts that the T_{max} temperatures were still at 470ºC.

When alkyl groups (tetrabutyl; TBP) were replaced by aryl groups (tetraphenyl; TPP) for organic moieties in phosphonium salt, an increase in decomposition temperature was observed (263−471ºC *vs*. 418−576ºC, respectively). A similar observation was reported by Xie *et al.* (2002), who found that tetraphenyl phosphonium-Mt showed a greater decomposition temperature

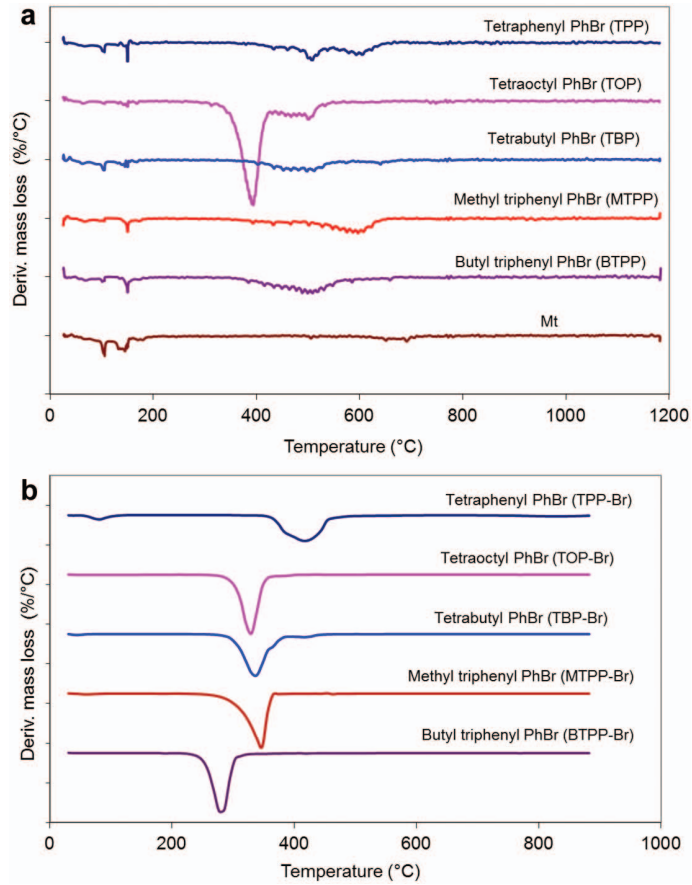

Figure 1. Derivative mass-loss curves of parent Mt (a), modified Mts (a), and phosphonium salts (b).

than tetraoctyl phosphonium-Mt (309–407ºC *vs.* 262–362ºC, respectively), despite the longer chain of the octyl group. According to Xie *et al.* (2002), this was due to steric hindrance from the phenyl substituents as well as the absence of α-hydrogen in phenyl groups, which inhibited α- and β-eliminations and led to different decomposition pathways, resulting in greater thermal stability. Kawasaki *et al.* (2010) prepared transparent clay film by cation exchange reaction of synthetic saponite (SA) with tetraphenyl phosphonium

Table 2. Basal spacing and thermal properties of modified Mts and phosphonium salts.

Sample	Basal spacing (nm)	Temperature (ºC) (@ 5% wt. loss)	Temperature (ºC) (@ max. wt. loss rate)	Cation loading (%)
Mt	1.53	131*	n/a	n/a
TBP	1.67	263	471	65.5
TOP	2.46	351	470	32.5
TPP	1.79	418	576	30.5
MTPP	1.75	431	543	73.74
BTPP	1.83	405	499	71.2
Organic phosphonium salts				
TBP-Br	–	–	340	–
TOP-Br	–	–	332	–
TPP-Br	–	–	419	–
MTPP-Br	–	–	355	–
BTPP-Br	–	–	285	–

* Mainly water loss

bromide (TPP-Br). From TG-differential thermal analysis (DTA) measurement, the resultant tetraphenyl phosphonium saponite (TPP-SA) film showed good thermal stability such that decomposition occurred at 380−600ºC and its DTA peak occurred at 550ºC, which is in good agreement with the observation made on TPP in the current study.

When one aryl chain in tetraphenyl phosphonium-modified Mt (TPP) was substituted by alkyl chains (methyl triphenyl phosphonium- and butyl triphenyl phosphonium-), the decomposition temperature was altered. Methyl triphenyl phosphonium-modified Mt (MTPP) showed a slight decrease in decomposition temperature compared to TPP (431−543ºC *vs*. 418−576ºC, respectively). With increasing alkyl chain length, butyl triphenyl phosphonium-modified Mt (BTPP) showed a further decrease in decomposition temperature (405−499ºC). Increasing the chain length of the substituted alkyl chain in the aryl phosphonium moiety caused the molecular structure to be more asymmetric, which tended to decrease decomposition temperature of the modified montmorillonite. A similar trend was observed in their corresponding phosphonium salts in that BTPP-Br showed a lower decomposition temperature than MTPP-Br and TPP-Br (285ºC, 355ºC, and 419ºC, respectively). Despite their asymmetric structures, alkyl-substituted aryl phosphonium-modified Mts (MTPP and BTPP) still showed greater decomposition temperatures than those of alkyl phosphonium-modified Mts (TBP and TOP). Similar observations have been reported by other studies. The influence of molecular symmetry on decomposition temperature of phosphonium-modified Mt was examined by Patel *et al.* (2007), who reported that the symmetric tetraphenyl phosphonium-modified Mt showed the highest decomposition temperature at 350−400ºC (at T_5), while substitution of the phenyl group by a methyl, ethyl, or propyl group resulted in lower decomposition temperature (T_5 = 300−350ºC). Xie *et al.* (2002) reported that the short chains having symmetrical structures showed higher decomposition temperature than non-symmetrical longer-chain structures. Tetraoctyl phosphonium Mt (P-4C8), which has a symmetrical structure, exhibited degradation temperatures which were ~30ºC higher than those of asymmetric tributyl alkyl phosphonium Mts (where alkyl = tetradecyl (C14), hexadecyl (C16), and octadecyl (C18)).

To investigate incorporation of organic phosphonium cations in Mt interlayers, organic cation loading of modified Mts was evaluated by comparing measured mass loss (from TGA) with the theoretically completely exchanged Mt (based on CEC of 80 meq/100 g). As mentioned previously, tetraphenyl phosphonium-modified Mt (TPP) and tetraoctyl phosphonium-modified Mt (TOP) showed two decomposition steps. In comparison with their respective phosphonium salts, the first decomposition step occurred in a temperature range comparable to that of the phosphonium salt. The decomposition at the second step should relate to the organic phosphonium moiety contained in the Mt interlayer. Organic mass losses which occurred during this second step were, thus, employed to determine the organic cation loadings for TPP and TOP, and these were found to be 30.5 and 32.5%, respectively (Table 2). For the others, tetrabutyl phosphonium-modified Mt (TBP), methyl triphenyl phosphonium-modified Mt (MTPP), and butyl triphenyl phosphonium-modified Mt (BTPP), decomposition of which occurred in a single step, had calculated cation loadings of 65.5, 73.7, and 71.2%, respectively. Increases in cation loading of MTPP and BTPP, compared to that of TPP, implied that introducing flexible alkyl chains assisted in the incorporation of the rigid aryl phosphonium moiety into the montmorillonite interlayer. Good mixing of the clay-polymer nanocomposite while maintaining heat stability could, thus, be achieved.

X-ray diffraction

Investigation of the XRD patterns (3−10º2θ) of purified and phosphonium-modified Mts (Figure 2) revealed that the bentonite (Mt) characteristic reflection occurred at 5.8º, and the corresponding basal spacing was 1.53 nm (Table 2). As organic phosphonium cations were exchanged in the Mt interlayers, the basal spacings of the modified Mts increased and were in the range 1.67−2.46 nm. To investigate the influence of alkyl chain length of organic moieties on intercalation of phosphonium salt into Mt, tetrabutyl phosphonium-modified Mt (TBP) and tetraoctyl phosphonium-modified Mt (TOP) were compared. The basal spacing of TOP, having longer alkyl chain-length moieties, was greater than that of TBP (2.46 *vs*. 1.67 nm, respectively). This corresponds well with observations reported by Patel *et al.* (2007) that basal spacing increases with alkyl chain length. A similar trend was reported by Xie *et al.* (2002), who found that basal spacing increased from 1.93 nm to 2.04 nm and 2.18 nm for tetradecyl tributyl (C14), hexadecyl tributyl (C16), and octadecyl tributyl (C18) phosphonium-modified Mt, respectively. When aryl groups (tetraphenyl; TPP) were substituted in place of alkyl chains (tetrabutyl; TBP) for organic moieties in phosphonium salt, slight increases in basal spacing were observed (1.79 and 1.67, respectively). The molecular shapes of different phosphonium cations were determined by Patel *et al.* (2007) using molecular modeling software and those authors also calculated their corresponding molecular chain lengths. From their work, using the relationship between basal spacing and chain length, tetraphenyl phosphonium-Mt (P4) showed greater basal spacing than tetrabutyl phosphonium-Mt (P1) (1.76 *vs*. 1.4 nm) despite having comparable chain length (~0.55 and 0.57 nm, respectively). This supports observations made on TPP and TBP in the present work, and indicates that the rigid structure of the aryl group in

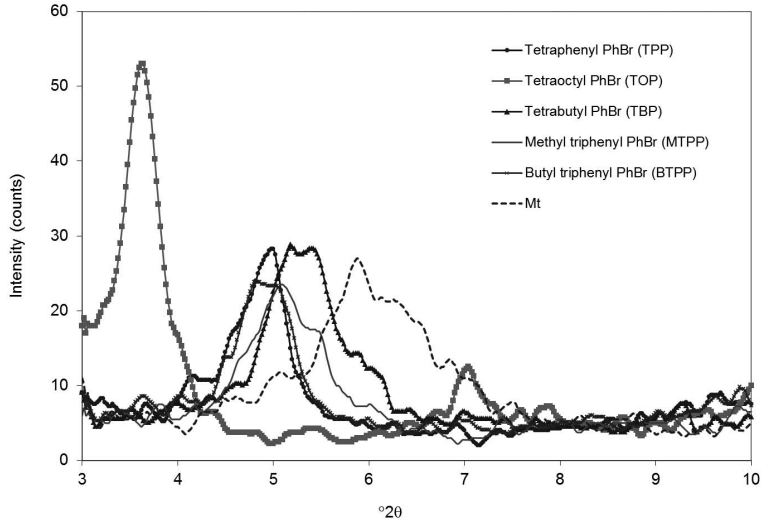

Figure 2. XRD patterns of parent Mt and modified Mts.

the tetraphenyl phosphonium moiety causes a larger increase in basal spacing.

When one aryl group in tetraphenyl phosphonium-modified Mt (TPP) was substituted by alkyl chains (methyl triphenyl, MTPP; butyl triphenyl, BTPP), the basal spacings were slightly different (d = 1.79, 1.75, and 1.83 nm, respectively). Patel *et al.* (2007) reported that basal spacing of tetraphenyl phosphonium-modified Mt and its derivatives of one substituted alkyl chain of different chain lengths (methyl, ethyl, and propyl) were comparable. For longer alkyl chain lengths, Xie *et al.* (2002) also reported slightly smaller basal spacings in dodecyl triphenyl phosphonium-modified Mt, compared to that of tetraphenyl phosphonium counterpart (d = 1.82 and 1.88 nm, respectively). These observations on comparable basal spacings in mono-alkyl triphenyl phosphonium-modified Mts, despite their different alkyl chain lengths, imply that the alkyl chains are possibly folded among phenyl groups instead of extending outward. The influence of alkyl chain length in aryl-type moieties is, thus, small compared to that of the alkyl group.

CONCLUSIONS

Thai bentonite (Mt) was modified with phosphonium salts of varied structures, and characterized by TGA and XRD. Aryl phosphonium-modified Mts (TPP) showed higher decomposition temperatures, *i.e.* greater thermal stabilities, than those of alkyl phosphonium-modified Mts. The asymmetric structure in methyl triphenyl- and butyl triphenyl phosphonium-modified Mts (MTPP and BTPP), in which one alkyl chain was introduced into TPP, caused slight decreases in their decomposition temperatures. Their cation loadings, however, increased (from 30% for TPP to 71% and 73% for BTPP and MTPP, respectively), which could favor the use of clay as a filler in polymer composites with improved thermal stability. In alkyl phosphonium-modified Mt, a larger basal spacing was observed with increasing alkyl chain length. In aryl phosphonium-modified Mt, however, the effect of alkyl chain length was less significant such that the basal spacings of alkyl triphenyl phosphonium-modified clays were comparable to those of their TPP counterparts. A fundamental understanding of the influences of organic modifiers on the intercalation of clays as well as on the thermal stabilities of the modified clays obtained can be used as a guide for selection of organo-clays as fillers in polymer-clay composites to achieve effective mixing and high thermal stability.

ACKNOWLEDGMENTS

The present study was supported by the National Metal and Materials Technology Center (Thailand) (grant number: MT-B-53-POL-07-488-I).

REFERENCES

Avalos, F., Ortiz, J.C., Zitzumbo, R., Lopez-Manchado, M.A., Verdejo, R., and Arroyo, M. (2009) Phosphonium salt intercalated montmorillonites. *Applied Clay Science*, **43**, 27−32.

Calderon, J.U., Lennox, B., and Kamal, M.R. (2008) Thermally stable phosphonium montmorillonite organo-clay. *Applied Clay Science*, **40**, 90−98.

Feng, J., Hao, J., Du, J., and Yang, R. (2012) Effects of organoclay modifiers on the flammability, thermal and mechanical properties of polycarbonate nanocomposites filled with a phosphate and organoclays. *Polymer Degradation and Stability*, **97**, 108−117.

Garcia-Lopez, D., Fernandez, J. F., Merino, J. C., and Pastor, J. M. (2013) Influence of organic modifier characteristic on the mechanical properties of polyamide6/organosepiolite nanocomposites. *Composites: Part B*, **45**, 459−465.

Hedley, C.B., Yuan, G., and Theng, B.K.G. (2007) Thermal analysis of montmorillonites modified with quaternary

phosphonium and ammonium surfactants. *Applied Clay Science*,
35, 180–188.

Kawasaki, K., Ebina, T., Mizukami, F., Tsuda, H., and Motegi, K. (2010) Development of flexible organo-saponite films and their transparency at high temperature. *Applied Clay Science*, **48**, 111–116.

Leszczynska, A., Njuguna, J., Pielichowski, K., and Banerjee, J.R. (2007) Polymer/montmorillonite nanocomposites with improved thermal properties I. Factors influencing thermal stability and mechanisms of thermal stability improvement. *Thermochimica Acta*, **453**, 75–96.

Leszczynska, A., Njuguna, J., Pielichowski, K., and Banerjee, J.R. (2007) Polymer/montmorillonite nanocomposites with improved thermal properties II. Thermal stability of montmorillonite nanocomposites based on different polymeric matrixes. *Thermochimica*, **454**, 1–22.

Paiva, L.B., Morales, A.R., and Diaz, F.R.V. (2008) Organoclay: Properties, preparation and applications. *Applied Clay Science*, **42**, 8–24.

Patel, H.A., Somani, R.S., Bajaj, H.C., and Jasra, R.V. (2007) Preparation and characterization of phosphonium montmorillonite with enhanced thermal stability. *Applied Clay Science*, **35**, 194–200.

Suin, S., Maiti, S., Shrivastava, N.K., and Khatua, B.B. (2014) Mechanically improved and optically transparent polycarbonate/clay nanocomposites using phosphonium modified organoclay. *Materials and Design*, **54**, 553–563.

Thuc, C.N.H., Grillet, A.C., Reinert, L., and Ohashi, F. (2010) Separation and purification of montmorillonite and polyethylene oxide modified montmorillonite from Vietnamese bentonites. *Applied Clay Science*, **49**, 229–238.

Xie, W., Xie, R., Pan, W.P., Hunter, D., Koene, B., Tan, L.S., and Vaia, R. (2002) Thermal stability of quaternary phosphonium modified montmorillonites. *Chemistry of Materials*, **14**, 4837–4845.

(*Received 6 October 2013; revised 25 January 2014; Ms. 816; AE: J. Brendlé-Miehé*)

Clays and Clay Minerals, Vol. 62, No. 1, 20–34, 2014.

XAFS STUDY OF Fe-SUBSTITUTED ALLOPHANE AND IMOGOLITE

LESLIE L. BAKER*, RYAN D. NICKERSON, AND DANIEL G. STRAWN
Division of Soil and Land Resources, University of Idaho, Moscow, ID 83844-3022, USA

Abstract—The nano-aluminosilicate mineral allophane is common in soils formed from parent materials containing volcanic ash and often contains Fe. Due to its lack of long-range order, the structure of allophane is still not completely understood. In the present study, Fe K-edge X-ray absorption fine structure (XAFS) was used to examine Fe-containing natural and synthetic allophane and imogolite samples. Results indicated that Fe substitutes for octahedrally coordinated Al in allophane, and that Fe exhibits a clustered distribution within the octahedral sheet. Iron adsorbed on allophane surfaces is characterized by spectral features distinct from those of isomorphically substituted Fe and of ferrihydrite. Fe adsorbed on the allophane surfaces probably exists as small polynuclear complexes exhibiting Fe–Fe edge sharing, similar to poorly crystalline Fe oxyhydroxides. The XAFS spectra of natural allophane and imogolite indicate that the Fe in the minerals is a combination of isomorphically substituted and surface-adsorbed Fe. In the synthetic Fe-substituted allophanes, the Fe XAFS spectra did not vary with the Al:Si ratio. Theoretical fits of the extended XAFS (EXAFS) spectra suggest that local atomic structure around octahedral Fe in allophanes is more similar to Fe in a smectite-like structure than to a published theoretical nanoball structure.

Key Words—Allophane, Fe K-edge XAFS, Imogolite.

INTRODUCTION

Poorly crystalline nano-sized aluminosilicates such as allophane, imogolite, and halloysite are common weathering products of volcanic materials on Earth. They often form by weathering of glassy volcanic ejecta in volcanic tuffs and ash-containing soils, sometimes *via* microbially facilitated processes (Kawano and Tomita, 2001; Tazaki *et al.*, 2006). High-silica allophane can also form by direct precipitation from water enriched in Al and Si, such as near hydrothermal vents. These aluminosilicates impart unique properties to soils in which they occur, including sorption of nutrients, particularly phosphate, stabilization of organic matter, and increased water-holding capacities (Parfitt, 2009). Allophanes are also proposed as possible weathering phases on the surface of Mars (Ming *et al.*, 2006; Rampe *et al.*, 2012).

The compositional range of allophanes is wide, and encompasses both Al-rich and Si-rich types, sometimes referred to as proto-imogolite and hydrous feldspathoid types, respectively (Farmer *et al.*, 1979) (Table 1). Different compositional types are characteristic of specific environments, and form under different pH and solution compositions (Farmer *et al.*, 1991). Allophane minerals are typically metastable, yet are common in surficial weathering environments. With time, allophane transforms to more ordered clay minerals, but the end products of this transformation are dependent upon temperature, oxidation state, and the chemical composition of the solution (Farmer *et al.*, 1991; Farmer, 1997). At present, systematic understanding of the effects of these variables upon allophane stability or upon its eventual transformation to more crystalline forms is lacking.

Iron commonly substitutes into the structure of minerals, isomorphically replacing octahedral cations, especially Al. Iron-substituted natural and synthetic allophane, imogolite, and halloysite samples have been described (Kitagawa, 1973). Natural allophane from Ecuador contains oxalate-soluble Fe that may be present in isomorphic substitution in the allophane, as well as dithionite-extractable Fe present in a finely dispersed goethite phase (Kaufhold *et al.*, 2009, 2010). The X-ray absorption spectrum (XAS) of Fe-substituted imogolite is distinct from that of Fe-adsorbed imogolite (Ookawa *et al.*, 2006), but the structures have not been fully modeled. According to McBride *et al.* (1984), allophane can accommodate more Fe in its structure than well formed imogolite. Iron in allophane samples may sometimes be present as ferrihydrite nanoparticles rather than isomorphically substituting for Al (Ossaka *et al.*, 1971; MacKenzie and Cardile, 1988). Several natural allophane samples were analyzed by Horikawa and Soezima (1977) using X-ray emission spectroscopy and those authors observed that Fe in these samples was distinct from Fe in Fe oxides, as well as from Fe in hisingerite and nontronite. Substitution of Fe into the structures of nano-aluminosilicates such as allophane has been reported to affect their morphology (Joussein *et al.*, 2005), as well as the kinetics and end products of their ripening to more crystalline clay minerals (McBride *et al.*, 1984; Farmer *et al.*, 1991; Farmer, 1997). Iron-substituted allophanes may ripen to an

* E-mail address of corresponding author:
lbaker@uidaho.edu
DOI: 10.1346/CCMN.2014.0620103

Table 1. Sample names, nominal and analyzed compositions, and locations of characteristic IR peaks (Figure 2).

Material (nominal Al:Si)	SiO_2 (mol.%)	Al_2O_3 (mol.%)	Fe_2O_3 (mol.%)	IR peaks		
				OH stretch	Si−O stretch	Al−O stretch
Synthetic samples						
Allophane (1:3) (hydrous feldspathoid)	86	13	0.09	3320	1180, 1075, 920	710
Allophane (1:1)	66	33	0.32	3540, 3290	1170, 1050, 950	
Allophane (2:1) (proto-imogolite)	57	42	0.61	3540, 3290	950	
Imogolite (2:1)	50	49	0.85	3600, 3300	990, 920	700
Fe-adsorbed allophane	66	34	0.35			
Natural samples						
KiP allophane (Japan)	56	40	4.46	3520, 3335	967	683
KiG imogolite (Japan)	51	48	0.52	3525, 3300	990, 950	695

Fe-depleted phase plus ferrihydrite (McBride *et al.*, 1984), or they may recrystallize to Fe-bearing clays such as nontronite (Farmer *et al.*, 1991) or ferruginous beidellite (Farmer, 1997). The specific conditions that lead Fe-bearing allophane to ripen into various end products are not well known.

Due to their lack of long-range crystal ordering, allophanes are difficult to study and their structure is still not completely understood, particularly with respect to the effect of widely varying Al:Si ratios in the same fundamental structural unit. The structure of imogolite, which has a more clearly defined Al:Si ratio, is better understood. The fundamental structural unit for both of these nano-aluminosilicates is thought to be an Al octahedral sheet (gibbsite sheet) rolled into a spheroidal, polyhedral, or tubular shape (Cradwick *et al.*, 1972; Parfitt *et al.*, 1980). In imogolite, Si is present as isolated tetrahedra bonded to the interior of the rolled gibbsite sheet by three Al−O−Si linkages, with one Si−OH pointing to the inside of the tube (Cradwick *et al.*, 1972; Creton *et al.*, 2008b). In synthetic systems, small, curved sections with such a structure have been shown to form rapidly upon hydrolysis and to self-assemble upon heating to form nanotubes (Levard *et al.*, 2010, 2011; Yucelen *et al.*, 2011). Proto-imogolite allophane may have a similar structure to imogolite, but with the gibbsite sheet rolled into a spherical rather than tubular shape. In a theoretical 40 nm-diameter proto-imogolite-like nanosphere constructed of imogolite-like orthosilicate units, Al:Si ratios of ~2:1 are predicted (Creton *et al.*, 2008a). The location of additional Si in more Si-rich (feldspathoid type) allophanes is not well understood, although in very high-Si compositions the fundamental structure may be a rolled Si tetrahedral sheet with an incomplete Al octahedral sheet in its interior (Childs *et al.*, 1990). An intermediate structure for Si-rich allophane based upon a curved kaolinite structure containing a defective tetrahedral sheet was proposed by Mackenzie *et al.* (1991). At present, no apparent consensus exists on whether high-Si and high-Al forms of allophane represent fundamentally different types of structure, or whether they represent a single fundamental structural type that is progressively modified to accommodate varying Al:Si ratios.

X-ray absorption fine structure spectroscopy is a useful technique for studying the structure of amorphous materials and nanominerals because it provides insight into short-range molecular structure at the atomic level, regardless of long-range structural order. The study of natural samples of poorly crystalline materials such as allophanes is complicated by variations in chemistry and by the possible presence of other mineral phases. To overcome this complexity, minerals synthesized in the laboratory under controlled conditions can be studied and compared to natural samples.

In the present study, Fe K-edge XAFS spectroscopy, including both X-ray absorption near-edge spectroscopy (XANES) and EXAFS, was used to analyze laboratory-synthesized minerals and natural samples. A challenge in analyzing natural samples is distinguishing between Fe-poor aluminosilicates and Fe-rich minerals such as ferrihydrite. Using EXAFS and XANES spectroscopy, Baker *et al.* (2010) showed that this can be achieved for low-Fe natural soil clays. In samples with Fe isomorphically substituted for Al, the Fe XAFS spectrum probes the short-range order in the octahedral sheet. The objective of the present study was to investigate Fe speciation and coordination state in synthetic and natural allophane and imogolite samples. The XAFS shell modeling was thus used to test existing models of allophane structure, and to examine the hypothesis that high-Al and high-Si forms of allophane have the same fundamental structure, based on a rolled octahedral sheet.

METHODS

Materials

Allophanes were synthesized at a range of Al:Si ratios (Table 1) using the method described by Baker and Strawn (2012), which was a modification of that

described by Montarges-Pelletier *et al.* (2005). The method was modified to produce Fe-substituted allophanes by adding 0.1 M $FeCl_3$ to the starting materials to produce a final Fe:Al molar ratio of 1:100. All syntheses were scaled to a total suspension volume of 1 L. The final supernatant from synthesis was decanted and saved for analysis. The precipitated gels were washed twice with deionized (DI) water, centrifuged for 15 min at 1000 × g, and placed in dialysis tubing in DI water until the final conductivity was <5 μS cm^{-1}. The dialyzed gel was again centrifuged and frozen for storage. A portion of each gel was removed and freeze-dried for analysis.

Imogolite gel was synthesized using the method of Farmer *et al.* (1977), modified to produce Fe-substituted imogolite by including 0.1 M $FeCl_3$ in the starting materials. In the present study, including Fe in the suspension promoted the formation of imogolite nanotubes more rapidly than in Fe-free compositions; in Fe-bearing solutions nanotubes formed after 1 week, but in Fe-free solutions two weeks of continuous heating were necessary to form detectable nanotubes. Nanotube formation was confirmed by microscopic and spectroscopic analysis.

A 2-line ferrihydrite was synthesized using the method described by Schwertmann *et al.* (2004). A solution of 0.1 M NaOH was titrated at a rate of 5 mL/min into a 100 mL aliquot of 0.1 M $Fe(NO_3)_3$ under constant stirring until the solution reached a pH of 7, using a total of 375 mL of NaOH altogether. The precipitate from this procedure was centrifuged and dialyzed in DI water. A portion of the gel was freeze-dried and was analyzed by X-ray diffraction (XRD) to confirm that the product was 2-line ferrihydrite.

Fe-adsorbed allophane was synthesized using the following procedure. A 50 g aliquot of an initially Fe-free allophane, synthesized as described above, was suspended in 500 mL of deionized water, and the suspension pH was adjusted to 3.5. A total of 250 mL of 0.001 M $Fe(NO_3)_3$ with pH adjusted to 3.5 was titrated at a rate of ~1 mL min^{-1} under vigorous stirring. While stirring, the pH was titrated dropwise with 0.1 M NaOH to a final value of 4.5. The sample was stirred overnight, centrifuged for 15 min at 1000 × g, washed twice with deionized water, and stored frozen. A portion of each sample was removed and freeze-dried for further analysis.

Natural allophane (KiP) and imogolite (KiG) separated from Japanese pumice from Kitakami were obtained from the collection of Dr S. Hiradate (Hiradate and Wada, 2005). Allophane and imogolite from this site were originally described by Miyauchi and Aomine (1966) and have been studied extensively. The natural allophane and imogolite samples were analyzed as received.

Analytical methods

Freeze-dried allophane and imogolite powders were analyzed using diffuse reflectance Fourier transform infrared spectroscopy (FTIR), powder XRD, scanning electron microscopy (SEM), and ^{27}Al and ^{29}Si nuclear magnetic resonance spectroscopy (NMR) to confirm their identification and further characterize their structure. The FTIR analyses were carried out on a Perkin-Elmer System 2000 (Thermo Scientific, Waltham, Massachusetts, USA), using a mixture of 3 wt.% allophane in optical-grade KBr. Spectra were processed using the Kubelka-Munk algorithm provided in Perkin Elmer Spectrum 2.0 software. The XRD scans were run on a Siemens D5000 diffractometer (Bruker AXS, Karlsruhe, Germany) using CuKα radiation (1.54 Å), and the data were analyzed using the Bruker *Diffracplus Eva* evaluation program (Bruker AXS, Karlsruhe, Germany). The SEM images were collected using a Zeiss Supra 35 field emission SEM (Carl Zeiss Microscopy GmbH, Jena, Germany) with a Noran System Six electron dispersive spectroscopic analyzer (EDS) (Thermo Scientific, Waltham, Massachusetts, USA) for semi-quantitative elemental analysis of individual particles. Samples of Fe-substituted and Fe-free 1:1 Al:Si synthetic allophane were analyzed using ^{27}Al and ^{29}Si magic angle spinning (MAS) solid-state NMR on a Bruker Avance 500 MHz spectrometer (Bruker Biospin, Rheinstetten, Germany).

All samples were analyzed by means of loss on ignition (LOI) to determine their total water content, and were dissolved for total elemental analysis using the following procedure. A 10 mg sample of each material was weighed and mixed thoroughly with 0.500 g of lithium metaborate flux; samples were analyzed in triplicate. The sample-flux mixture was placed in a graphite crucible and fused in a muffle furnace at 1000ºC for 30 min. Upon removal from the furnace, the molten bead was poured directly into 25 mL of 1 M HNO_3. After the bead was fully dissolved, the solution was diluted with deionized water to a final volume of 100 mL. These dissolved samples, and the supernatants from gel synthesis, were analyzed for major element composition in a Thermo Scientific iCAP inductively coupled plasma atomic emission spectrometer (ICP-AES) (Thermo Scientific, Waltham, Massachusetts, USA).

Bulk Fe K-edge XAFS scans for all allophanes and standards were collected on Beamline 7-3 at the Stanford Synchrotron Radiation Laboratory (SSRL). The monochromator for this beamline consisted of two parallel Si(220) crystals with a 6 mm entrance slit. All samples were run in a liquid He-cooled cryostat at a temperature of 7 K. Fluorescence data were collected using a 13-element Ge detector or a passivated implanted planar silicon (PIPS) detector. Step size through the XANES region was 0.35 eV, sufficient to give ~20 points defining the smallest (pre-edge) peaks. Samples were packed as wet gels or freeze-dried powders (no differences were observed between spectra of gel packs and powder packs of the same sample) into stainless

steel sample holders and held in place with Kapton tape. The XAFS scans were also collected for laboratory-synthesized two-line ferrihydrite as a freeze-dried powder. The ferrihydrite powder was smeared on filter paper, which was cut into strips, stacked three layers thick, and sealed in the sample holder with Kapton tape. Both transmission and fluorescence spectra were collected for all samples; fluorescence spectra were used for all samples because of their higher signal to noise ratio. For high-Fe samples both fluorescence and transmission data were compared, and fluorescence data showed no self-absorption artifacts, as judged by the intensities of the white line and EXAFS peaks.

Data analysis

Two to 12 XAFS scans per sample were calibrated to an Fe foil and merged using the program *SixPack* (Webb, 2005). The averaged spectra were imported into the program *Athena* (Ravel and Newville, 2005), normalized, and background subtracted using a cubic spline. Linear combination fitting was carried out using the LCF routine in *Athena* on windowed XANES spectra (7110−7160 eV). Raw and normalized intensity data were exported into the plotting program *Origin* 8.6 (OriginLab, Northampton, Massachusetts, USA), where baselines were removed for pre-edge peak identification, fitting, and integration using the Peak Analyzer routine.

Shell fitting of the aluminosilicate samples was carried out using the 6-shell montmorillonite model and 6-shell allophane nanoball model (Figure 1) following the approach described by Baker and Strawn (2012). Atomic coordinates for the montmorillonite model were taken from Tsipursky and Drits (1984) and coordinates for the nanoball model were taken from a section of the model nanoball described by Creton *et al.* (2008a). Paths were generated from the atomic coordinates using the program *Atoms* (Ravel, 2001) and shell fitting was carried out using the program *Artemis* (Ravel and Newville, 2005) (Table 2). In fitting, all path lengths were optimized. Debye-Waller XAFS factors were optimized for the first Fe-O shell, and fixed or constrained for the other backscattering paths.

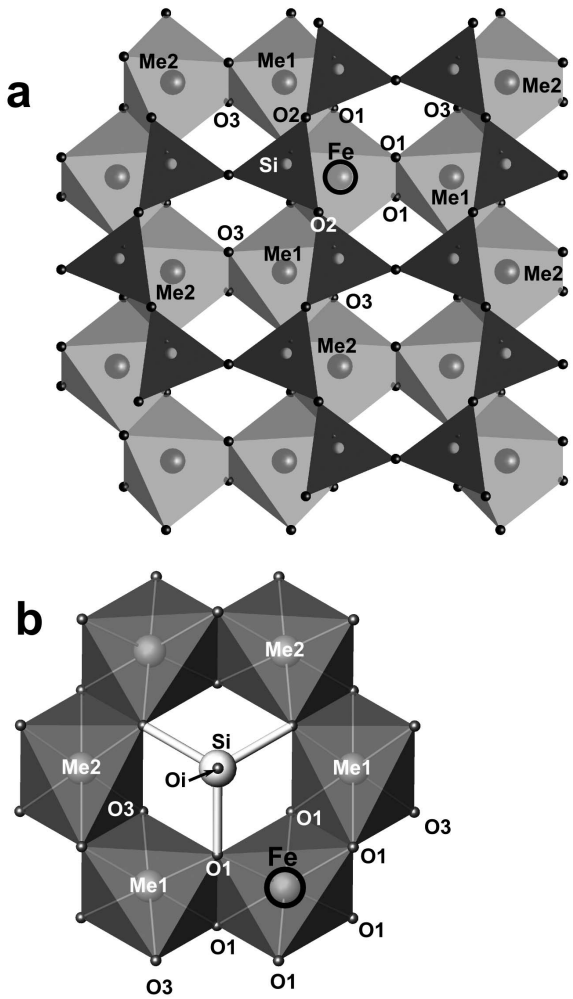

Figure 1. Illustration of modeled structures showing the locations of backscattering atoms. The central Fe atom is circled. (a) Montmorillonite structure (for simplicity, the bottom tetrahedral sheet is not shown). (b) Allophane octahedral structure with an unpolymerized Si tetrahedron. *Me*1 and *Me*2 are either Al or isomorphically substituted Fe atoms.

Table 2. Theoretical paths, coordination numbers (CN), and path lengths (R) generated using the program *FEFF* (Newville, 2001) for smectite and nanoball structural models. Smectite scattering paths were modeled using an *FEFF* input file created using *cis*-vacant crystal structure data from Tsipursky and Drits (1984), with Fe isomorphically substituted into an Al octahedral site. Nanoball scattering paths were modeled using an *FEFF* input file created using atomic coordinates for a section of the nanoball structure modeled by Creton *et al.* (2008a), as described by Baker and Strawn (2012). In fitting, Fe and Al coordination numbers were optimized, but constrained to sum to a total of three octahedral cations (NFe is the number of Fe atoms in the structure, $\leqslant 3$).

Smectite model		
1 tetrahedral sheet (2 tetrahedral sheets)		
Path	CN	R (Å)
Fe−O1	6	1.85−2.03
Fe−Fe1	NFe	2.88−3.05
Fe−Al1	3-NFe	2.88−3.05
Fe−Si1	2 (4)	3.16−3.18
Fe−O2	1 (2)	3.38
Fe−O3	6	3.65−3.81
Nanoball model		
Path	CN	R (Å)
Fe−O1	6	1.91−1.94
Fe−Fe1	NFe	2.99−3.13
Fe−Al1	3-NFe	2.99−3.13
Fe−Si1	3	3.15−3.16
Fe−Oi	3	3.51−3.71
Fe−O3	3	3.98−3.99

Octahedral sites in the two models were fitted with either Fe or Al, with the total number of Fe-Me1 backscatterers constrained to sum to three. The path length was optimized for the Fe-Si backscattering path, with the number of Si atoms fixed at 2 (smectite model) or 3 (nanoball model). For the allophane sample with Al:Si = 1:3, higher Si coordination numbers were also tested, as discussed in the shell-fitting section. The models included paths to O atoms coordinated to Si and the second shell of octahedral cations; the path lengths were optimized for these Fe−O2 and Fe−O3 shells, and Debye-Waller XAFS factors were optimized, but constrained to be equal to each other. Errors in the fitted bond distances are typically <0.02 Å, and errors in fitted first shell coordination number are typically <20%, and greater for second shells depending on how many backscatters are fit in the second shell and on the degree of disorder (O'Day *et al.*, 1994). Further details of the fitting procedure and of its refinement on well characterized clay-mineral standards were discussed by Baker and Strawn (2012).

The XAFS spectrum of Fe-sorbed synthetic allophane was fit using selected paths from the smectite model structure. The Fe−O1, Fe−Fe, and Fe−Si paths were used, with the Fe−Si path representing the distance between the allophane surface and adsorbed Fe (Table 3). Modeling of XAFS spectra cannot distinguish between Si and Al atoms, so the use of the Fe−Si path does not imply a particular bonding site for the Fe surface complex, or bonding specifically to either the nanosphere's interior or exterior surface. The fitting was carried out using the same approach as used for Fe-substituted allophanes, except for the use of only three paths.

RESULTS

Material synthesis and characterization

Allophanes at all Al:Si ratios were synthesized successfully with Fe up to 1 mol.% of Al (Table 1). Synthetic allophanes were not always stable to larger Fe contents. At Al:Si = 1:3, a stable gel could be formed with Fe = 10 mol.% of Al, but for Al:Si contents of 1:1 and 2:1, stable gels were not formed at this Fe content (either no gel formed at all or the gel dissolved during dialysis). A 1:1 allophane with Fe = 5 mol.% of Al was successfully produced. This composition is close to the value of 5 wt.% Fe_2O_3 suggested by Ossaka *et al.* (1971) as the upper limit of Fe substitution in allophane, although proto-imogolite allophanes with up to 20% of

Table 3. Fitting results for allophane samples. Variables optimized in fitting are annotated; in addition, all path lengths were optimized independently unless otherwise noted. Coordination numbers were fixed except where noted.

Smectite model

	2:1 allophane E0 = −3.10 – R factor = 0.014 –			1:1 allophane E0 = −2.41 – R factor = 0.017 –			1:3 allophane E0 = −4.20 – R factor = 0.017 –			Fe-sorbed allophane E0 = −4.01 – R factor = 0.012 –		
Path	CN	*R* (Å)	σ^2 (Å^2)	CN	*R* (Å)	σ^2 (Å^2)	CN	*R* (Å)	σ^2 (Å^2)	CN	*R* (Å)	σ^2 (Å^2)
Fe−O1	6	1.99	0.005[a]	6	2	0.004[a]	6	1.99	0.006	6	1.99	0.010[a]
Fe−Fe1	1.01[a]	3.03	0.005	1.83[a]	3.07	0.005	1.66[a]	3.02	0.005	1.33[a]	3.04	0.005
Fe−Al1	1.99[a]	2.96	0.005	1.17[a]	3.01	0.005	1.34[a]	3.01	0.005			
Fe−Si1	2	3.26	0.005	2	3.27	0.005	4	3.25	0.005	1	3.23	0.005
Fe−O2	1	3.42	0.008[b]	1	3.36	0.006[b]	2	3.24	0.014[b]			
Fe−O3	6	3.8	0.008[b]	6	3.82	0.006[b]	6	3.77	0.014[b]			

Nanoball model

	2:1 allophane E0 = −3.25 – R factor = 0.012 –			1:1 allophane E0 = −2.76 – R factor = 0.016 –			1:3 allophane E0 = −3.82 – R factor = 0.017 –		
Path	CN	*R* (Å)	σ^2 (Å^2)	CN	*R* (Å)	σ^2 (Å^2)	CN	*R* (Å)	σ^2 (Å^2)
Fe−O1	6	1.99	0.005[a]	6	1.99	0.004[a]	6	1.99	0.006[a]
Fe−Fe1	0.82[a]	3.04[a]	0.005	1.30[a]	3.08[a]	0.005	1.70[a]	3.11[a]	0.005
Fe−Al1	2.18[a]	2.98[a]	0.005	1.70[a]	2.97[a]	0.005	1.30[a]	2.97[a]	0.005
Fe−Si1	3	3.25	0.005	3	3.24	0.005	3	3.20	0.005
Fe−Oi	6	3.78	0.01[b]	6	3.79	0.01[b]	6	3.78	0.015[b]
Fe−O3	3	3.93	0.01[b]	3	3.92	0.01[b]	3	4.00	0.015[b]

[a] Value-optimized in fit.
[b] Values optimized but set to be equal within fit.
E0 is the phase shift and R factor is the relative error of the fit to the data.

the Al substituted by Fe were synthesized by McBride *et al.* (1984), compositions that could not be reproduced in the present study. The only results presented on synthetic allophanes here are from samples with substituted Fe = 1 mol.% of Al (Table 1).

Synthetic Fe-free 2:1 allophanes dissolved during the Fe sorption procedure. In the absence of aqueous Fe, samples of 2:1 allophane were not soluble in pH 3.5 solutions, suggesting that the Fe concentrations used in the sorption procedure contributed to allophane dissolution. The 1:1 and 1:3 Al:Si allophane compositions did not dissolve when Fe was adsorbed. In the present study, data on an Fe-sorbed allophane of 1:1 composition are presented in Table 1; no differences between the XAFS spectrum of this sample and that of an Fe-sorbed 1:3 allophane (data not shown) were observed.

The synthetic nanoparticles lacked strong XRD-detectable crystal structures, as is typical for allophane, although a broad peak centered at 26º2θ and a smaller peak centered at 40º2θ were consistent with features in published XRD scans of synthetic allophanes (Ossaka *et al.*, 1971; Ohashi *et al.*, 2002; Iyoda *et al.*, 2012; Levard *et al.*, 2012). Infrared spectroscopy of the synthetic and natural samples showed differences between allophane of different compositions (Figure 2, Table 1). Synthetic imogolite and Al:Si 2:1 allophane had IR spectra similar to those of the natural samples with the main Si–O stretching peaks near 990 and 920–950 cm^{-1}. The Al:Si 1:3 synthetic allophane had a main Si–O stretching band at much higher wavenumber, 1075 and 1180 cm^{-1}, with a small shoulder at 920 cm^{-1}. The intermediate Al:Si 1:1 allophane had a main Si–O stretching peak at 950 cm^{-1}, similar to that of 2:1 allophane, but with shoulders at 1050 and 1170 cm^{-1}, near that of 1:3 allophane, suggesting it contained a combination of proto-imogolite-like groups and more polymerized Si. This shift in the Si–O stretching peak with Al:Si ratio is consistent with published data on natural and synthetic allophane samples (Parfitt and Henmi, 1980).

The SEM images of the synthetic allophanes showed nanospherical structures ~5 nm in diameter (Figure 3a). These spheres could be resolved individually, but in most cases were present as larger aggregates. The nanosphere diameter was apparently unaffected by the Fe content of the allophanes. Images of synthetic imogolite showed tangles of long tubes ~5 nm in diameter and tens to hundreds of nm long (Figure 3b).

^{29}Si and ^{27}Al NMR spectra of synthetic Fe-allophanes with Al:Si = 1:1 (not shown) were identical to spectra of Fe-free synthetic samples with similar Al:Si ratios. In addition, NMR spectra of the synthetic allophanes examined here were comparable to the spectra of natural allophanes and previously studied synthetic allophanes with similar Al:Si ratios (Henmi and Wada, 1976; Barron *et al.*, 1982; Goodman *et al.*, 1985; Shimizu *et al.*, 1988; MacKenzie *et al.*, 1991).

XANES

Slight differences in the energy of the main edge step for different samples (1s to 4s transition, ~7124 eV (Waychunas *et al.*, 1983)) were indicative of differences in Fe coordination state (Figure 4a,b). The ferrihydrite

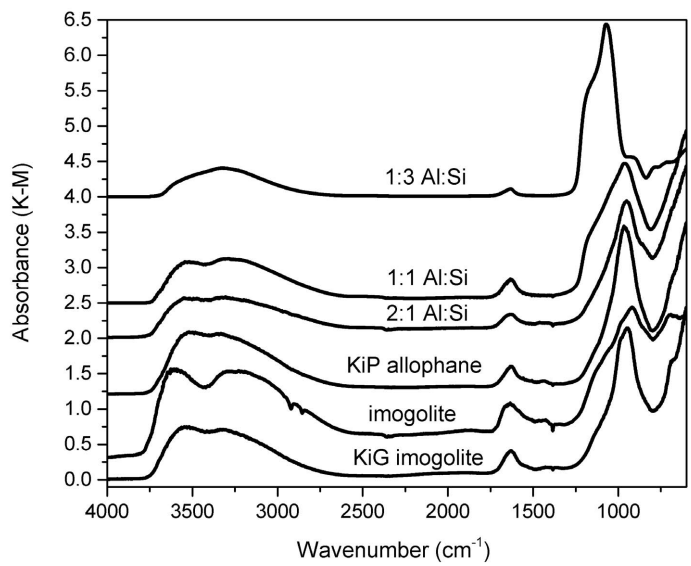

Figure 2. FTIR spectra for synthetic and natural allophane and imogolite samples. Synthetic imogolite and Al:Si 2:1 allophane have IR spectra similar to those of the natural samples with the main Si–O stretching peaks near 990 and 920–950 cm^{-1}. The Al:Si 1:3 synthetic allophane has a main Si–O stretching band at a much higher wavenumber, 1075 and 1180 cm^{-1}, with a small shoulder at 920 cm^{-1}. The intermediate Al:Si 1:1 allophane composition has a main Si–O stretching peak at 950, similar to that of 2:1 allophane, but with shoulders at 1050 and 1170 cm^{-1}, near that of 1:3 allophane, suggesting it contains a combination of proto-imogolite-like groups and more polymerized Si.

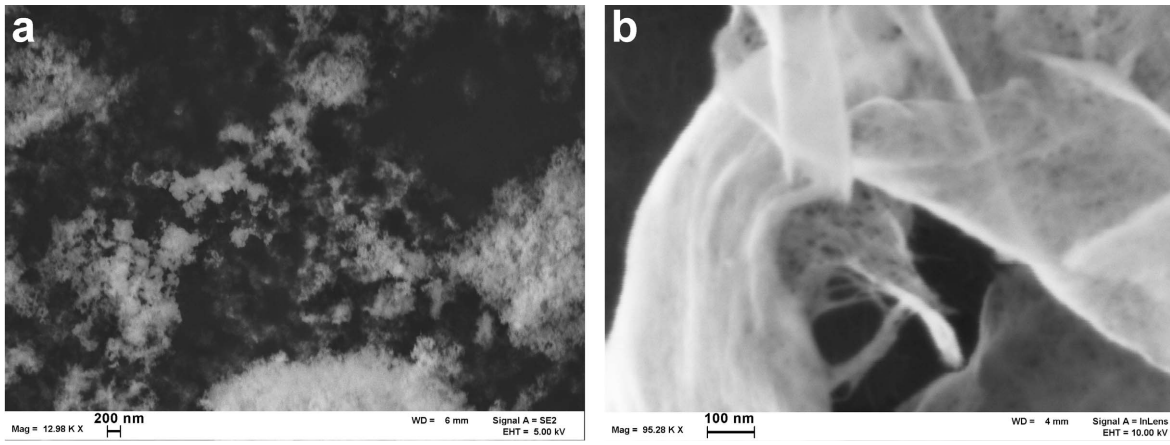

Figure 3. SEM images of synthetic (a) Fe-substituted 1:3 allophane, and (b) Fe-substituted imogolite.

reference sample had the lowest-energy step at 7123.1 eV, and the synthetic allophanes had the highest energy at 7124.5 eV. The natural samples, imogolite, and Fe-sorbed allophane had edge-step energies intermediate between those of ferrihydrite and synthetic allophanes. An additional inflection at 7132 eV (Figure 4a), which was clearly discernable as an additional peak in the first-derivative spectrum (Figure 4b), was present in the XANES spectra of Fe-substituted allophane samples. This peak is a distinctive feature observed in XANES spectra of Fe-substituted phyllosilicates (Baker *et al.*, 2010; Baker and Strawn, 2012), poorly developed in synthetic imogolite, and absent from the spectra of the natural samples, ferrihydrite, and Fe-sorbed allophanes (Figure 4b).

XANES pre-edge features

The pre-edge feature in the XANES spectrum arises from the 1s to 3d transition, and contains information about Fe valence, coordination state, and spin state (Waychunas *et al.*, 1983; Westre *et al.*, 1997; Galoisy *et al.*, 2001). In the normalized and baseline subtracted pre-edge region of the XANES spectrum (Figure 5), split pre-edge peaks at 7113.9 and 7115.4 eV observed in the allophanes with Al:Si of 1:1 and 1:3 were consistent with Fe(III) in high-spin octahedral coordination (Westre *et al.*, 1997), and had similar peak location and intensity to beidellite and nontronite clays (Baker and Strawn, 2012). The 2:1 allophane pre-edge was similar to the higher-Si allophanes, except that the higher-energy peak appeared ~0.4 eV lower. Pre-edge peak splitting was less distinct and peaks were more intense in natural allophane and imogolite samples, the synthetic imogolite, the Fe-adsorbed allophane, and the ferrihydrite.

EXAFS spectra

The EXAFS χ spectra of all allophane and imogolite samples were similar to one another (Figure 6a), although some differences were present. A shoulder at

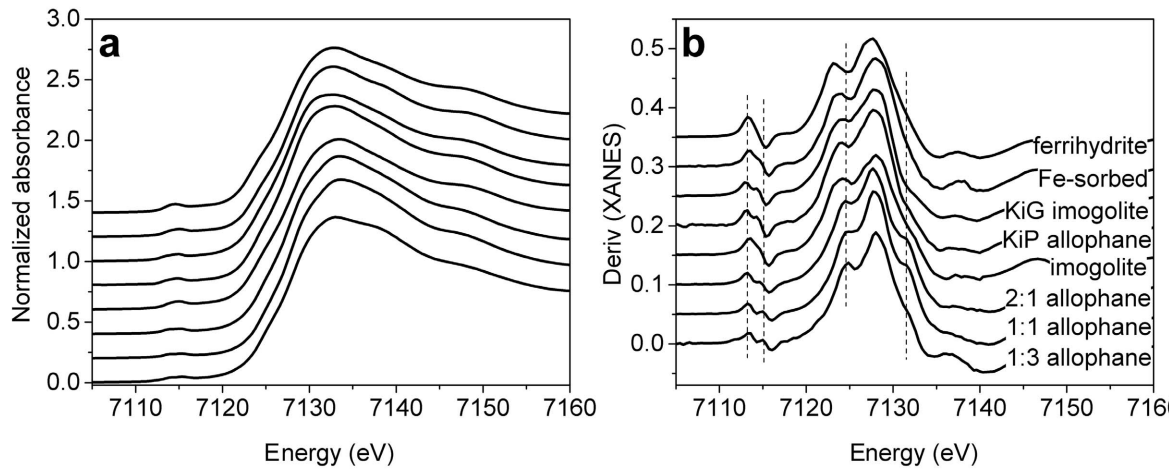

Figure 4. XANES spectra (a) and first-derivative spectra (b) for all samples. Dashed lines indicate the locations of peaks in the first-derivative spectra of synthetic allophanes.

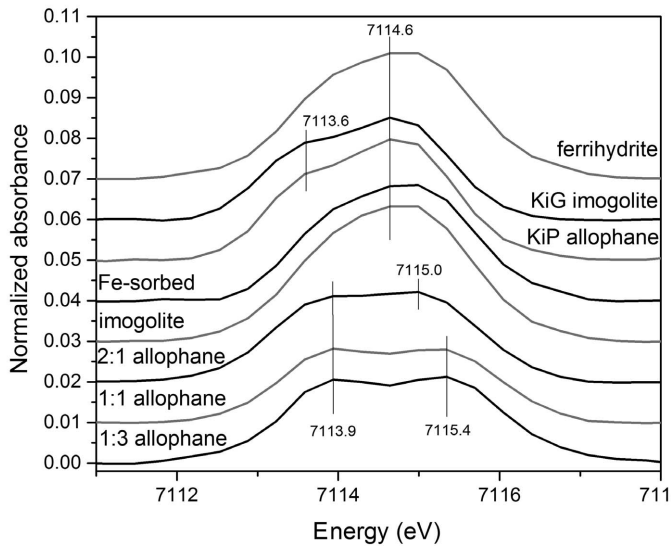

Figure 5. Pre-edge region of the normalized baseline-subtracted XANES spectra of all samples.

4 $Å^{-1}$ was obvious in the synthetic allophanes, and was slightly developed in imogolite, but was absent from ferrihydrite, Fe-sorbed allophane, and natural allophane and imogolite spectra. In the synthetic allophane EXAFS spectra, the shoulder at 5 $Å^{-1}$ and the peak centered near 7.5 $Å^{-1}$ were not as well developed as in the spectra of the other samples. The oscillation at 8.35 $Å^{-1}$ in synthetic allophanes shifted to 8.5 $Å^{-1}$ for all other samples.

The shoulder near 5 $Å^{-1}$ and the peak centered near 7.5 $Å^{-1}$ are indicative of the extent of Fe–Fe next-neighbor bonding in the mineral structure (Vantelon *et al.*, 2003). These features were well developed in the synthetic allophane samples, where Fe-Fe pairing was observed to be more extensive than in low-Fe montmorillonites (Baker and Strawn, 2012). This finding suggests that Fe was clustering in the substituted allophanes, which is surprising given the very low Fe contents of the allophanes being studied.

Fourier-transformed (FT) spectra of the samples (Figure 6b) revealed peak positions that represent the backscattering environment of the first and second shells, and some multiple scattering effects. The peak in the FT spectrum near 1.5 Å is due primarily to backscattering from the first O shell surrounding the Fe atoms (Fe−O1). Differences in Fe−O1 peak position between synthetic allophanes and other samples suggest small variations in Fe−O bond distances, which will be discussed further in the shell-fitting section below. The second peak in the FT, between 2.5 and 3.5 Å, contains information about several backscattering shells (Manceau *et al.*, 1988, 1990, 1998, 2000; Baker and Strawn, 2012). These include backscattering paths to adjacent octahedral cations (Fe−*Me*1, where *Me* is Fe or

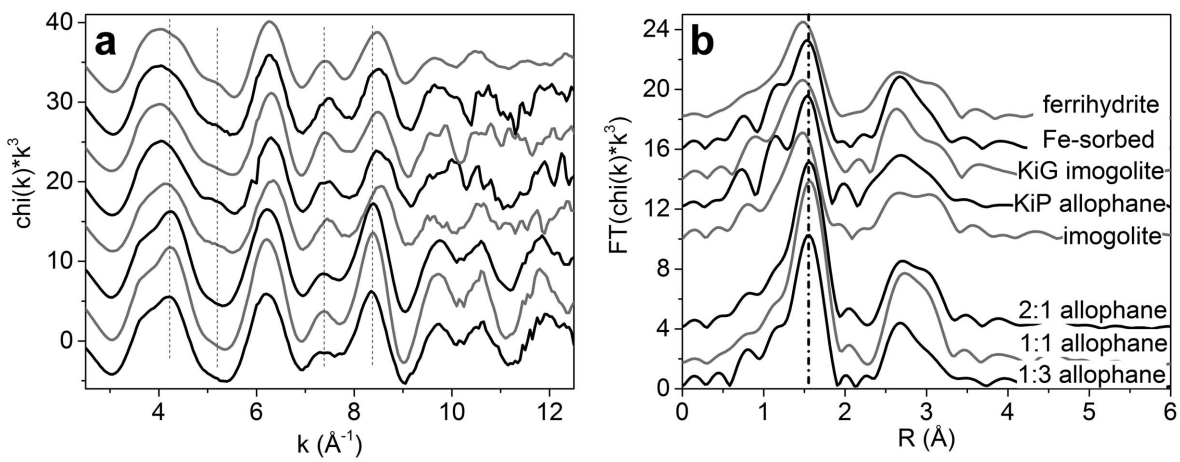

Figure 6. EXAFS χ spectra and FT spectra for all samples. Spectra are offset for clarity, but relative peak heights are to scale. Dashed lines indicate locations of peaks discussed in the text.

Al), to tetrahedral Si (or Al) atoms (Fe−Si1), and to octahedral and tetrahedral oxygen atoms at varying distances (Table 2). Multiple scattering paths can also occur in this range, but have only a small effect on the spectrum (Manceau *et al.*, 1998). Of all the possible backscattering paths, the Fe−Fe1 is the strongest signal that contributes to the FT peak at ~2.6 Å, and knowledge of the extent of the Fe−Fe next-neighbor bonding can be gleaned from this peak. However, peak amplitude is also affected by the extent of disorder in the sample, so care is necessary in constraining the Debye Waller factor and interpreting the coordination number.

The EXAFS spectra of the three synthetic allophane samples were similar to one another. The EXAFS spectra of the imogolite and natural allophanes showed subtle differences that may be used to interpret the local atomic structure of Fe in the samples. None of the samples had significant structure beyond 3.5 Å in the FT, as expected for poorly crystalline materials.

EXAFS shell fitting

Shell fitting of the EXAFS spectra from the synthetic allophanes was used to determine the local atomic structure around Fe in these samples. Because the natural samples and the synthetic imogolite appeared to contain a mixture of substituted and surface-adsorbed Fe, as discussed below, shell fitting was not carried out on spectra from those samples. Two models of Fe in an aluminosilicate structure were used to develop theoretical EXAFS paths: Fe substituted for octahedral Al in a montmorillonite structure, and Fe substituted for octahedral Al in a theoretical nanoball allophane model structure described by Creton *et al.* (2008a). These models, and the fitting approach, were described in a previous study (Baker and Strawn, 2012), which found that a 1:1 allophane composition could be fit using the smectite structure, whereas fits using the nanoball model converged to smectite-like path lengths.

Differences between theoretical local molecular structures in the smectite and nanoball models are subtle (Table 2). All paths to octahedral sheet atoms are similar (Fe−O1, Fe−*Me*1, and Fe−O3), although all the calculated path lengths are shorter for the nanoball model. The major differences between the theoretical models within a backscattering distance of ~4 Å are due to the Fe−Si1 and Fe−O2 paths: the smectite model contains only one tetrahedral sheet with two Si atoms and one O2 atom, whereas in the nanoball model three Si atoms and three associated Oi atoms are found (Figure 1).

Spectra of the three synthetic allophane compositions were fitted successfully using either the smectite or the nanoball model (Table 3). Results from using the two fit models for synthetic allophanes with a range of Al:Si ratios were similar to the 1:1 allophane fitted by Baker and Strawn (2012). The most noticeable differences between fits using the smectite and nanoball models were path lengths to the outermost oxygen atoms. Because the backscattering signal from these relatively distant atoms was not strong, the significance of these path-length differences was unclear. However, the convergence of both models to similar path lengths and Fe coordination numbers provides information about the local structure of Fe in the synthetic allophanes.

Fit-path lengths and coordination numbers for the 1:1 allophane using the smectite model (Table 3 and Figure 8) were similar to those reported by Baker and Strawn (2012). The nanoball model returned similar path lengths for all backscatterers except the outer oxygen shells, but an Fe coordination number of 1.3 (out of three total octahedral backscatterers), 30% less than the value fitted using the smectite model. This smaller NFe was a result of the additional Si backscatterer in the nanoball model. As discussed by Baker and Strawn (2012), fitting of EXAFS spectra alone does not provide sufficient information to completely delineate the structure of allophane, particularly with respect to Si coordination number.

The 1:3 allophane contained considerably more Si than the 1:1 allophane, and this Si must be accommodated somewhere within the structure. As noted above, the Si coordination number is difficult to constrain using shell fitting. Calculated Fe−Si backscattering path lengths were similar in the nanoball structure and in the layered smectite structure, suggesting that optimized path lengths will not be a useful indicator of silica accommodation in the allophane structure.

The 1:3 allophane spectrum was fitted successfully using either the nanoball or the smectite model (Table 3, Figure 8), although the quality of the smectite model fit was increased by including additional Si (in the form of two tetrahedral sheets rather than one). Interestingly, the smectite model fitted to the 1:3 allophane structure was the only model fitted in this study that did not show significant splitting between the Fe−Fe and Fe−Al path lengths. This fit produced an extremely short Fe−Oi path length, however, a result that is physically doubtful. Fitting the 1:3 allophane with the nanoball model produced a fit that was physically reasonable, with parameters resembling those obtained for the other allophane samples.

The 2:1 (proto-imogolite) allophane sample was the closest in composition to the theoretical nanoball allophane. However, the nanoball and smectite model fits were similar, with the fit quality slightly better in the nanoball model (Table 3, Figure 8).

The XANES and EXAFS spectra of Fe sorbed on allophane (Figures 5, 8) suggest that the Fe in this sample was present in structures with Fe−Fe edge-sharing bonds only (Toner *et al.*, 2009). Other Fe−Fe linkages found in more ordered ferrihydrites and in goethite, such as double corner-sharing bonds, are not present. The structure was, therefore, fitted using selected paths from the smectite model structure. A

noticeable second shell peak is present in the spectrum (Figure 6b), thus the NFe parameter was optimized to determine the extent of polynuclear complexation of adsorbed Fe.

Fitting of the first shell in the Fe-sorbed allophane suggests that Fe exists in a distorted octahedral site, as observed in ferrihydrite and aqueous Fe complexes (Pokrovski *et al.*, 2003; Toner *et al.*, 2009). In the best fit solution (Table 3, Figure 8), the relatively large Debye-Waller constant (σ^2) suggests a distorted first shell Fe−O. The shell can be fit equally well using two separate Fe−O paths of unequal length and smaller σ^2 value. The second shell path length fits to 3.04 Å, a typical distance for Fe oxyhydroxides (Toner *et al.*, 2009). The Fe−Fe coordination number in the second shell fits to 1.33, which suggests that some Fe adsorbed on this allophane sample may be present as dimers or multinuclear clusters sorbed on the surfaces of the allophane. The average distance from an individual sorbed Fe nucleus to the nearest Al or Si atom at the allophane surface was described in the model by the Fe−Si1 parameter, and optimized in modeling to 3.24 Å (Table 3).

DISCUSSION

Fe in synthetic allophanes

The XANES main-edge peak positions show that Fe in all the allophane and imogolite samples exists in a molecular environment distinct from that of Fe in ferrihydrite (Figures 4, 5). The XANES spectra of Fe in synthetic imogolite and in natural allophane resemble the spectrum of Fe adsorbed onto a synthetic allophane sample. Thus, Fe in the natural allophane sample, and in both the natural and synthetic imogolite, may be present partly as adsorbed Fe rather than in isomorphic substitution.

Examination of the pre-edge peaks suggested that the synthetic allophane samples did not contain ferrihydrite. The ferrihydrite pre-edge contained one intense peak at 7114.6 eV. Synthetic allophane samples displayed two pre-edge peaks with lower total intensity (Figure 5). The separation between the split peaks in the Fe-substituted synthetic allophane samples was 1.05−1.40 eV, typical of high-spin octahedral complexes (Westre *et al.*, 1997). The smaller split peak distances observed for natural allophane and imogolite (1 eV) and the synthetic imogolite and Fe-sorbed allophane samples (0.7 eV in deconvolved spectra) suggest that some or all of the Fe in these samples was in a different coordination environment than the Fe substituted in the synthetic allophanes.

The intensity and nature of the pre-edge peak in nontronites depends upon both Fe coordination (*i.e.* tetrahedral *vs*. octahedral) and Fe site geometry (*i.e.* degree of distortion) according to Manceau *et al.* (2000). Pre-edge peak height was used by Gates *et al.* (2002) as an index of tetrahedral Fe content. Allophanes were analyzed by Ildefonse *et al.* (1994) using ^{27}Al MAS NMR and Al K-edge XANES spectroscopy and those authors proposed that the high-Si allophanes had more tetrahedral Al than other allophanes. In the present study, the pre-edge peaks in 3:1 and 1:1 allophanes were of low intensity, comparable to that for beidellite and montmorillonite (Baker and Strawn, 2012). Such an observation suggests that Fe in these samples is in relatively undistorted sites with no tetrahedral Fe substitution. Proto-imogolite (2:1) allophane had a slightly more intense pre-edge peak than high-Si allophanes, and the imogolite pre-edge was still more intense. These observations suggest either that imogolite and 2:1 allophane had more distorted octahedral sites than high-Si allophanes, or that these samples contained some tetrahedral Fe.

The EXAFS spectra indicate that Fe in the synthetic Fe-substituted allophane samples is forming small clusters. This is indicated qualitatively by the development of the shoulder near 5 Å^{-1} and the peak centered near 7.5 Å^{-1} (Figure 6a), and quantitatively by the relatively large NFe values in the shell fits (Table 3). The NFe value indicates the average number of Fe next neighbors surrounding the central Fe atom. In a sample with 1 mol.% of Al replaced by Fe, if Fe is randomly distributed, most Fe atoms should be surrounded by Al atoms and should have no Fe next neighbors. Thus, for a random Fe distribution, this parameter should fit to a near-zero value. Fitted values between 0.82 and 1.83 suggest that Fe is forming small (2−6 atom) clusters within the allophane octahedral sheet (Baker and Strawn, 2012). The best-fit NFe values vary somewhat between the synthetic allophane samples, but do not vary systematically with the Al:Si ratio. Additional experiments, not described here, indicated no systematic change in NFe with sample age up to 2 y.

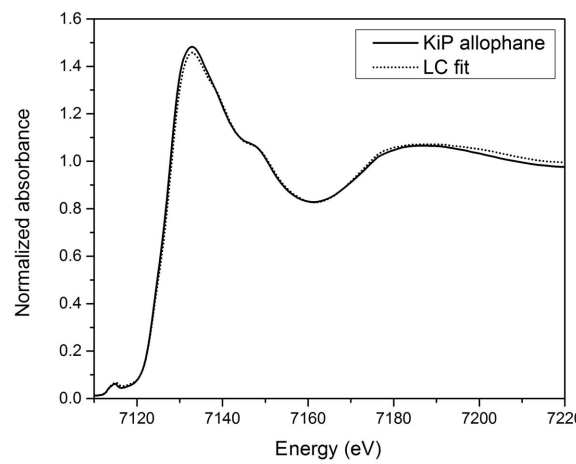

Figure 7. Linear combination fitting results for natural allophane: 85% Fe-substituted allophane, 15% Fe-sorbed allophane ($R^2 = 0.994$).

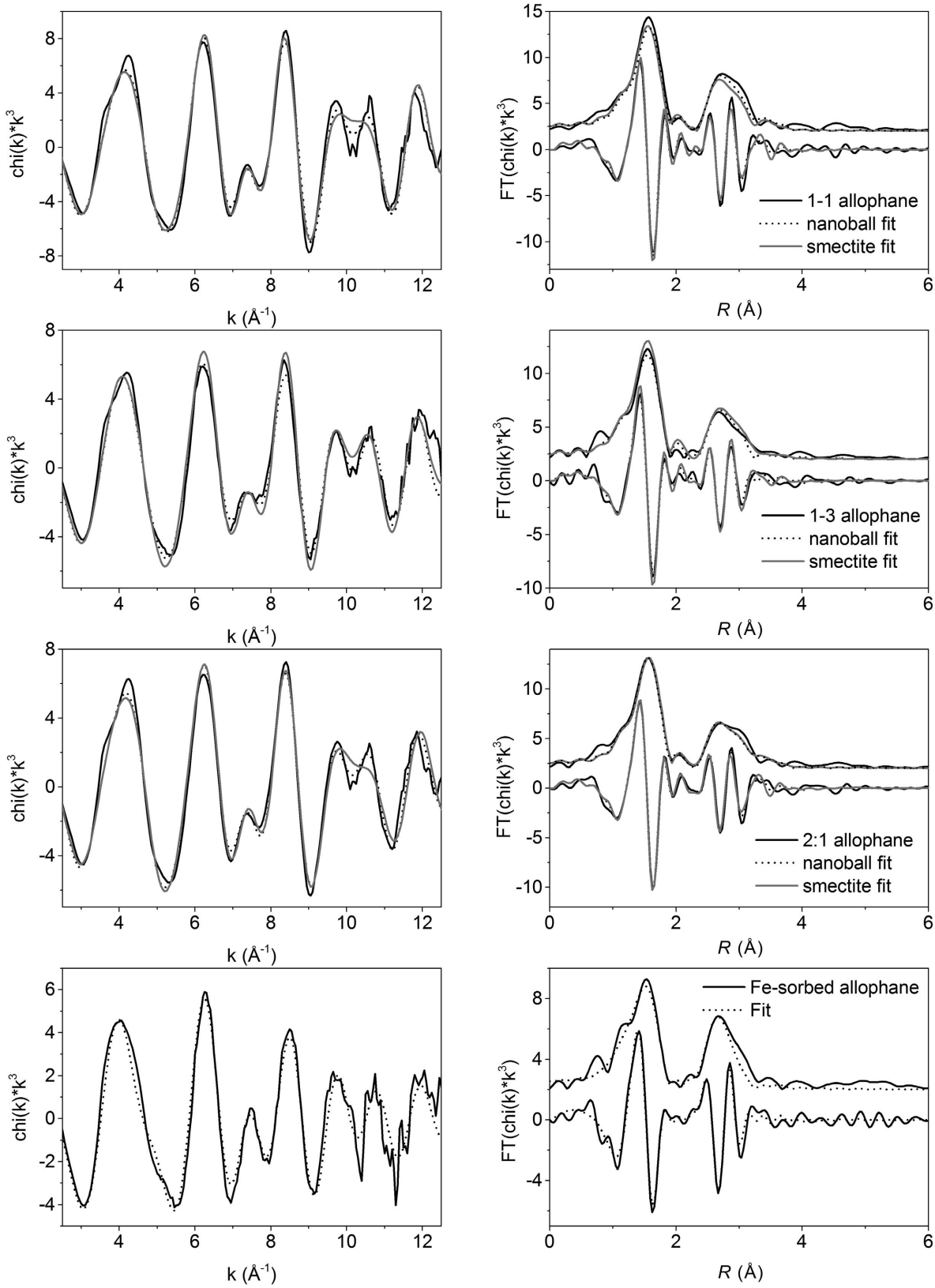

Figure 8. Shell-model fits to synthetic allophane spectra (FT magnitude offset from imaginary component for clarity) for nanoball and smectite models. Fit details given in Table 3.

Fe in synthetic imogolite and natural allophane and imogolite

Previous studies have found that Fe in natural allophane is a combination of isomorphically substituted Fe and some other form, typically described as a poorly crystalline ferrihydrite (Ossaka *et al.*, 1971; McBride *et al.*, 1984). In the present study, Fe K-edge XANES peak positions and splittings for the natural samples (KiG and KiP) and synthetic imogolite were unlike those of both ferrihydrite and Fe-substituted synthetic allophanes (Figures 4, 5). The spectra of the natural samples and of the synthetic imogolite resembled synthetic Fe-sorbed allophane samples most closely, suggesting that some Fe in the natural samples was present as a surface-sorbed phase.

To test the hypothesis that Fe in the natural samples is a combination of substituted and surface-sorbed Fe, the XANES spectrum of natural allophane was analyzed using linear combination fitting (LCF). The spectrum was modeled as a linear combination using synthetic Fe-substituted 2:1 allophane, synthetic Fe-sorbed allophane, and ferrihydrite as possible components. The LCF results for the KiG natural allophane sample indicated that the spectrum was best reproduced by a combination of 85% Fe-substituted allophane and 15% Fe-sorbed allophane (Figure 7). This is consistent with the finding of Ossaka *et al.* (1971) that Fe in synthetic allophane samples was present partly in isomorphic substitution for Al and partly as a surface-sorbed phase. Error estimates for XANES linear combination fits are on the order of 10−25% (Ostergren *et al.*, 1999; Roberts *et al.*, 2002; Ajiboye *et al.*, 2007).

Little information is available on the structure or properties of ferric iron sorbed to phyllosilicate surfaces. As discussed above, shell fitting of the Fe-sorbed allophane sample suggests small polynuclear clusters (NFe = 1.33) at a distance of 3.23 Å from an Al or Si atom at the allophane surface, and with an Fe−O distance of 1.99 Å. The geometry of possible sorption complexes on the aluminol surface suggests that this bond length is indicative of a bidentate (edge-sharing) bond to Al octahedra. These results suggest that the sorption behavior of Fe(III) on allophane is somewhat different from that of Cu(II), which was found to sorb to the octahedral sheet of allophane via a bridging bidentate bond, as well as *via* monodentate bonds at greater Cu loadings (Clark and McBride, 1984).

The presence of Si in aqueous solution inhibited the formation of double corner-sharing bonds in aqueous Fe complexes according to Pokrovski *et al.* (2003). In the Fe-sorption procedure used in the present study, small amounts of aqueous Si from dissolution of allophane may have inhibited the formation of more polymerized Fe linkages. This process may also enhance the substitution of small amounts of Fe in synthetic and natural allophanes by inhibiting the formation of a separate well ordered ferrihydrite phase. However, the Fe-allophane synthesis results described in the present study suggest that excess Fe in solution could also inhibit allophane formation in natural systems.

Allophane structure models

A fundamental challenge in defining the allophane structure is that allophanes range in composition from high-Al types, with Al:Si close to 2, to high-Si types, with Al:Si near 0.5. An imogolite-like nanoball allophane structure modeled by Creton *et al.* (2008a) has an Al:Si ratio of 2:1, with Si atoms in individual orthosilicate units bonded to a rolled octahedral Al sheet. If higher-Si allophanes form similar nanoballs, the structure must be modified to accommodate considerably more Si.

One proposed structure for high Si stream-deposit allophanes accommodates the excess Si in these materials in a fully polymerized tetrahedral sheet rolled with an incomplete octahedral sheet (Childs *et al.*, 1990). Defects in the octahedral sheet should be detectable in the EXAFS spectrum of octahedrally coordinated Fe. The shell-fitting results discussed above indicate that the synthetic allophane samples could all be fit successfully with a complete octahedral sheet (*e.g.* Fe−*Me*1 coordination number fixed at 3 (Table 3)). When octahedral coordination numbers were allowed to vary in the fit model, they never fit to values of <3. Thus, fitting of the structure around Fe atoms in the synthetic allophane samples shows no evidence of incomplete octahedral sheets in high-Si allophane compositions.

This result is in agreement with the observations from the XANES spectra. As discussed above, an inflection at 7132 eV is present in the XANES spectra of Fe-substituted allophanes. A previous study suggested that attenuation of this XANES feature in synthetic hematite nanoparticles is related to lattice distortions within 4 Å of the central absorbing atom, and that development of an intense peak requires several well ordered backscattering shells around the central site (Chen *et al.*, 2002). The presence of a well developed peak in the present allophane XANES data thus suggests that the synthetic allophane octahedral sheets were well ordered in the neighborhood of the isomorphically substituted Fe atoms.

The observation that the best fit models for the 2:1, 1:1, and 1:3 allophane samples were similar to one another suggests that considerable additional Si may be incorporated into the allophane structure without large changes in the fundamental structure of the particle. In particular, the structure of the octahedral sheet appears to be similar across the entire compositional range of the synthetic allophanes in the present study, suggesting a structure similar to the defect kaolin model proposed by MacKenzie *et al.* (1991), where a nanospherical particle contains both isolated orthosilicate units, as in imogolite, and sections of polymerized tetrahedral Si sheets, as in kaolinite.

Calculations suggest that tight rolling of the gibbsite sheet into nanotubular form in imogolite should result in some interatomic distances being shortened relative to the flat sheet (Gustafsson, 2001; Li *et al.*, 2008). This shortening of path lengths should also be observed in allophane nanospheres, in which the gibbsite sheet is also tightly rolled into a particle several nm in diameter. Such shortening was not observed by Baker and Strawn (2012) for 1:1 allophane, however, and was not observed in the fit results in the present study, where the Fe-*Me*1 fit distances were close to those calculated theoretically for the smectite model (Table 3). Why path lengths in allophane are not slightly shorter than those in smectite is unclear. An allophane model with polyhedral structure that had slightly curved faces rather than a sphere was proposed by Creton *et al.* (2008a). If allophane has such a polyhedral structure, that may explain why the interatomic distances observed in the present study are similar to those in flat octahedral sheets.

CONCLUSIONS

The results of the present study suggest that Fe in natural allophane and imogolite samples is present partly in isomorphic substitution for Al and partly as a surface-sorbed phase, but that ferrihydrite is not present in the samples studied. Spectra of synthetic allophanes suggest that the structure of the octahedral sheet is the same in high-Al and high-Si allophane, and that it is well ordered and similar to the octahedral sheet in smectite clays. Thus, the present results suggest a model of allophane structure in which one fundamental structural type, containing a complete octahedral sheet, can accommodate a range of Al:Si ratios.

High-Al allophanes could not be synthesized with large Fe contents (>1 mol.% of Al), and high-Al allophanes were found to dissolve during Fe sorption experiments. These observations suggest that the formation and stability of natural allophanes is affected by solution chemistry and ion sorption.

ACKNOWLEDGMENTS

The authors thank Alex Blumenfeld and Richard Williams for assistance with NMR spectroscopy, and Noriko Yamaguchi for sending allophane, imogolite, and pumice samples from Dr Hiradate's collection. Two anonymous reviewers provided helpful and constructive comments that improved the manuscript substantially. An Idaho Space Grant Consortium Research Initiation Grant provided funding for this work. Portions of this research were carried out at the Stanford Synchrotron Radiation Lightsource, a Directorate of SLAC National Accelerator Laboratory and an Office of Science User Facility operated for the U.S. Department of Energy Office of Science by Stanford University.

REFERENCES

Ajiboye, B., Akinremi, O.O., and Jürgensen, A. (2007) Experimental validation of quantitative XANES analysis for phosphorus speciation. *Soil Science Society of America Journal*, **71**, 1288–1291.

Baker, L.L. and Strawn, D.G. (2012) Fe K-edge XAFS spectra of phyllosilicates of varying crystallinity. *Physics and Chemistry of Minerals*, **39**, 675–684.

Baker, L.L., Strawn, D.G., Vaughan, K.L., and McDaniel, P.A. (2010) XAS study of Fe mineralogy in a chronosequence of soil clays formed in basaltic cinders. *Clays and Clay Minerals*, **58**, 772–782.

Barron, P., Wilson, M., Campbell, A.S., and Frost, R. (1982) Detection of imogolite in soils using solid state ^{29}Si NMR. *Nature*, **299**, 616–618.

Chen, L.X., Liu, T., Thurnauer, M.C., Csencsits, R., and Rajh, T. (2002) Fe_2O_3 nanoparticle structures investigated by X-ray absorption near-edge structure, surface modifications, and model calculations. *The Journal of Physical Chemistry B*, **106**, 8539–8546.

Childs, C.W., Parfitt, R.L., and Newman, R.H. (1990) Structural studies of Silica Springs allophane. *Clay Minerals* **25**, 329–341.

Clark, C. and McBride, M.B. (1984) Chemisorption of Cu (II) and Co (II) on allophane and imogolite. *Clays and Clay Minerals*, **32**, 4, 300–311.

Cradwick, P.D.G., Farmer, V.C., Russell, J.D., Masson, C.R., Wada, K., and Yoshinaga, N. (1972) Imogolite, a hydrated aluminum silicate of tubular structure. *Nature Physical Science*, **240**, 187–189.

Creton, B., Bougeard, D., Smirnov, K.S., Guilment, J., and Poncelet, O.G. (2008a) Structural model and computer modeling study of allophane. *Journal of Physical Chemistry C*, **112**, 358–364.

Creton, B., Bougeard, D., Smirnov, K.S., Guilment, J., and Poncelet, O. (2008b) Molecular dynamics study of hydrated imogolite. 1. Vibrational dynamics of the nanotube. *The Journal of Physical Chemistry C*, **112**, 10013–10020.

Farmer, V.C. (1997) Conversion of ferruginous allophanes to ferruginous beidellites at 95º under alkaline conditions with alternating oxidation and reduction. *Clays and Clay Minerals*, **45**, 591–597.

Farmer, V.C., Fraser, A.R., and Tait, J.M. (1977) Synthesis of imogolite: a tubular aluminium silicate polymer. *Journal of the Chemical Society, Chemical Communications*, **13**, 462–463.

Farmer, V.C., Fraser, A.R., and Tait, J.M. (1979) Characterization of the chemical structures of natural and synthetic aluminosilicate gels and sols by infrared spectroscopy. *Geochimica et Cosmochimica Acta*, **43**, 1417–1420.

Farmer, V.C., Krishnamurti, G., and Huang, P. (1991) Synthetic allophane and layer-silicate formation in SiO_2-Al_2O_3-FeO-Fe_2O_3-MgO-H_2O systems at 23ºC and 89ºC in a calcareous environment. *Clays and Clay Minerals*, **39**, 561–570.

Galoisy, L., Calas, G., and Arrio, M.A. (2001) High-resolution XANES spectra of iron in minerals and glasses: structural information from the pre-edge region. *Chemical Geology*, **174**, 307–319.

Gates, W.P., Slade, P.G., Manceau, A., and Lanson, B. (2002) Site occupancies by iron in nontronites. *Clays and Clay Minerals*, **50**, 223–239.

Goodman, B., Russell, J., Montez, B., Oldfield, E., and Kirkpatrick, R. (1985) Structural studies of imogolite and allophanes by aluminum-27 and silicon-29 nuclear magnetic resonance spectroscopy. *Physics and Chemistry of Minerals*, **12**, 342–346.

Gustafsson, J.P. (2001) The surface chemistry of imogolite. *Clays and Clay Minerals*, **49**, 73–80.

Henmi, T. and Wada, K. (1976) Morphology and composition of allophane. *American Mineralogist*, **61**, 379–390.

Hiradate, S. and Wada, S.-I. (2005) Weathering process of

volcanic glass to allophane determined by ^{27}Al and ^{29}Si solid-state NMR. *Clays and Clay Minerals*, **53**, 401–408.

Horikawa, Y. and Soezima, H. (1977) State analysis of iron in allophanic clays II: Iron L-emission band spectra from allophanic clays and hisingerite by the use of an X-ray microanalyzer. *Clay Science*, **5**, 97–102.

Ildefonse, P., Kirkpatrick, R.J., Montez, B., Calas, G., Flank, A.M., and Lagarde, P. (1994) ^{27}Al MAS NMR and aluminum X-ray absorption near edge structure study of imogolite and allophanes. *Clays and Clay Minerals*, **42**, 276–287.

Iyoda, F., Hayashi, S., Arakawa, S., John, B., Okamoto, M., Hayashi, H., and Yuan, G. (2012) Synthesis and adsorption characteristics of hollow spherical allophane nano-particles. *Applied Clay Science*, **56**, 77–83.

Joussein, E., Petit, S., Churchman, J., Theng, B., Righi, D., and Delvaux, B. (2005) Halloysite clay minerals – a review. *Clay Minerals*, **40**, 383–426.

Kaufhold, S., Kaufhold, A., Jahn, R., Brito, S., Dohrmann, R., Hoffmann, R., Gliemann, H., Weidler, P., and Frechen, M. (2009) A new massive deposit of allophane raw material in Ecuador. *Clays and Clay Minerals*, **57**, 72–81.

Kaufhold, S., Ufer, K., Kaufhold, A., Stucki, J.W., Anastácio, A.S., Jahn, R., and Dohrmann, R. (2010) Quantification of allophane from Ecuador. *Clays and Clay Minerals*, **58**, 707–716.

Kawano, M. and Tomita, K. (2001) Microbial biomineralization in weathered volcanic ash deposit and formation of biogenic minerals by experimental incubation. *American Mineralogist*, **86**, 400–410.

Kitagawa, Y. (1973) Substitution of aluminum by iron in allophane. *Clay Science*, **4**, 151–154.

Levard, C., Rose, J., Thill, A., Masion, A., Doelsch, E., Maillet, P., Spalla, O., Olivi, L., Cognigni, A., Ziarelli, F., and Bottero, J.Y. (2010) Formation and growth mechanisms of imogolite-like aluminogermanate nanotubes. *Chemistry of Materials*, **22**, 2466–2473.

Levard, C., Masion, A., Rose, J., Doelsch, E., Borschneck, D., Olivi, L., Chaurand, P., Dominici, C., Ziarelli, F., Thill, A., Maillet, P., and Bottero, J.Y. (2011) Synthesis of Ge-imogolite: influence of the hydrolysis ratio on the structure of the nanotubes. *Physical Chemistry Chemical Physics*, **13**, 14516–14522.

Levard, C., Doelsch, E., Basile-Doelsch, I., Abidin, Z., Miche, H., Masion, A., Rose, J., Borschneck, D., and Bottero, J.Y. (2012) Structure and distribution of allophanes, imogolite and proto-imogolite in volcanic soils. *Geoderma*, **183–184**, 100–108.

Li, L., Xia, Y., Zhao, M., Song, C., Li, J., and Liu, X. (2008) The electronic structure of a single-walled aluminosilicate nanotube. *Nanotechnology*, **19**, 175702.

MacKenzie, K.J.D. and Cardile, C.M. (1988) The structure and thermal reactions of natural iron-containing allophanes studied by 57-Fe Mössbauer spectroscopy. *Thermochimica Acta*, **130**, 259–267.

MacKenzie, K., Bowden, M., and Meinhold, R. (1991) The structure and thermal transformations of allophanes studied by 29Si and 27Al high resolution solid-state NMR. *Clays and Clay Minerals*, **39**, 337–346.

Manceau, A., Bonnin, D., Kaiser, P., and Frétigny, C. (1988) Polarized EXAFS of biotite and chlorite. *Physics and Chemistry of Minerals*, **16**, 180–185.

Manceau, A., Bonnin, D., Stone, W.E.E., and Sanz, J. (1990) Distribution of Fe in the octahedral sheet of trioctahedral micas by polarized EXAFS; comparison with NMR results. *Physics and Chemistry of Minerals*, **17**, 363–370.

Manceau, A., Chateigner, D., and Gates, W.P. (1998) Polarized EXAFS, distance-valence least-squares modeling (DVLS), and quantitative texture analysis approaches to the structural refinement of Garfield nontronite. *Physics and Chemistry of Minerals*, **25**, 347–365.

Manceau, A., Lanson, B., Drits, V.A., Chateigner, D., Gates, W.P., Wu, J., Huo, D., and Stucki, J.W. (2000) Oxidation-reduction mechanism of iron in dioctahedral smectites: I. Crystal chemistry of oxidized reference nontronites. *American Mineralogist*, **85**, 133–152.

McBride, M.B., Farmer, V.C., Russell, J.D., Tait, J.M., and Goodman, B.A. (1984) Iron substitution in aluminosilicate sols synthesized at low pH. *Clay Minerals*, **19**, 1–8.

Ming, D.W., Mittlefehldt, D.W., Morris, R.V., Golden, D.C., Gellert, R., Yen, A., Clark, B.C., Squyres, S.W., Farrand, W.H., Ruff, S.W., Arvidson, R.E., Klingelhöfer, G., McSween, H.Y., Rodionov, D.S., Schröder, C., de Souza, P.A., Jr., and Wang, A. (2006) Geochemical and mineralogical indicators for aqueous processes in the Columbia Hills of Gusev crater, Mars. *Journal of Geophysical Research*, **111**, DOI: 10.1029/2005JE002560.

Miyauchi, N. and Aomine, S. (1966) Mineralogy of gel-like substance in the pumice bed in Kanuma and Kitakami Districts. *Soil Science and Plant Nutrition*, **12**, 19–22.

Montarges-Pelletier, E., Bogenez, S., Pelletier, M., Razafitianamaharavo, A., Ghanbaja, J., Lartiges, B., and Michot, L. (2005) Synthetic allophane-like particles: textural properties. *Colloids and Surfaces A: Physicochemical and Engineering Aspects*, **255**, 1–10.

Newville, M. (2001) IFEFFIT: interactive XAFS analysis and FEFF fitting. *Journal of Synchrotron Radiation*, **8**, 322–324.

O'Day, P.A., Rehr, J.J., Zabinsky, S.I., and Brown, G.E., Jr. (1994) Extended X-ray absorption fine structure (EXAFS) analysis of disorder and multiple-scattering in complex crystalline solids. *Journal of the American Chemical Society*, **116**, 2938–2949.

Ohashi, F., Wada, S.-I., Suzuki, M., Maeda, M., and Tomura, S. (2002) Synthetic allophane from high-concentration solutions: nanoengineering of the porous solid. *Clay Minerals*, **37**, 451–456.

Ookawa, M., Inoue, Y., Watanabe, M., Suzuki, M., and Yamaguchi, T. (2006) Synthesis and characterization of Fe containing imogolite. *Clay Science*, **12**, Suppl. 2, *Claysphere*, 280–284.

Ossaka, J., Iwai, S.-i., Kasai, M., Shirai, T., and Hamada, S. (1971) Coexistence states of iron in synthesized iron-bearing allophane (Al_2O_3-SiO_2-Fe_2-H_2O system). *Bulletin of the Chemical Society of Japan*, **44**, 716–718.

Ostergren, J.D., Brown, G.E., Parks, G.A., and Tingle, T.N. (1999) Quantitative speciation of lead in selected mine tailings from Leadville, CO. *Environmental Science & Technology*, **33**, 1627–1636.

Parfitt, R.L. (2009) Allophane and imogolite: role in soil biogeochemical processes. *Clay Minerals*, **44**, 135–155.

Parfitt, R.L. and Henmi, T. (1980) Structure of some allophanes from New Zealand. *Clays and Clay Minerals*, **28**, 285–294.

Parfitt, R.L., Furkert, R.J., and Henmi, T. (1980) Identification and structure of two types of allophane from volcanic ash soils and tephra. *Clays and Clay Minerals*, **28**, 328–334.

Pokrovski, G.S., Schott, J., Farges, F., and Hazemann, J.-L. (2003) Iron (III)-silica interactions in aqueous solution: insights from X-ray absorption fine structure spectroscopy. *Geochimica et Cosmochimica Acta*, **67**, 3559–3573.

Rampe, E., Kraft, M., Sharp, T., Golden, D., Ming, D., and Christensen, P. (2012) Allophane detection on Mars with Thermal Emission Spectrometer data and implications for regional-scale chemical weathering processes. *Geology*, G33215.33211.

Ravel, B. (2001) ATOMS: crystallography for the X-ray absorption spectroscopist. *Journal of Synchrotron*

Radiation, **8**, 314–316.

Ravel, B. and Newville, M. (2005) ATHENA, ARTEMIS, HEPHAESTUS: data analysis for X-ray absorption spectroscopy using IFEFFIT. *Journal of Synchrotron Radiation*, **12**, 537–541.

Roberts, D.R., Scheinost, A.C., and Sparks, D.L. (2002) Zinc speciation in a smelter-contaminated soil profile using bulk and microspectroscopic techniques. *Environmental Science & Technology*, **36**, 1742–1750.

Schwertmann, U., Friedl, J., and Kyek, A. (2004) Formation and properties of a continuous crystallinity series of synthetic ferrihydrites (2- to 6-line) and their relation to FeOOH forms. *Clays and Clay Minerals*, **52**, 221–226.

Shimizu, H., Watanabe, T., Henmi, T., Masuda, A., and Saito, H. (1988) Studies on allophane and imogolite by high-resolution solid-state ^{29}Si-and ^{27}Al-NMR and ESR. *Geochemical Journal*, **22**, 23–31.

Tazaki, K., Morikawa, T., Watanabe, H., Asada, R., and Okuno, M. (2006) Microbial formation of imogolite. *Clay Science*, **12**, Supplement 2, 245–254.

Toner, B.M., Santelli, C.M., Marcus, M.A., Wirth, R., Chan, C.S., McCollom, T., Bach, W., and Edwards, K.J. (2009) Biogenic iron oxyhydroxide formation at mid-ocean ridge hydrothermal vents: Juan de Fuca Ridge. *Geochimica et Cosmochimica Acta*, **73**, 388–403.

Tsipursky, S.I. and Drits, V.A. (1984) The distribution of octahedral cations in the 2:1 layers of dioctahedral smectites studied by oblique-texture electron diffraction. *Clay Minerals*, **19**, 177–193.

Vantelon, D., Montarges-Pelletier, E., Michot, L.J., Pelletier, M., Thomas, F., and Briois, V. (2003) Iron distribution in the octahedral sheet of dioctahedral smectites. An Fe K-edge X-ray absorption spectroscopy study. *Physics and Chemistry of Minerals*, **30**, 44–53.

Waychunas, G.A., Apted, M.J., and Brown, G.E. (1983) X-ray K-edge absorption spectra of Fe minerals and model compounds: Near-edge structure. *Physics and Chemistry of Minerals*, **10**, 1–9.

Webb, S.M. (2005) Sixpack: A graphical user interface for XAS analysis using IFEFFIT. *Physica Scripta*, **T115**, 1011–1014.

Westre, T.E., Kennepohl, P., DeWitt, J.G., Hedman, B., Hodgson, K.O., and Solomon, E.I. (1997) A multiplet analysis of Fe K-edge 1s → 3d pre-edge features of iron complexes. *Journal of the American Chemical Society*, **119**, 6297–6314.

Yucelen, G.I., Choudhury, R.P., Vyalikh, A., Scheler, U., Beckham, H.W., and Nair, S. (2011) Formation of single-walled aluminosilicate nanotubes from molecular precursors and curved nanoscale intermediates. *Journal of the American Chemical Society*, **133**, 5397–5412.

(*Received 3 July 2013; revised 15 February 2014; AE: A. Thompson; Ms. 787*)

Clays and Clay Minerals, Vol. 62, No. 1, 35–52, 2014.

NATURAL CLAY-SIZED GLAUCONITE IN THE NEOGENE DEPOSITS OF THE CAMPINE BASIN (BELGIUM)

R. ADRIAENS*, N. VANDENBERGHE, AND J. ELSEN

Applied Geology and Mineralogy, Department of Earth and Environmental Sciences, University of Leuven, Celestijnenlaan 200E, 3000 Leuven, Belgium

Abstract—Natural clay-sized glauconite has the same mineralogical composition as sand-sized glauconite pellets but occurs in <2 μm clay fractions. This particular glauconite habit has been described previously from soil environments resulting from pelletal weathering but is rarely reported in higher-energy sedimentary environments. In the present study, clay-sized glauconite was identified as a common constituent in transgressive Neogene glauconite pellet-rich deposits of the southern North Sea in Belgium. X-ray diffraction results revealed that the characteristics of the clay-sized glauconite are very similar to the associated glauconite pellets in sand deposits. Both glauconite types consisted of two glauconite-smectite R1 phases with generally small percentages of expandable layers (<30%) with d_{060} values ranging between 1.513 Å and 1.519 Å. Clay-sized glauconite was not neoformed but formed by the disintegration of sand-sized glauconite pellets which were abraded or broken up during short-distance transport within the sedimentary basin or over the hinterland. Even in an environment where authigenic glauconite pellets occur, minimal transport over transgressive surfaces is sufficient to produce clay-sized glauconite. Furthermore, clay-sized glauconite can be eroded from marine deposits and subsequently resedimented in estuarine deposits. Clay-sized glauconite is, therefore, a proxy for the transport intensity of pelletal glauconite in energetic depositional environments and, moreover, indicates reworking in such deposits which lack pelletal glauconite.

Key Words—Belgium, Clay-sized Glauconite, Neogene, Transport.

INTRODUCTION

Authigenic glauconite is a sensitive indicator of low sedimentation rates in the marine realm and constitutes a powerful tool for sedimentological and sequence stratigraphic interpretations as well as K-Ar dating studies (Chamley, 1989; Amorosi, 1995; Hesselbo and Huggett, 2001; Potter *et al.*, 2005; El Albani, 2005; Harris *et al.*, 2007; Derkowski *et al.*, 2009). Many deposits contain transported glauconite pellets, which drastically changes the interpretation of environmental conditions during deposition (McRae, 1972; Odin and Matter, 1981; Cudzil and Dreise, 1987; Odin and Fullagar, 1988; Chafetz and Reid, 2000; Gonzalez *et al.*, 2004).

Physical transport of glauconite pellets leads to pellet abrasion, large amounts of fragmented particles (Amorosi, 1997; Udgata, 2007), or even complete disintegration of clay flakes resulting in the production of clay-sized glauconite material. This process has been identified in soils where the clay fraction consists predominantly of a glauconite mineralogy (Van Ranst and De Coninck, 1983; Tedrow, 1986, 2002).

Clay-sized glauconite in sedimentary rocks was suggested by Baioumy and Boulis (2012) to represent a pre-pelletal stage during glauconitization. Depending on its compositional and sedimentological characteristics, clay-sized glauconite has a transported origin, indicative of a rather high-energy environment or an authigenic origin, indicative of a lower-energy depositional environment. Clay-sized glauconite is, however, almost never reported in sedimentary deposits and certainly not co-existing with pelletal glauconite.

The current study documents the common presence of such clay-sized glauconite in Neogene glauconite-pellet-rich deposits of the southern North Sea in Belgium (Campine basin). First, experiments were performed to evaluate disintegration behavior of glauconite particles during several types of sample treatment. Second, a methodology was established to investigate the mineralogy of both glauconite pellets and associated clay-sized fractions. The study further addressed the relationship between sand-sized glauconite pellets and clay-sized glauconite, along with the origin and sedimentological significance of the latter.

CRITERIA TO IDENTIFY AND QUANTIFY GLAUCONITE MINERALS

Standard reference mineralogy and chemistry of glauconite pellets

The mineral glauconite is an Fe-rich dioctahedral mica which can be formed in various ways, with tetrahedral Al^{3+} or Fe^{3+} >0.2 atoms per formula unit and octahedral R^{3+} >1.2 atoms. A generalized formula is $K(R^{3+}_{1.33}R^{2+}_{0.67})(Si_{3.67}Al_{0.33})O_{10}(OH)_2$ with Fe^{3+} > Al and Mg > Fe^2 (Bailey,1980). The d_{060} values must be

* E-mail address of corresponding author:
rieko.adriaens@ees.kuleuven.be
DOI: 10.1346/CCMN.2014.0620104

>1.510 Å and K^+ should be the dominant interlayer cation (Bailey, 1988). The mineralogy of glauconite pellets, however, seldom consists of the pure glauconite mica. Instead, one or more Fe-rich mixed-layered glauconite-smectite phases are encountered (Buckley *et al.*, 1978; El Albani, 2005; Adriaens, 2009; Baldermann *et al.* 2012). Al-rich glauconite species were also reported by Berg-Madsen (1983) and Weaver and Pollard (1973), however. The composition of Al-rich glauconite overlaps with that of Fe-illite, which is related to non-marine environments (Meunier, 2005; Meunier and El Albani, 2007), although Banerjee *et al.* (2008) claimed the presence of Fe-illite in a marine succession. Nevertheless, marine Al-rich glauconite, or Fe-illite, is the result of diagenetic alteration (Odin and Matter, 1981; Ireland *et al.*, 1983) and neither is found in unlithified sediments. Consequently, illitic mineral species with >15 wt.% total Fe, which is expressed by d_{060} values >1.51 Å, are termed glauconite or glauconite-smectite here (Velde, 1985; Meunier, 2005).

Identifying and quantifying clay-sized glauconite in mixtures of clay minerals

As discussed above, the identification of glauconite minerals is based on both mineralogical and chemical data in cases of pure minerals. In clay-mineral mixtures, however, the situation is often much more complex and the use of chemical characterization methods is less straightforward. Deriving mineralogical information and parameters from X-ray diffraction (XRD) patterns combined with detailed XRD clay modeling is, therefore, the optimal working method.

As stated by Moore and Reynolds (1997), the cation size and site occupancy of the dominant octahedral trivalent cation correlates with the d_{060} peak position. Furthermore, when considering the general stability of the 060 area in terms of structural and chemical variations common for clays, this area represents a valuable and reliable tool in X-ray powder diffractometry to distinguish between different clay species (Środoń *et al.*, 2001). Consequently, the d_{060} values of different illitic 10 Å species are positioned at, or lower than, 1.500 Å for normal illite, between 1.500 Å and 1.510 Å for Fe-rich illite, and >1.510 Å for glauconite. This clear-cut differentiation can be obscured in mixtures of glauconite and nontronite which are rarely reported and absent from the present setting.

GEOLOGICAL SETTING

During the Neogene, sedimentation is restricted to the Campine area in the northern part of Belgium (Figure 1).

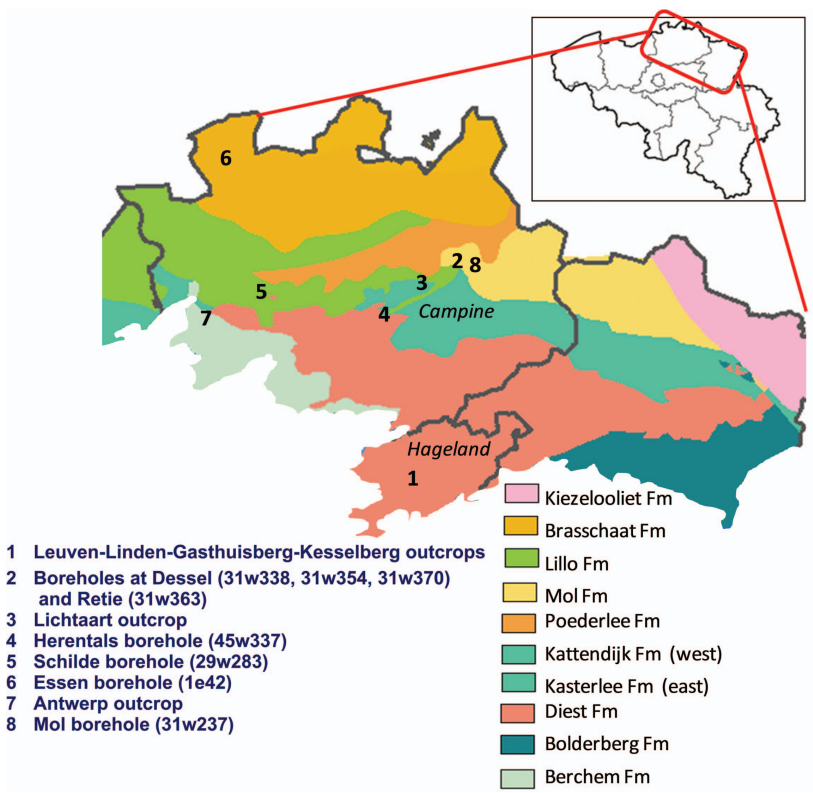

Figure 1. Geographical locations of out-crop or bore-hole samples plotted on the Tertiary geological map of the northern part of Belgium. The out-cropping formations presented here are indexed at the bottom right. Bore-hole codes correspond to codes of the Belgian Geological Survey.

Figure 2. (left) Glauconitic sands of the Diest Formation intercalated with thin, irregular clay layers. (right) Slightly glauconitic sands of the Kasterlee Formation with thin clay intercalations.

Deposits are mainly transgressive shallow-marine glauconite-rich sands but minor estuarine to fluvial sand deposits occur also (Vandenberghe *et al.*, 1998; 2004). Clay in these deposits occurs dispersed in the sand matrix and as thin intercalated clay layers (Figure 2). Depositional sequences are separated by erosion surfaces, interpreted as major stratigraphic unconformities. The chronostratigraphic position of the different units is based on Vandenberghe *et al.* (1998) and Louwye *et al.* (2000) (Table 1).

The Early Miocene sands of the Berchem Formation are subdivided in the Burdigalian Edegem and Kiel sand Members and the Langhian-Serravalian Antwerp sand Member (De Meuter and Laga, 1976), which were all deposited in a fully marine environment (De Meuter and Laga, 1976; Louwye and Laga, 1998; Louwye, 2001). These three members are fine- to medium-grained sand units commonly intercalated with thin clay layers (Vandenberghe *et al.*, 1998; Louwye *et al.*, 2000; Louwye, 2005). Distinction is made based on calcareous fossils, dinoflagellate biozonations, and glauconite contents (Table 1). Radiometric glauconite dating led Odin *et al.* (1974) to conclude an authigenic origin for the Antwerp glauconites while the Edegem and Kiel glauconites are considered to be reworked.

After an important phase of erosion, sedimentation only restarted in the latest Serravalian–early Tortonian with the Diest Formation (Louwye *et al.*, 1999). This poorly sorted sand unit occurs in both the Hageland and the Campine area with average glauconite contents of

Table 1. Stratigraphical overview of the Neogene units investigated in the present study, their average pelletal glauconite contents, and the potential of each unit to contain authigenic glauconites.

Chronostratigraphy	– Lithostratigraphic unit – Formation	Member	Average Gl content	Authigenic Gl potential
Zanclean/ Piacenzian	Mol Formation / Poederlee Formation		<0.01% / 20%	very low / medium
Messinian	Kasterlee Formation		3%	very low
Tortonian	Diest Formation		39%	very low
Serravallian				
Langhian		Antwerp Member	50%	medium
Burdigalian	Berchem Formation	Kiel Member	35%	low
		Edegem Member	35%	low

40% (Figure 1 and Table 1). Discontinuous clay layers are commonly observed in these sands (Figure 2). The Diest sands in the Hageland area contain no microfossils, which makes their exact stratigraphic positioning questionable.

The Late Miocene Kasterlee Formation was formed in a near-shore depositional environment or embayment with a manifest river discharge and was, thus, influenced by oxic freshwaters (Louwye, 2005; Louwye *et al.*, 2006). This resulted in a well sorted, fine-grained sand unit with thin irregular clay intercalations (Figure 2). Glauconite contents in the Kasterlee Formation are typically much smaller than the older Miocene sand deposits, with typical values of only 5%.

The Pliocene Poederlee sand is a fine glauconitic sand unit with disperse clay lenses (De Meuter and Laga, 1976) often presented as highly oxidized sands with a hard limonitic crust. Louwye and De Schepper (2010) suggest a near-coastal, possibly shoaling environment, with more terrestrial influence in the upper part of the formation. Glauconite contents in the Poederlee sands are variable, ranging from 5 to 30%.

A thick unit of continental to estuarine sands of the Mol Formation occurs geographically more to the east (Figure 1). This unit consists of very quartz-rich glass sands with very small clay contents and contains virtually no glauconite pellets.

Under a binocular microscope, glauconite pellets in the sand units described above generally appear pale to dark green, with the latter variety occurring more frequently. Pellets are often well rounded and polished but also more irregular pellet shapes occur. Cracks in pellets and broken fragments are commonly observed (Figure 3). The spatial distribution of glauconite pellets is often very irregular as they occur concentrated in cross beds, on transgressive surfaces, and in basal green sands but also dispersed in the sand matrix. When mixed with water, the suspension water of sand deposits displays a pronounced green coloration. However, the suspension water of sedimentary clay is grey to brown colored and rarely contains any glauconite pellets.

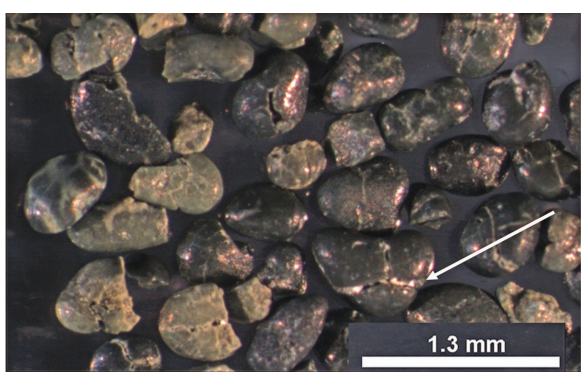

Figure 3. Glauconite pellets of the Kasterlee Formation. Pellets occur very regularly as fragmented or broken pieces. Rims are sometimes filled with clay precipitates as indicated by the arrow.

The relation in terms of size distribution of glauconite pellets to the remainder of the sediments reveals important information regarding possible mutual transport (Figure 4). For the formations of Diest and Kasterlee, and the Edegem and Kiel Members of the Berchem Formation, both distributions are very similar, which confirms simultaneous transport of glauconites and detrital particles. In contrast, the Poederlee Formation and the Antwerp sands of the Berchem Formation contain potential authigenic glauconites. Their glauconite pellet distribution is differently shaped from the remaining fraction of the sediment and the glauconite pellets are significantly larger than the remainder of the sediments (Figure 4). A reasonable conclusion is that the Neogene sediments in Belgium contain transported glauconites as well as possible authigenic glauconite horizons. These sediments are ideal, therefore, to test the presence of clay-sized glauconite and investigate the possible relation between glauconite pellets and the associated clay fraction.

DISINTEGRATION EXPERIMENTS ON GLAUCONITE PELLETS

Clay-sized glauconite might be artificially introduced into clay fractions during sampling or laboratory-preparation procedures. In order to verify such artificial contributions, the effects of different preparation processes were evaluated experimentally.

A first experiment was set up to investigate the effect of commonly applied geological lab procedures such as washing, shaking, stirring, wet sieving, and oven drying. This type of preparation procedure caused minimal disintegration of glauconites as contaminants were either absent or undetectable. Nevertheless, sample suspensions which were subjected to high-speed shaking for >24 h demonstrated a slightly greener coloration, illustrating that glauconite pellets broke up during this last procedure.

In a second experiment, purified >32 μm glauconite pellets of Neogene deposits were subjected to the standard clay preparation treatment for aggregate removal (modified after Jackson, 1975). The >32 μm glauconite pellets were separated paramagnetically from a washed and sieved sand sample and subjected to heating in a Na-acetate-buffer solution, H_2O_2, and Na-dithionite in a Na-citrate+$NaHCO_3$-solution (modified after Jackson, 1975; Zeelmaekers, 2011). The amount of disintegrated <2 μm pellets was determined quantitatively by weight. Based on 12 samples, the amount of clay produced from decomposed pellets averaged between 15 and 25 wt.%. Although this experiment was on purified glauconite pellets, it showed clearly that significant errors can be induced when glauconite pellets are not removed before standardized clay-preparation procedures.

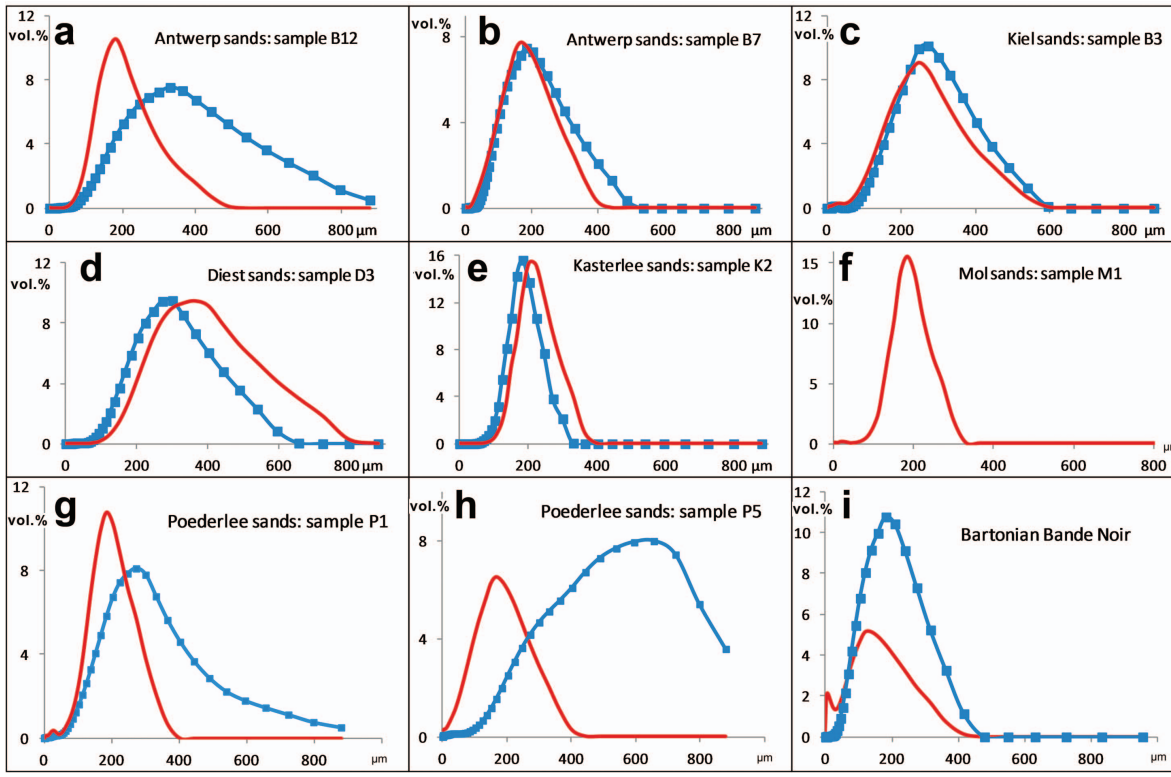

Figure 4. Comparison of the particle-size distribution between the >32 µm glauconite fraction (dotted blue) and the rest (red). The Poederlee (g,h) and Antwerp sands (a,b) typically contain large glauconite pellets with a particular size distribution, suggesting potential authigenic glauconitization. The pellet size is less well sorted than might be expected for authigenic minerals, *e.g.* the Bartonian Bande Noir horizon (I) (Odin, 1982; Maréchal, 1994). Some samples of the Antwerp and Poederlee sand (b, g) have similar particle-size distributions for quartz and glauconite, suggesting a common transport history.

A third experiment was set up to study contamination by glauconite particles in the 2–32 µm size fraction. Untreated samples were split into two parts and soaked in water. The first part was centrifuged to remove the <2 µm size fraction without any treatment, then the amounts of glauconite in the <2 µm and >2 µm size fractions were determined. To the second split, the standard clay treatments were applied (see second experiment). The <2 µm and >2 µm size fractions were then separated by centrifugation and the amount of glauconite was determined in both.

Two main observations can be made from this experiment. Firstly, large amounts of glauconite occurred in the <2 µm size fraction of untreated samples (Figure 5). Secondly, the increase in artificially produced <2 µm glauconite particles after treatment was limited to 15–20 wt.% (Figure 5). Nevertheless, this must be a maximum value because, due to the applied treatment, some clay aggregates also shifted to the <2 µm size fraction.

During a fourth experiment, a fresh clay outcrop sample of the Bartonian Bande Noir horizon (Maréchal, 1994) containing large amounts of glauconite pellets was subjected to several destructive actions such as shovel cutting, pushing, and shearing. The clay suspension immediately adopted a much greener color compared with the untreated sample. The <2 µm clay fraction was centrifuged before and after the destructive actions and analyzed using bulk XRD methods. The results indicated that, while the clay fraction of the untreated sample contained 20 wt.% glauconite, the treated sample had 30 wt.% glauconite in its clay fraction.

Consequently, the application of routine laboratory procedures affects glauconite particles in these sediments to such a degree that clay-sized glauconite is formed. However, these introductory experiments demonstrated that large amounts of <2 µm glauconite particles occur naturally in the clay fraction. After laboratory treatments, the amount of clay-sized glauconite increased to 20% at most, indicating that the majority of clay-sized glauconite occurs naturally.

SAMPLES AND METHODS

A selection of samples from the formations of Berchem, Diest, Kasterlee, Poederlee, and Mol were studied for glauconite pellet mineralogy and associated clay mineralogy. Samples were collected in various available cores and outcrops (Table 2, Figure 1).

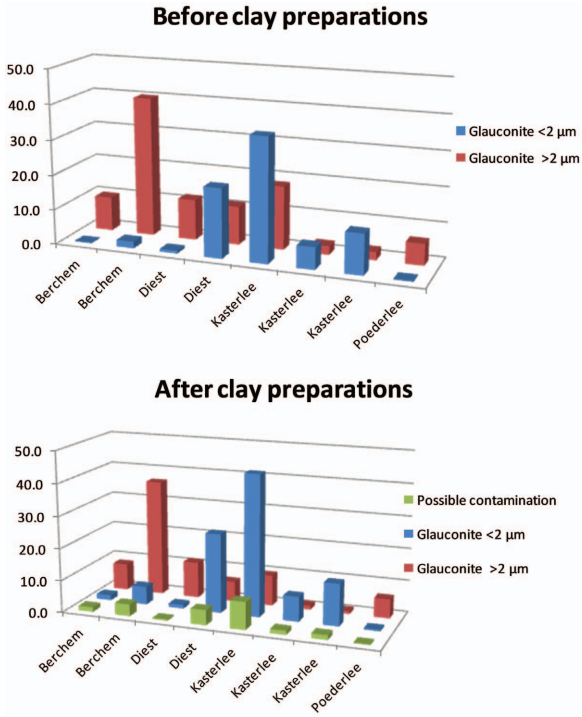

Figure 5. Results of the glauconite pellet disintegration experiment. Untreated samples were centrifuged with a Thermo Scientific SL40R benchtop centrifuge (relative centrifugal force $25214 \times g$ –Thermo Fisher Scientific, Erembodegem, Belgium) to <2 µm to quantify the amount of glauconite minerals present in the finer and coarser size fractions. This procedure was repeated after applying the standard clay-preparation procedures. The columns in green correspond to the maximum possible amount of contamination of >2 µm glauconite material that ended up in the <2 µm clay fraction.

Considering the importance of glauconite pellet disintegration behavior as demonstrated in the section above, the >32 µm glauconite pellets were separated systematically from the remainder of the sediment. Sand samples were soaked in demineralized water, stirred, and separated by 32 µm wet sieving, which was repeated three times. Glauconite pellets were isolated from the >32 µm fraction using a Frantz isodynamic magnetic separator. Clay samples were not treated because they contained no glauconite pellets. Both clay samples and <32 µm fractions of sand samples were examined for bulk mineralogy as well as for clay mineralogy on clay slides. Bulk measurements were recorded with XRD from randomly oriented powders which were fine-milled and mixed with an internal standard (after Środoń *et al.*, 2001). Oriented clay slides were prepared after the removal of all aggregate-forming particles (modified after Jackson, 1975; Zeelmaekers, 2011), followed by centrifugation of the <2 µm fraction. The clay material was subsequently Ca-saturated to ensure homogenous swelling of smectitic components (Eberl *et al.*, 1987; Sakharov *et al.*, 1999), and oven-dried afterward at 60ºC. Clay (<2 µm) material was also analyzed as randomly oriented powders by XRD, analogous to the procedure applied for bulk samples (after Środoń *et al.*, 2001).

Glauconite pellets were examined for mineralogy by XRD as randomly oriented powders but also as oriented slides after fine milling and subsequent Ca saturation. The major-element chemistry of glauconite pellets was characterized using inductively coupled plasma-optical emission spectroscopy (ICP-OES) while ferrous iron was determined through titration (after Wilson, 1955).

All XRD measurements were carried out at the department of Earth and Environmental Sciences at the University of Leuven on a Phillips PW1830 with CuKα radiation at 30 mA and 45 kV using a graphite monochromator and a scintillation detector. Diffractometer scans were recorded in Bragg-Brentano geometry from 5 to 65º for bulk measurements and from 2 to 47º for clay measurements, each time with a step size of 0.02º and 2 s counting time per step. Oriented slides were measured under air-dry, glycolated, and heated (550ºC) conditions.

Quantification of the <2 µm clay fraction was done in two independent ways. Firstly, clay modeling using the software *Sybilla* (©Chevron ETC) was used for interpretation, clay-structure analysis, and quantification. Secondly, quantification of randomly oriented powders and characterization of the 060 area was performed using the software *Quanta* (©Chevron ETC). This full-pattern fitting software bases the clay mineral quantification on the integrated intensity of the 060 area. The efficiency and accuracy of this method was described previously (Środoń *et al.*, 2001; Kleeberg, 2005; Omotoso *et al.*, 2006). Furthermore, the method takes advantage of the fact that clay mineral species with different 060 spacings can be quantified separately, which makes it ideally suited for independent glauconite quantification in the presence of the more common Al-rich clay mineral species.

RESULTS

Glauconite pellets

An inventory of mineralogical characteristics and chemical compositions of the glauconite-pellet bearing horizons in the Upper-Cretaceous and Cenozoic in Belgium was reported by Adriaens (2009). Cretaceous glauconite-bearing horizons were characterized by a 1*M* to 1*Md*-glauconite-smectite R1 phase with expandable layers ranging between 6 and 8%. Throughout the Cenozoic record, glauconite pellet mineralogy displays low variability, consisting of one or two 1*Md*-glauconite-smectite R1 phases with <16% expandable layers in total. Neogene glauconite pellets, from similar stratigraphic horizons to those used in the present study, typically contain between 6 and 12% expandable layers. The position of the 060 reflection of these glauconite pellets varied between 1.515 Å and 1.519 Å. Major-element analysis by ICP-OES revealed K_2O contents

Table 2. Overview of samples with information regarding stratigraphy, origin, and lithology. Borehole and outcrop locations are shown in Figure 1.

Name	Formation	Member	Location	Lithology	State
B1	Berchem	Edegem	Kruibeke claypit outcrop	Sand	Fresh
B2	Berchem	Kiel	Schilde borehole 66.3 m	Sand	Fresh
B3	Berchem	Kiel	Schilde borehole 67.3 m	Sand	Fresh
B4	Berchem	Kiel	Antwerp outcrop	Sand	Fresh
B5	Berchem	Kiel	Schilde borehole 64.8 m	Sand	Fresh
B6	Berchem	Antwerp	Herentals borehole 75.5 m	Sand	Fresh
B7	Berchem	Antwerp	Herentals borehole 85.5 m	Sand	Fresh
B8	Berchem	Antwerp	Dessel 5 borehole 165.5 m	Clay	Fresh
B9	Berchem	Antwerp	Dessel 5 borehole 165.9 m	Clay	Fresh
B10	Berchem	Antwerp	Essen borehole 176.9 m	Sand	Fresh
B11	Berchem	Antwerp	Mol borehole 143.7 m	Sand	Fresh
B12	Berchem	Antwerp	Essen borehole 180.5 m	Sand	Fresh
B13	Berchem	Antwerp	Schilde borehole 62.8 m	Sand	Fresh
D1	Diest (Campine)		Essen borehole 172.5 m	Sand	Fresh
D2	Diest (Campine)		Essen borehole 174.6 m	Sand	Fresh
D3	Diest (Campine)		Essen borehole 175.9 m	Sand	Fresh
D4	Diest (Campine)		Retie 1 borehole 48.86 m	Sand	Slightly oxidized
D5	Diest (Campine)		Dessel 2 borehole 47.50 m	Sand	Slightly oxidized
D6	Diest (Campine)		Dessel 2 borehole 34.65 m	Clay	Fresh
D7	Diest (Hageland)		Leuven GHB outcrop	Sand	Slightly oxidized
D8	Diest (Hageland)		Linden outcrop	Sand	Slightly oxidized
D9	Diest (Hageland)		Leuven Kesselberg outcrop	Sand	Slightly oxidized
D10	Diest (Hageland)		Leuven GHB outcrop	Sand	Slightly oxidized
D11	Diest (Hageland)		Leuven GHB outcrop	Clay	Fresh
D12	Diest (Hageland)		Leuven GHB outcrop	Clay	Fresh
K1	Kasterlee		Dessel 3 borehole 28.58 m	Sand	Fresh
K2	Kasterlee		Dessel 3 borehole 29.78 m	Sand	Fresh
K3	Kasterlee		Dessel 2 borehole 32.03 m	Sand	Fresh
K4	Kasterlee		Lichtaart outcrop	Sand	Fresh
K5	Kasterlee		Lichtaart outcrop	Sand	Fresh
K6	Kasterlee		Dessel 3 borehole 30.73 m	Clay	Fresh
K7	Kasterlee		Dessel 2 borehole 32.75 m	Clay	Fresh
M1	Mol		Dessel 3 borehole 12.10 m	Sand	Fresh
M2	Mol		Dessel 3 borehole 12.75 m	Sand	Fresh
M3	Mol		Dessel 3 borehole 13.10 m	Sand	Fresh
M4	Mol		Dessel 2 borehole 16.5 m	Sand	Fresh
M5	Mol		Dessel 2 borehole 19.2 m	Sand	Fresh
P1	Poederlee		Rees borehole 21.20 m	Sand	Fresh
P2	Poederlee		Rees borehole 21.55 m	Sand	Fresh
P3	Poederlee		Rees borehole 21.90 m	Sand	Fresh
P4	Poederlee		Rees borehole 22.40 m	Sand	Fresh
P5	Poederlee		Rees borehole 23.80 m	Sand	Fresh
P6	Poederlee		Rees borehole 24.20 m	Sand	Fresh

ranging from 5.5 to 7 wt.%, pointing to well evolved pelletal maturity (Table 3). Total (Fe_2O_3+FeO) contents for Neogene glauconite pellets ranged between 16 and 23.5 wt.% oxides (Table 3), with a typical ferric:ferrous ratio of 9:1, plotting within the glauconite compositional field of Meunier and El Albani (2007) (Figure 6).

The results of the clay modeling of oriented slides (Figure 7) show that the majority of analyzed glauconite pellets consisted of two separate phases: a glauconite-smectite R1 phase with 5−10% expandable layers and a three-component glauconite-expandable R1 phase with a total of 25–35% expandable layers of two types. The expandable minerals in the former phase are smectites of the low-charge type while in the three-component system they consist of both low-charge and high-charge smectite with a 60:40−70:30 ratio, respectively. Traces of kaolinite were often encountered as the result of clay precipitation in the pelletal rims (Figure 3). The glauconite pellets of the different investigated formations were characterized based on the relative amounts of both glauconite-expandable phases and their typical 060 value (Figure 7 and Table 4). Furthermore, during modeling, the octahedral Fe content of the glauconite pellets was assessed. This parameter shows low variability for all glauconite pellets investigated, ranging from 0.75 to 0.9/half unit cell.

Glauconite pellets of the Berchem Formation typically display a 75:25 ratio between the less expandable two-component and more expandable three-component glauconite-smectite phase, respectively. No distinction was found between glauconite pellets of the Antwerp sand and the Kiel and Edegem sands. Glauconite pellets of both the Diest and Kasterlee Formations generally have a small amount of expandable layers, which was reflected in their 90:10 less expandable-more expandable ratio. Glauconite pellets of the Poederlee sands contained two R1 glauconite-smectite phases but also Fe-rich smectite was also present (Figure 7), which is unique in the Campine basin (Adriaens, 2009). The estuarine Mol Formation contained no glauconite pellets and was, therefore, not characterized further.

Clay mineralogy of the <2 μm fraction

Sands. The quantitative mineralogical composition of the <2 μm clay fractions from the sands, as determined by clay modeling (Figure 8), illustrates the systematic presence of clay-sized glauconite-smectite, which was defined by its unique 060 value and modeled octahedral Fe content (Figure 9, Table 4). Optimal modeling results were only obtained after introducing similar glauconite-smectite R1 phases which make up the mineralogy of the associated sand-sized glauconite pellets. The clay mineralogy of the Berchem Formation was always rich in discrete dioctahedral smectite and Al-rich mixed-layer illite-smectite. Clay-sized glauconite was quantified in total amounts ranging from 10% up to 30% with typically the more expandable type (three-component glauconite-smectite R1 with 22–30% expandable layers) dominating the less expandable type (glauconite-smectite R1 with 8−12% expandable layers) (Table 4 and Figure 8). Clay minerals in the Antwerp Member were not significantly different from those in the Edegem and Kiel Members. Sample B11, however, contained almost no clay-sized glauconite. In the Diest sands, the <2 μm clay mineralogy depended on the origin of the samples. Samples from the Hageland area contained large amounts of clay-sized glauconite, up to 90% of the total <2 μm fraction, with smaller amounts of Al-rich illite-smectite, illite, kaolinite, and, occasionally some chlorite. Diest sand samples originating from the Campine area, contained smaller amounts of clay-sized glauconite with values between 20 and 45%. Contributions from other clay minerals were, therefore, more important, in particular of discrete smectite, which is seldom found in sands in the Hageland area. Very similar more and less expandable clay-sized glauconite types as for the Berchem sands were used during modeling. In the Hageland area the less expandable type predominates, whereas in samples of the Campine area the ratio of more expandable type:less expandable type was just 2:1 (Table 4).

The Kasterlee sands contained variable amounts of clay-sized glauconite, ranging from 20 to 50%, with the less expandable clay-sized glauconite type generally dominating the more expandable type. While the kaolinite content in the Berchem and Diest sands was rather small (<10%), it was much greater in the Kasterlee sands with values between 15 and 35%.

Clay-sized glauconite also exists naturally in the Poederlee sands, but in limited amounts (<15%). Both the less and more expandable glauconite types were used in these clay patterns. Smectite was, however, the dominant clay mineral consisting of dioctahedral as well as trioctahedral expandable phases. The dioctahedral smectite is comparable in all formations discussed and appears to be very poor in Fe content, with the modeled octahedral Fe content <0.25/half unit cell. The trioctahedral expandable species was, however, very rich in Fe with 1.5 octahedral Fe/half unit cell.

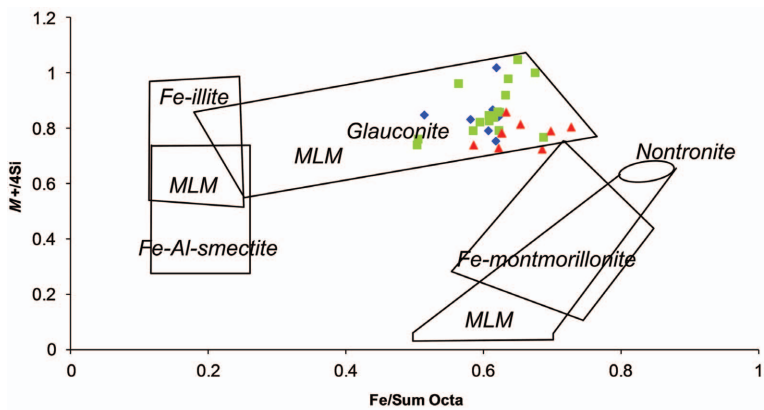

Figure 6. Position of the Belgian Cenozoic glauconite pellets (see Table 2 for sample information) in a compositional diagram. End-member positions are indicated by squares. MLM indicates mixed-layer minerals, *M*+ corresponds to the interlayer charge, while 'Sum octa' corresponds to the sum of octahedral cations in the structure. Blue dots refer to poorly expandable glauconite pellets (K_2O <7%), red triangles to pellets which are more expandable (K_2O >10%), and green squares to a group of glauconite pellets which expand to a medium extent (7%<K_2O<10%). Neogene glauconite pellets as presented here belong to the blue and green markers (modified after Meunier and El Albani, 2007).

Table 3. Bulk chemical data (%) of Neogene glauconite pellets, analyzed using ICP-OES.

Chronostratigraphy		Chemical phase / Lithostratigraphy	SiO_2 0.01	Al_2O_3 0.01	Fe_2O_3 0.01	FeO 0.01	MgO 0.01	CaO 0.01	Na_2O 0.01	K_2O 0.01	MnO 0.001	TiO_2 0.001	P_2O_5 0.01
Neogene	Zanclean	Luchtbal sand	43.990	9.940	19.103	1.660	3.010	0.361	0.130	6.340	0.047	0.856	0.190
		Kattendijk sand	44.250	9.860	20.292	1.480	3.030	1.098	0.140	6.450	0.019	0.346	0.200
	Messinian	Kasterlee sand	44.080	12.810	15.631	1.480	2.450	0.403	0.140	5.520	0.015	0.492	0.120
		Kasterlee sand	49.150	10.200	21.570	1.300	2.950	0.479	0.140	6.260	0.012	0.317	0.100
	Tortonian	Diest sand	45.110	10.690	18.620	2.740	2.790	0.397	0.100	6.190	0.019	0.500	0.170
		Diest sand	46.890	9.490	19.770	2.210	3.120	0.386	0.130	6.950	0.007	0.161	0.110
		Diest sand	46.230	10.510	19.920	2.560	3.050	0.413	0.090	6.960	0.009	0.214	0.120
		Deurne sand	46.850	9.770	20.280	1.840	3.370	0.500	0.110	6.720	0.016	0.127	0.260
		Deurne sandstone	45.810	9.870	14.580	2.370	3.420	0.242	0.140	6.230	0.018	0.225	0.320
	Langhian	Zonderschot sands	45.440	8.670	20.270	3.270	3.190	1.317	0.210	6.400	0.021	0.288	0.170
		Antwerp sands	50.340	12.560	18.590	3.090	3.350	1.634	0.220	6.430	0.027	0.538	0.150
		Antwerp sands	44.110	9.510	18.800	2.730	3.050	0.847	0.150	6.320	0.012	0.174	1.270
		Antwerp sands	46.055	10.220	19.670	2.550	3.160	0.497	0.290	6.500	0.014	0.225	0.300
	Burdigalian	Kiel sands	45.160	9.680	13.550	2.550	3.170	2.548	0.200	6.090	0.010	0.164	0.070
		Kiel sands	47.350	9.990	20.370	2.200	3.070	0.370	0.130	6.550	0.010	0.218	0.260
		Kiel sands	45.580	9.840	18.270	2.190	3.020	3.290	0.130	5.960	0.011	0.217	0.260
		Kiel sands	46.983	9.580	17.710	3.090	3.450	0.300	0.130	6.600	0.009	0.147	0.160
Paleogene	Rupelian	Eigenbilzen sands	46.190	9.760	20.810	1.660	3.080	0.481	0.110	6.120	0.058	0.000	0.450
	Bartonian	base Asse-Ursel	43.040	6.650	14.030	3.480	2.450	0.485	0.190	5.850	0.011	0.146	0.050
		base Asse-Ursel	43.060	8.770	16.300	3.270	2.740	0.415	0.220	6.130	0.011	0.150	0.050
		Bande Noir	45.160	8.890	21.970	1.300	3.540	0.531	0.110	6.160	0.045	0.407	0.060
		Bande Noir	38.880	5.440	8.350	1.310	3.180	0.684	0.210	5.560	0.018	0.241	0.020
		Wemmel sands	42.300	8.070	19.530	1.840	3.700	1.451	0.130	6.070	0.227	0.439	0.060
		Wemmel sands	43.058	8.860	21.020	2.560	3.660	0.040	0.130	5.860	0.092	0.000	0.050
	Lutetian	Lede sands	42.688	8.910	12.270	2.210	2.940	0.671	0.110	4.990	0.130	0.000	0.030
		Brussel sands (Gobertange)	47.720	8.530	19.230	1.660	4.300	0.438	0.140	6.850	0.014	0.116	0.070
		Brussel sands (Gobertange)	48.840	8.380	20.930	1.660	4.260	0.691	0.130	6.960	0.019	0.105	0.060
		Brussel sands (Gobertange)	46.020	8.250	11.683	1.490	4.010	0.438	0.100	6.490	0.019	0.120	0.040
		Aalter sands	49.420	8.860	21.430	1.480	3.670	0.657	0.140	5.650	0.051	0.787	0.140
	Ypresian	Vlierzele sands	47.460	8.520	21.180	1.120	3.490	0.718	0.160	5.850	0.026	0.259	0.070
		Vlierzele sands	44.110	9.410	11.757	0.760	2.670	0.626	0.140	4.570	0.027	0.188	0.110
		Vlierzele sands	49.530	9.510	19.907	1.120	3.020	0.775	0.180	5.620	0.021	0.209	0.050
		Vlierzele sands	49.690	7.860	21.112	1.130	3.130	1.281	0.180	5.950	0.026	0.158	0.060
		Bierbeek sands	44.570	12.440	15.250	2.200	2.830	1.076	0.230	3.710	0.081	2.171	0.110
		Egem sandstone	47.560	6.950	22.190	2.730	3.360	0.556	0.140	6.230	0.031	0.358	0.110
	Thanetian	Tuffeau de Lincent	47.270	7.320	20.150	0.760	3.290	0.846	0.110	6.230	0.137	0.201	0.110
Cretaceous	Campanian	Vaals sands	48.090	7.460	24.350	1.300	2.450	0.764	0.140	6.100	0.013	0.119	0.180
	Santonian	Chalky sandstone	49.400	7.400	19.220	2.560	3.980	0.760	0.310	8.140	0.007	0.063	0.420
	Coniacian	Craies de Maisières	46.840	9.450	16.570	1.480	3.770	0.068	0.190	7.400	0.006	0.073	2.150
	Turonian	Dièves marls	43.000	6.880	5.730	2.560	3.460	1.212	0.120	6.630	0.009	0.074	0.350

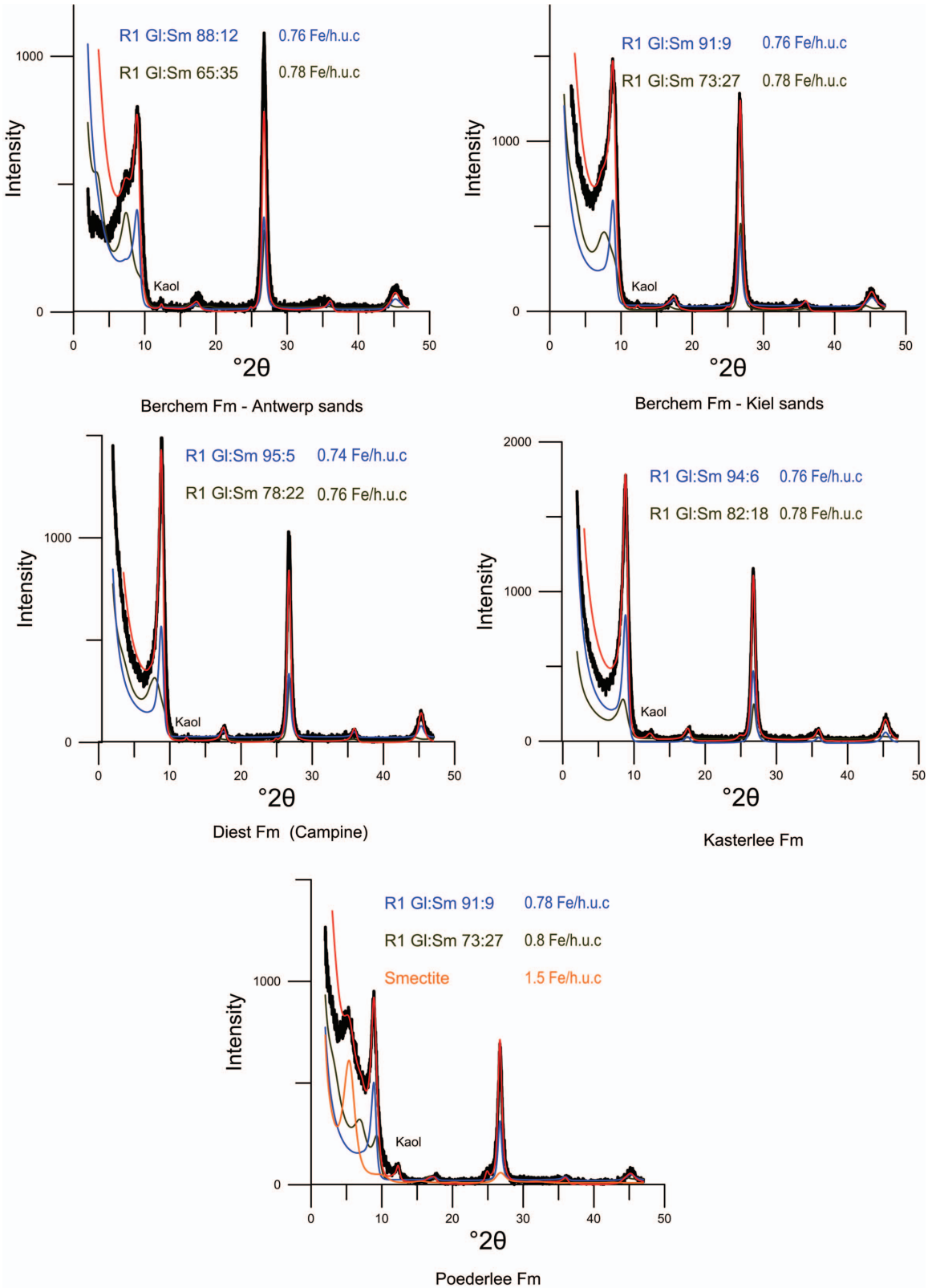

Figure 7. XRD traces of glauconite pellets glycolated (black) and the Sybilla-fitted model (red) . The glauconite-smectite R1 phases used in the clay modeling are shown in blue and green for each formation and are representative of all studied samples. 'Kaol' indicates small amounts of kaolinite.

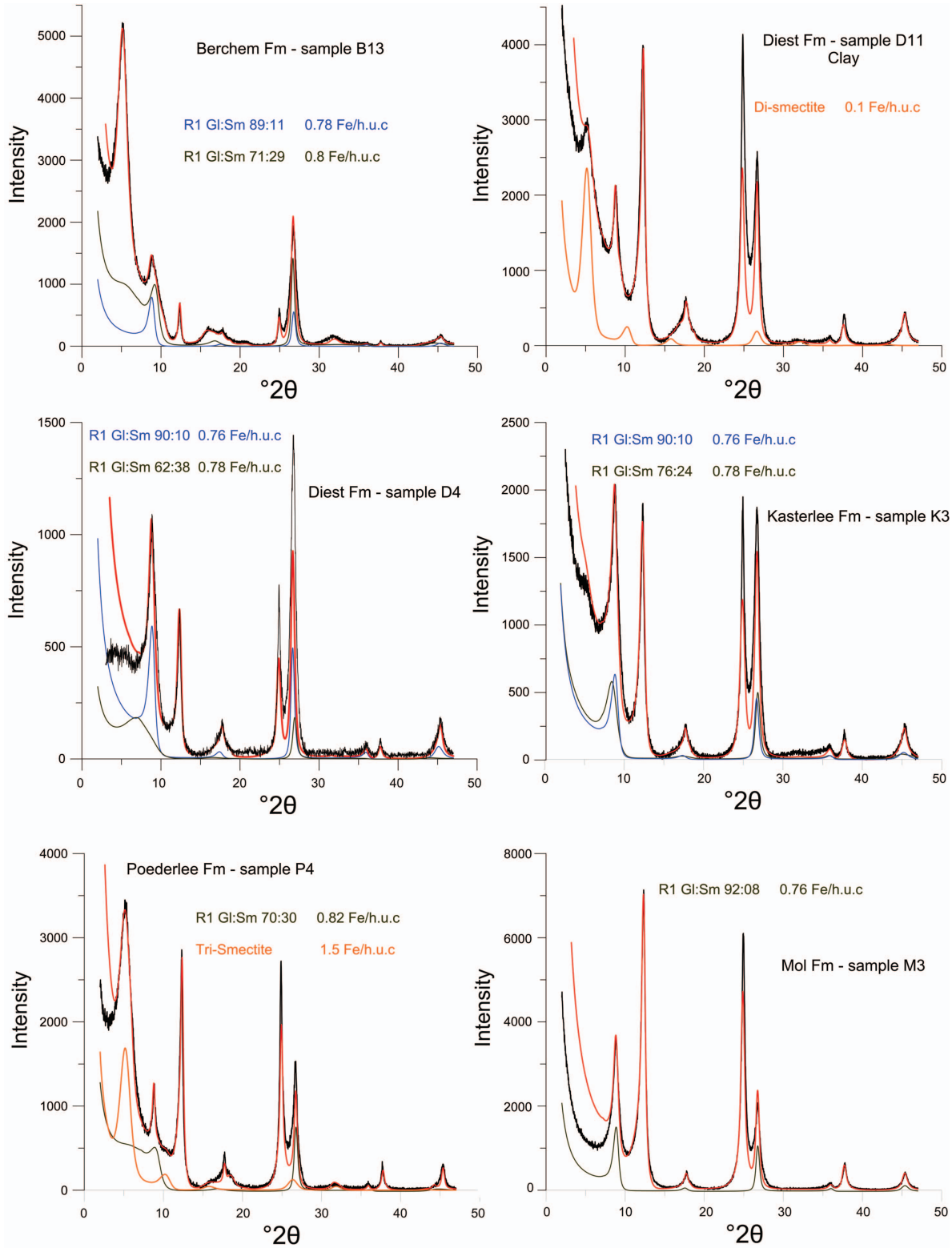

Figure 8. XRD traces of Ca-saturated clay fractions (<2 µm, glycolated, on oriented slides) (black). The Sybilla model fit is shown in red. The glauconite-smectite R1 phases used in the clay modeling are shown in blue and green for each formation.

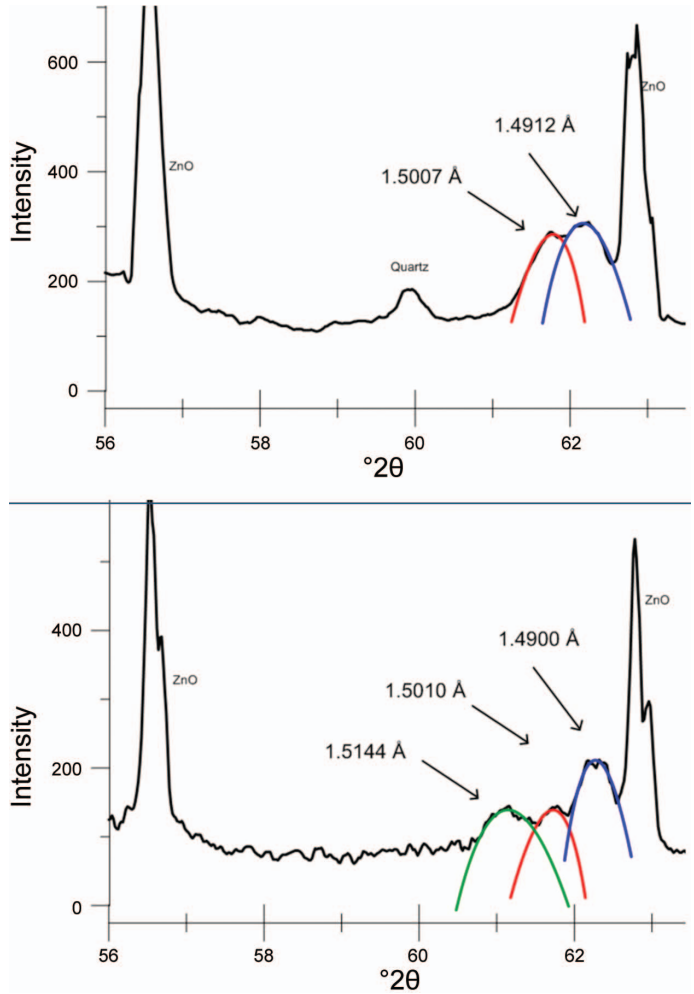

Figure 9. (upper) Decomposition of the 060 area of the clay samples; (lower) decomposition of the 060 area for sand samples. The blue curve represents the contribution from kaolinite; the red curve represents the contribution from all dioctahedral Al-clays (smectite, illite, illite-smectite) while the green curve corresponds to the contribution of glauconite and/or glauconite-smectite. XRD patterns were recorded with ZnO as the reference material.

Finally, the clay mineralogy of the estuarine Mol sands consisted mainly of kaolinite but also contained clay-sized glauconite in significant amounts. Note that these quartz-rich sands contained glauconite pellets only in their clay fraction; clay-sized glauconite represents an important proportion of the clay fraction. Only the less expandable clay-sized glauconite type was necessary to model the clay fractions of the Mol Formation

Clays. Sedimentary clay samples were examined in all lithological units. In contrast to the sand samples, the <2 μm clay fractions displayed brown to grey coloration. The XRD patterns of clays were similar to those of sand samples, and modeled clay mineral characteristics were identical to those in sands. Inspection of the d_{060} of randomly oriented powders, however, indicated that clay-sized glauconite was systematically absent from clays (Figure 9, Table 4). This was confirmed by the clay modeling because oriented clay patterns could not be modeled with the incorporation of Fe-rich clay minerals (Figure 8). The most important clay minerals in these size fractions were dioctahedral Al-smectite, Al-rich illite-smectite, kaolinite, and chlorite (Table 4).

DISCUSSION

Clay-sized glauconite was encountered systematically in Cenozoic marine glauconite pellet-bearing samples. Both the experiments and the data presented reveal that inappropriate use of laboratory treatments can cause glauconite pellet disintegration. However, after removing the >32 μm glauconite pellets, the amount of contaminated clay-sized glauconite was at most 25% and the real value is probably much less. Therefore, most of the clay-sized glauconite must have a natural origin. Its presence is confirmed in units that contain glauconite pellets which were probably less transported or even authigenic but also in units where

Table 4. Quantitative clay mineralogy of each analyzed sample. Glauconite contents are shown for sand samples together with d_{060} values of both pelletal and clay-sized glauconite. Question marks indicate that the exact 060 position could not be determined due to low glauconite abundance in the particular sample.

Sample	Formation	Glauconite grains 060 (Å)	Glauconite clay 060 (Å)	% Glauconite grains in the >32 μm fraction	Kaolinite	Illite	Mixed layer illite-smectite	Clay-sized glauconite (less expandable)	Clay-sized glauconite (more expandable)	Di-smectite	Tri-smectite	Chlorite
B1	Berchem	1.5139	1.5144	40	4	8	22	3	13	50	0	1
B2	Berchem	1.5139	1.5139	32	5	14	13	2	13	51	0	1
B3	Berchem	1.5144	1.5139	29	2	4	29	3	7	55	0	1
B4	Berchem	1.5148	1.5135	34	4	4	36	7	11	37	0	1
B5	Berchem	1.5148	1.5144	36	1	5	32	3	14	44	0	1
B6	Berchem	1.5139	1.5131	39	5	5	17	1	18	54	0	1
B7	Berchem	1.5128	1.5153	43	1	7	26	10	13	42	0	1
B8	Berchem				10	14	48	0	0	27	0	1
B9	Berchem				10	13	48	0	0	29	0	1
B10	Berchem	1.5139	1.5135	35	3	3	38	6	15	35	0	1
B11	Berchem	1.5144	1.5131	43	5	5	33	0	2	54	0	1
B12	Berchem	1.5148	1.5144	48	7	17	33	4	10	28	0	1
B13	Berchem	1.5139	?	55	1	5	34	5	12	42	0	1
				0			0					
D1	Diest	1.5153	1.5157	20	6	17	25	27	17	7	0	1
D2	Diest	1.5148	1.5162	27	5	10	30	32	13	9	0	1
D3	Diest	1.5148	1.5157	20	5	10	27	34	15	7	0	2
D4	Diest	1.5162	1.5171	19	15	18	26	30	8	2	0	1
D5	Diest	1.5180	1.5175	38	5	4	33	4	18	15	21	0
D6	Diest				28	14	26	0	0	31	0	1
D7	Diest	1.5189	1.5189	31	2	3	5	90	0	0	0	0
D8	Diest	1.518	1.5189	32	1	6	10	84	0	0	0	0
D9	Diest	1.518	1.518	36	2	2	22	72	0	1	0	1
D10	Diest	1.5189	1.5184	35	1	0	3	96	0	0	0	0
D11	Diest				19	18	29	0	0	34	0	1
D12	Diest				21	12	35	0	0	31	0	1
				0			0					
K1	Kasterlee	1.5166	1.5162	6	18	4	16	51	10	0	0	1
K2	Kasterlee	1.5166	1.5166	6	24	5	44	17	5	4	0	1
K3	Kasterlee	1.5171	1.518	5	25	10	17	34	9	4	0	1
K4	Kasterlee	1.5162	1.5166	5	20	8	19	20	26	6	0	1
K5	Kasterlee	1.5166	1.5171	5	18	6	19	28	23	5	0	1
K6	Kasterlee				34	19	39	0	0	7	0	1
K7	Kasterlee				30	15	42	0	0	12	0	1
				0								
M1	Mol		1.5135	0	45	7	14	34	0	0	0	0
M2	Mol		1.5144	0	48	8	13	31	0	0	0	0
M3	Mol		1.5148	0	49	8	12	31	0	0	0	0
M4	Mol		1.5139	0	48	12	10	30	0	0	0	0
M5	Mol		1.5135	0	47	11	12	30	0	0	0	0
P1	Poederlee	1.5222	1.5238	20	14	15	18	4	12	18	17	2
P2	Poederlee	1.5211	1.522	24	16	18	16	5	9	15	19	2
P3	Poederlee	1.522	?	22	16	17	22	2	4	20	17	2
P4	Poederlee	1.5211	?	21	17	14	21	2	2	28	16	0
P5	Poederlee	1.5202	?	24	11	6	16	0	0	32	33	2
P6	Poederlee	1.5202	?	22	9	5	12	0	3	38	33	1

glauconites were transported in the same way as the detrital quartz (Figure 4). Furthermore, the occurrence of the glauconite pellets is not restricted to marine glauconite pellet-bearing units because the estuarine Mol Formation also contains clay-sized glauconite.

The relation between clay-sized glauconite and pelletal glauconite

The occurrence of clay-sized glauconite was reported by Baioumy and Boulis (2012) who suggested a pre-pelletal stage in the glauconitization process. The occurrence of fine-grained glauconite is indeed expected in areas where new glauconite pellets are being formed (Odin, 1982). Clay-sized glauconite is, however, rarely reported coexisting with sand-sized glauconite pellets. If reported, the clay fraction of early-stage or more evolved glauconitic sediments typically consists of Al-rich clay minerals (Bell and Goodell, 1967; Seed, 1968; Baldermann *et al.*, 2012) and rarely of Fe-rich clays.

In the current case, however, the results illustrate glauconite occurrence in sand and clay fractions, which both display a very similar two-phase glauconite-smectite R1 mineralogy (Table 4). The near-linear relation between d_{060} values of glauconite pellets and clay-sized glauconite in the same sample (Figure 10) demonstrates the close association between both glauconite types. Furthermore, d_{060} values can be used as a parameter to distinguish the different analyzed formations (Figure 10), which supports the idea that both sand-sized and clay-sized glauconite occurrences are closely related. While during clay modeling an identical glauconite-smectite R1 structure was used to model both the clay-sized and the pelletal glauconite, the respective d_{060} values are not always identical (Figure 10). However, compositional differences exist between the outer and inner surfaces of glauconite pellets, as well as between larger and smaller glauconite pellets (Harris *et al.*, 2007), which could explain such small-scale mineralogical differences Nevertheless, the interpretation is, then, that both glauconite types indeed belong to the same system but occur in different sizes.

The origin of clay-sized glauconite in marine deposits

When assuming that both glauconite types are part of the same system, this must mean that either pellet disaggregation or pelletization of clay-sized glauconite is the controlling process. An alternative hypothesis is that both types were formed simultaneously.

El Albani (2005) and Banerjee *et al.* (2012) demonstrated that glauconite authigenesis results in distinct mineralogical and crystal-chemical differences between different glauconite types, which is clearly not observed in the present setting

Furthermore, if the clay-sized glauconite is an authigenic precipitate, this should be reflected in its properties as the process of glauconitization depends on the amount of available Fe and, thus, the prevailing redox conditions (Odin, 1982; Chamley, 1989). El Albani (2005) demonstrated that open marine conditions yield the anoxic conditions necessary for Fe mobility through organic matter resulting in a large amount of Fe and K uptake in the glauconite structure. Near-coastal or estuarine environments are, on the contrary, influenced

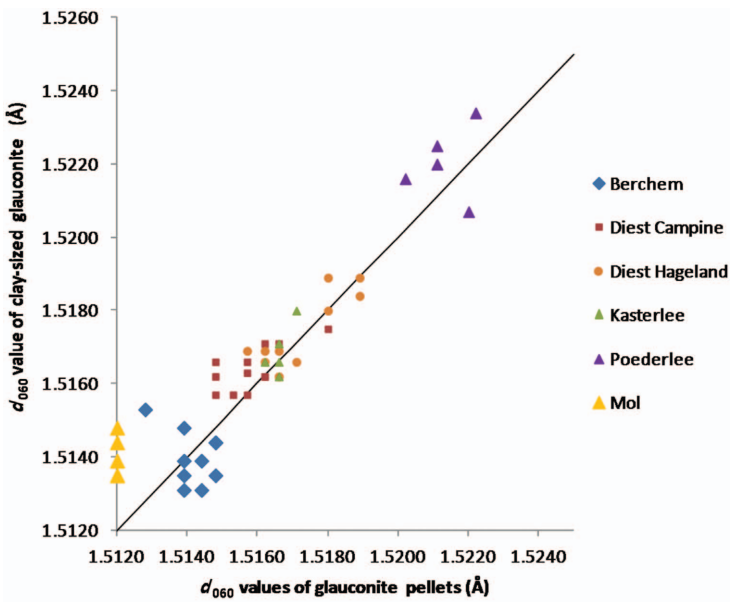

Figure 10. Glauconite pellet d_{060} values plotted against clay-sized glauconite d_{060} values, following a 1:1 relation. The d_{060} value is apparently a good parameter to distinguish between different formations. The yellow line indicates the position of the clay-sized glauconite of the Mol formation.

by oxic freshwaters which will strongly reduce the amount of available Fe and result in Al-rich glauconites with d_{060} spacings of between 1.50 Å and 1.51 Å (Parry and Reeves, 1966; Porrenga, 1968; Berg-Madsen, 1983; El Albani *et al.*, 2005). Louwye (2005) and Louwye *et al.* (2006) found evidence for near-coastal depositional environments with continental influences in the Kasterlee and Poederlee Formations, while the Berchem and Diest Formations were exposed to fully marine conditions. The quartz sands of the Mol Formation were deposited in estuarine conditions (Vandenberghe *et al.*, 1998). The mineralogy and crystal chemistry of the clay-sized glauconite found in these units (Table 4) revealed little correspondence with a sedimentary environment, as the Fe contents are almost equal in each of the formations described. Although anoxic conditions may also develop in near coastal environments (Gertsch *et al.*, 2010; Wignall and Newton, 2001), this involves large amounts of organic material and is not found in the current deposits.

Baioumy and Boulis (2012) suggested that clay-sized glauconite can form pellets at a later stage due to reworking or circulation processes. This seems rather unlikely in the current situation because clay-sized and pelletal glauconite occur systematically together in the same system and, furthermore, are never present in intercalated clay layers. Moreover, based on d_{060} values and, thus, Fe-contents and K_2O-values of the glauconite pellets (Table 3), both types of glauconite represent well evolved glauconitization stages which contradicts an early-stage origin. Considering that the bulk of pelletal glauconites was actively transported (Figure 4), and that both pelletal and clay-sized glauconite are probably part of the same system, a true authigenic nature of the clay-sized glauconite is, therefore, very unlikely.

The only stratigraphic occurrence where clay-sized glauconite has been reported coexisting with glauconite pellets are soils and weathering profiles (Van Ranst and De Coninck, 1983; Tedrow, 1986, 2002). In this case, the characteristics of both glauconite types are expected to be equal because clay-sized glauconite formation is related to weathering and soil processes (Velde and Meunier, 2008). In the current setting, however, soil environments are excluded. Considering the limited depth of burial and the fact that glauconite pellets are not deformed, compaction is also to be excluded. The origin of the clay-sized glauconite is probably related to the abrasion and breaking up of glauconite pellets during physical transport.

A key observation is that clay-sized glauconite is incorporated in the clay fraction of sands but never in the intercalated clay layers (Table 4, Figure 8). The type and relative proportions of clay minerals in both sands and clays are very similar, indicating that Al-smectite, Al-rich illite-smectite, illite-smectite, kaolinite, and chlorite mainly originate from a detrital source area. This clay assemblage probably constitutes the 'background' clay mineralogy in sands and clays but apparently does not include clay-sized glauconite. Furthermore, no linear relation exists between clay-sized glauconite and the detrital sedimentary clay fraction (Figure 11). As a result, a distant source area is excluded as the main source of clay-sized glauconite but points to a more local origin. A physically weaker population of incomplete or broken glauconite pellets of older deposits was probably abraded over short-range transport or decomposed on impact.

This process of abrasion of glauconite pellets into a clay-sized glauconite fraction is most logical in glauconite pellet-bearing sediments for which the glauconite pellets are apparently transported together with the detrital, mainly quartz, fraction (Figure 4). Although the Poederlee and Antwerp sands favor glauconite pellet authigenesis (Figure 4; see also Odin *et al.*, 1974), clay-sized glauconite is also present in these deposits, which seems to contradict a transported origin (Table 4). The heterogeneity in glauconite-pellet size distribution (Figure 4), however, suggests that a variety of depositional processes played an important role, indicating that glauconite pellets are not exclusively authigenic. Glauconite pellets in these units were, therefore, only transported over short distances as they were swept over the shelf during transgressive movement away from the area of glauconitization. This process is apparently sufficient to produce clay-sized glauconite but in smaller amounts than detrital glauconite pellets. Consequently, the amount of clay-sized glauconite can be used as a proxy for the amount and intensity of pelletal glauconite transport and the energy of the depositional environment. This is demonstrated by the small amounts of clay-

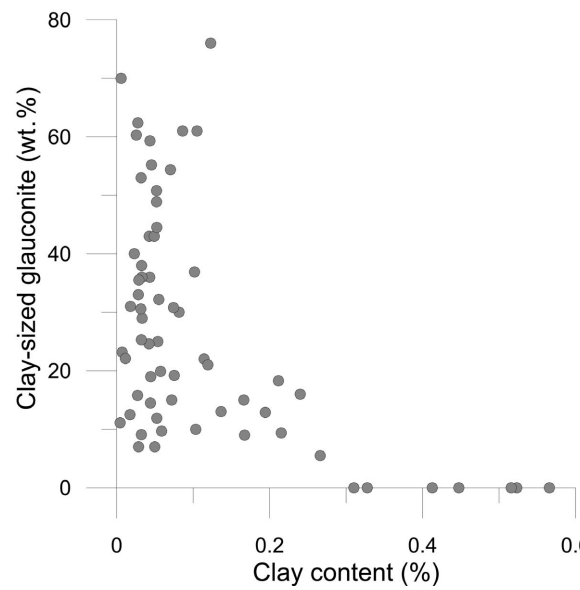

Figure 11. The <2 µm clay fraction plotted *vs.* the amount of <2 µm glauconite which shows no linear relation.

sized glauconite in the Poederlee sands, and, to a lesser degree, the Antwerp sands (Table 4).

The origin of clay-sized glauconite in the estuarine Mol Formation

The estuarine Mol sands are very mature sands with no glauconite pellets and the 30% clay-sized glauconite in its clay fraction (Table 4). The clay-sized glauconite in these sands cannot, therefore, be derived from pre-existing pelletal glauconite in the Mol Formation. The estuarine environment in which this deposit was formed does not yield the necessary reducing conditions for glauconitization which makes an authigenic origin unlikely. Estuarine glauconitization was reported by El Albani (2005) but the amount of Fe incorporated in those mineral structures was much less than the relatively large Fe contents found in the clay-sized glauconite of the Mol Formation. Nevertheless, clay-sized glauconite produced in slightly older deposits can be further taken up in subsequent erosion and sedimentation cycles together with clays from other sources. The clay-sized glauconite in the estuarine Mol Formation must, therefore, be reworked from the locally out-cropping glauconitic sands occurring in and around the estuary (Figures 2, 3). The d_{060} position of the Mol sands (Figure 10) is, however, slightly different from the older Kasterlee and Poederlee Formations, suggesting that Fe is lost from the clay-mineral structure during transport or as the result of acid percolation, leading to a slightly more Al-rich glauconite mineralogy.

Significance of expandable minerals

The abundance of expandable minerals in the clay fraction of the glauconitic sediments (Table 4) could indicate that it is the precursor of glauconite minerals as suggested by Buatier *et al.* (1989) and Jimenez-Millan *et al.* (1998). Clay modeling of the dioctahedral smectite, present in almost all the formations described, resulted in octahedral Fe contents of 0.05−0.25/half unit cell, common values for Al-rich dioctahedral smectites (Güven, 1988).

In the Poederlee Formation, however, a trioctahedral expandable phase is also present. Clay modeling resulted in an octahedral Fe content of ~1.5/half unit cell, which is significantly greater than the 0.75–0.9 octahedral Fe cations/half unit cell typical of glauconite pellets and clay-sized glauconite in these sediments. This Fe-rich expandable phase is also present in the glauconite pellets of the Poederlee Formation (Figure 7, Table 4), illustrating the mineralogical relation between glauconite pellets and the associated clay fraction. Furthermore, size distributions of the glauconite pellets (Figure 4) and the small amounts of clay-sized glauconite (Table 4) demonstrate that glauconitization took place at a nearby area or even partially at the current position. Nevertheless, the Fe-expandable phase in this particular deposit is probably the precursor mineral which induced pelletal glauconitization.

CONCLUSIONS

Experiments show that the large majority of clay-sized glauconite is naturally present in the samples. However, certain populations of glauconite particles tend to break up during strong physical actions of the sediment, excessive shaking at high speeds, and during standard clay preparations. This effect can be strongly reduced by isolating >32 μm glauconite particles prior to further clay mineralogical preparations. The data presented prove the existence of natural clay-sized glauconite in Neogene glauconite pellet-bearing and non-glauconite pellet-bearing sand deposits in the northern part of Belgium. The origin of clay-sized glauconite is not authigenic but related to glauconite pellet abrasion and disintegration upon transport. Intercalated sedimentary clay layers of the same deposits were never found to incorporate the clay-sized glauconite, meaning that the latter did not originate from distant detrital source areas but rather has a local origin within the same depositional basin. The amount of clay-sized glauconite produced is indicative of the distance and intensity of transport. The clay-sized glauconite in the estuarine Mol Formation was derived by erosion of older deposits around the estuary and reworked. A trioctahedral Fe-rich expandable phase was identified in both the clay fraction and the glauconite pellets of the Poederlee sands, suggesting that it acted as the precursor mineral for pelletal glauconitization. Clay-sized glauconite has never been reported as such before and is clearly an important contributor to the clay fraction in these deposits, emphasizing the energetic character of the environment in which they were formed.

REFERENCES

Adriaens, R. (2009) Mineralogical and crystal-chemical analysis of glauconites in the Upper-Cretaceous and Cenozoic strata of the Southern North Sea basin. Unpublished Masters thesis, University of Leuven, Leuven, Belgium, 105 pp.

Amorosi, A. (1995) Glaucony and sequence stratigraphy: a conceptual framework of distribution in siliciclastic sequences. *Journal of Sedimentary Research*, **65**, 419−425.

Amorosi, A. (1997) Detecting compositional, spatial, and temporal attributes of glaucony: a tool for provenance research. *Sedimentary Geology*, **109**, 135−153.

Bailey, S.W. (1980) Summary of recommendations of AIPEA nomenclature committee. *Clays and Clay Minerals*, **28**, 73−78.

Bailey, S.W. (1988) *Hydrous Phyllosilicates (exclusive of Micas)*. Reviews in Mineralogy, **19**, Mineralogical Society of America, Washington, D.C., 725 pp.

Baioumy, H. and Boulis, S. (2012) Non-pelletal glauconite from the Campanian Qusseir Formation, Egypt: Implication for glauconitisation. *Sedimentary Geology*, **249**, 1−9.

Baldermann, A., Grathoff, G.H., and Nickel, C. (2012) Micromileu-controlled glauconitisation in fecal pellets at Oker (Central Germany). *Clay Minerals*, **47**, 513−538.

Banerjee, S., Jeevankumar, S., and Eriksson, P.G. (2008) Mg-rich ferric illite in marine transgressive and highstand systems tracts: examples from the Paleoproterozoic Semri

Group, central India. *Precambrian Research*, **162**, 212–226.
Banerjee, S., Chattoraj, S.L., Saraswati, P.K., Dasgupta, S., and Sarkar, U. (2012) Substrate control on formation and maturation of glauconites in the Middle Eocene Harudi Formation, western Kutch, India. *Marine and Petroleum Geology*, **30**, 144–160.
Bell, D.H. and Goodell, H.G. (1967) A comparative study of glauconite and the associated clay fraction in modern marine sediments. *Sedimentology*, **9**, 169–202.
Berg-Madsen, V. (1983) High-alumina glaucony from the middle Cambrian of Öland and Bornholm, Southern Baltoscandia. *Journal of Sedimentary Petrology*, **53**, 875–893.
Buatier, M., Honnorez, J., and Ehret, G. (1989) Fe-smectite-glauconite transition in hydrothermal green clays from the Galapagos spreading center. *Clays and Clay Minerals*, **37**, 532–541.
Buckley, H.A., Bevan, J.C., Brown, K.M., Johnson, L.R., and Farmer, V.C. (1978) Glauconite and celadonite: two separate mineral species. *Mineralogical Magazine*, **42**, 373–382.
Chafetz, H.S. and Reid, A. (2000) Syndepositional, shallow water precipitation of glauconitic minerals. *Sedimentary Geology*, **136**, 29–42.
Chamley, H. (1989) *Clay Sedimentology*. Springer-Verlag, Berlin, 623 pp.
Cudzil, M.R. and Driese, S.G. (1987) Fluvial, tidal and storm sedimentation in the Chilhowee Group (Lower Cambrian), northeastern Tennessee, U.S.A. *Sedimentology*, **34**, 861–883.
De Meuter, F.J. and Laga, P. (1976) Lithostratigraphy and biostratigraphy based on benthonic foraminifera of the Neogene deposits of northern Belgium. *Bulletin de Société belge Géologie*, **85**, 133–152.
Derkowski, A., Środoń, J., Franus, J., Uhlík, P., Banaś, M., Zieliński, G., Čaplovičova, M., and Franus, M. (2009) Progressive dissolution of glauconite and its implications for the methodology of K-Ar and Rb-Sr dating. *Clays and Clay Minerals*, **57**, 531–554.
Eberl, D.D., Środoń, J., Lee, M., Nadeau, P.H., and Northrop, H.R. (1987) Sericite from the Silverton caldera, Colorado: Correlation among structure, composition, origin, and particle thickness. *American Mineralogist*, **72**, 914–934.
El Albani, A. (2005) Unusual occurrence of glauconite in a shallow lagoonal environment (Lower Cretaceous, northern Aquitaine Basin, SW France). *Terra Nova*, **17**, 537–544.
Gertsch, B., Adatte, T., Keller, G., Aziz, A.M., Tantawy, A., Berner, Z., Mort, H.P., and Fleitmann, D. (2010) Middle and late Cenomanian oceanic anoxic events in shallow and deeper shelf environments of western Morocco. *Sedimentology*, **57**, 1430–1462.
Gonzalez, R., Dias, J.M.A., Lobo, F., and Mendes, I. (2004) Sedimentological and paleoenvironmental characterization of transgressive sediments on the Guadiana Shelf (Northern Gulf of Cadiz, SW Iberia). *Quaternary International*, **120**, 133–144.
Güven, N. (1988) Smectites. Pp 497–559 in: *Hydrous Phyllosilicates*. Reviews in Mineralogy, **19**. Mineralogical Society of America, Washington DC.
Harris, W.B., Fullager, P.D., and Tovo, L.T. (2007) Significance of young Paleocene Rb-Sr glauconite dates from the Lang Syne Formation, Savannah River site, South Carolina. *Southeastern Geology*, **37**, 55–72.
Hesselbo, S.P. and Huggett, J.M. (2001) Glaucony in ocean-margin sequence stratigraphy (Oligocene–Pliocene, Offshore New Jersey, USA; ODP Leg 174A). *Journal of Sedimentary Research*, **71**, 598–606.
Ireland, B.J., Curtis, C.D., and Whiteman, J.A. (1983) Compositional variation within some glauconites and illites and implications for their stability and origins. *Sedimentology*, **30**, 769–786.
Jackson, M.L. (1975) *Soil Chemical Analysis – Advanced Course*, 2nd edition. Published by the author, Madison, Wisconsin, USA, 895 pp.
Jimenez-Millan, J., Molina, J.M., Nieto, F., Nieto, L., and Ruiz-Ortiz, P.A. (1998) Glauconite and phosphate peloids in Mesozoic carbonate sediments (Eastern Subbetic Zone, Betic Cordilleras, SE Spain). *Clay Minerals*, **33**, 547–559.
Kleeberg, R. (2005) Results of the second Reynolds Cup contest in quantitative mineral analysis. International Union of Crystallography. *Commission on Powder Diffraction Newsletter*, **20**, 22–24.
Louwye, S. (2001) New species of dinoflagellate cysts from the Berchem formation, Miocene, northern Belgium (southern North Sea basin). *Geobios*, **34**, 121–130.
Louwye, S. (2005) The Early and Middle Miocene transgression at the southern border of the North Sea Basin (northern Belgium). *Geological Journal*, **40**, 441–456.
Louwye, S. and De Schepper, S. (2010). The Miocene–Pliocene hiatus in the southern North Sea Basin (northern Belgium) revealed by dinoflagellate cysts. *Geological Magazine*, **5**, 760–776.
Louwye, S. and Laga, P. (1998) Dinoflagellate cysts of the shallow marine Neogene succession in the Kalmthout well, northern Belgium. *Bulletin of the Geological Society of Denmark*, **45**, 73–86.
Louwye, S., De Coninck, J., and Verniers, S. (1999) Dinoflagellate cyst stratigraphy and depositional history of Miocene and Lower Pliocene formations in northern Belgium (southern North Sea basin). *Geologie en Mijnbouw*, **78**, 31–46.
Louwye, S., De Conick, J., and Verniers, J. (2000) Shallow marine Lower and Middle Miocene deposits at the southern margin of the North Sea Basin (northern Belgium): dinoflagellate cyst biostratigraphy and depositional history. *Geological Magazine*, **137**, 381–394.
Louwye, S., De Schepper, S., Laga, P., and Vandenberghe, N. (2006) The Upper Miocene of the southern North Sea Basin (northern Belgium): a palaeoenvironmental and stratigraphical reconstruction using dinoflagellate cysts. *Geological Magazine.* **144**, 33–52.
Maréchal, R. (1994) A new lithostratigraphic scale for the Palaeogene of Belgium. *Bulletin de la Société belge de Géologie*, **102**, 215–229.
McRae, S.C. (1972) Glauconite. *Earth-Science Reviews*, **8**, 397–440.
Meunier, A. (2005) *Clays*. Springer-Verlag, Berlin, 472 pp.
Meunier, A. and El Albani, A. (2007) The glauconite-Fe-illite-Fe-smectite problem: a critical review. *Terra Nova*, **19**, 95–104.
Moore, D.M. and Reynolds, R.C. Jr. (1997) *X-ray Diffraction and the Identification and Analysis of Clay Minerals*, second edition. Oxford University Press, Oxford, New York, 371 pp.
Odin, G.S., (1982) *Numerical Dating in Stratigraphy.* Wiley Interscience, New York, 1094 pp.
Odin, G.S. and Fullager, P.D. (1988) Geological significance of glaucony facies. Pp. 295–332 in: *Green Marine Clays* (G.S. Odin, editor). Developments in Sedimentology, **45**, Elsevier, Amsterdam.
Odin, G.S. and Matter, A. (1981) De glauconiarum origine. *Sedimentology*, **28**, 611–641.
Odin, G.S., Hunziker, J.C., Keppens, E., Laga, P.G., and Pasteels, P. (1974) Analyse radiométrique de glauconies par les méthodes au strontium et a l'argon; L'Oligo-Miocène de Belgique. *Bulletin de Société belge Géologie*, **83**, 35–48.
Omotoso, O., McCarthy, D.K., Hillier, S., and Kleeberg, R. (2006) Some successful approaches to quantitative mineral

analysis as revealed by the 3rd Reynolds Cup contest. *Clays and Clay Minerals*, **54**, 748–760.

Parry, W.T. and Reeves, Jr., C.C. (1966) Lacustrine glauconitic mica from Pluvial Lake Mound, Lynn and Terry Counties, Texas. *American Mineralogist*, **51**, 229–235.

Porrenga, D.H. (1968) Non-marine glauconitic illite in the Lower Oligocene of Aardebrug, Belgium. *Clay Minerals*, **7**, 421–430.

Potter, P.E., Maynard, B.J., and Depetris, J.P. (2005) *Mud and Mudstones*. Springer-Verlag, New York, 297 pp.

Sakharov, B.A., Lindgreen, H., Salyn, A.L., and Drits, V.A. (1999) Determination of illite-smectite structures using multispecimen X-ray diffraction profile fitting. *Clays and Clay Minerals*, **47**, 555–566.

Seed, D.P. (1968) The analysis of the clay content of some glauconite oceanic sediments. *Journal of Sedimentary Petrology*, **38**, 229–231.

Środoń, J., Drits, V.A., McCarty, D.K., Hsieh, J.C.C., and Eberl, D.D. (2001) Quantitative XRD analysis of clay-rich rocks from random preparations. *Clays and Clay Minerals*, **49**, 514–528.

Tedrow, J.C.F. (1986) *Soils of New Jersey*. Robert E. Krieger Publishing Company, Malabar, Florida, USA, 479 pp.

Tedrow, J.C.F. (2002) *Greensand and Greensand Soils of New Jersey: a review.* Department of Ecology, Evolution and Natural Resources Rutgers University, New Brunswick, New Jersey, USA, 40 pp.

Udgata, D.B.P. (2007) Glauconite as an indicator of sequence stratigraphic packages in a lower Paleocene passive-margin shelf succession, Central Alabama. Masters thesis, Auburn University, Alabama, USA, 124 pp.

Van Ranst, E. and De Coninck, F. (1983) Evolution of glauconite in imperfectly drained soils of the Belgian Campine. *Zeitschrift fur Pflanzenernahrung und Bodenkunde*, **146**, 415–426.

Vandenberghe, N., Laga, P., Steurbaut, E., and Vail, P.R. (1998) Tertiary sequence stratigraphy at the southern border of the North Sea basin in Belgium. *Mesozoic and Cenozoic Sequence Stratigraphy of European Basins*. SEPM special publication No **60**, pp. 119–154, Society for Sedimentary Geology, Tulsa, Oklahoma, USA.

Vandenberghe, N., Van Simaeys, S., Steurbaut, E., Jagt, J., and Felder, P. (2004) Stratigraphic architecture of the Upper Cretaceous and Cenozoic along the southern border of the North Sea Basin in Belgium. *Netherlands Journal of Geosciences-Geologie en Mijnbouw*, **83**, 155–171.

Velde, B. (1985) *Clay Minerals*. Developments in Sedimentology, **40**. Elsevier, Amsterdam, 427 pp.

Velde, B. and Meunier, A. (2008) *The Origin of Clay Minerals in Soils and Weathered Rocks*. Springer Verlag, Berlin, 406 pp.

Weaver, C.E. and Pollard, L.D. (1973) *The Chemistry of Clay Minerals*. Developments in Sedimentology, **15**, Elsevier Scientific Publishing Company, Amsterdam, London, New York, 213 pp.

Wignall, P.B. and Newton, R.J. (2001) Black shales on the basin margin: a model based on examples from the Upper Jurassic of the Boulonnais, northern France. *Sedimentary Geology*, **144**, 335–356.

Wilson, A.D. (1955) A new method for the determination of ferrous iron in rocks and minerals. *Bulletin of the Geological Survey of Great Britain*, **9**, 56–58.

Zeelmaekers, E. (2011) Computerized qualitative and quantitative clay mineralogy: Introduction and application to known geological cases. Doctoral dissertation, University of Leuven, Leuven, Belgium, 397 pp.

(*Received 2 July 2013; revised 2 February 2014; Ms 785; AE: H. Dong*)

Clays and Clay Minerals, Vol. 62, No. 1, 53–61, 2014.

RELATIVE HUMIDITY-INDUCED REVERSIBLE HYDRATION OF SULFATE-INTERCALATED LAYERED DOUBLE HYDROXIDES

S. Radha[1], K. Jayanthi[1], Josef Breu[2,*], and P. Vishnu Kamath[1,*]

[1] Department of Chemistry, Central College, Bangalore University, Bangalore-5600 01, India
[2] Department of Inorganic Chemistry I, University of Bayreuth, Bayreuth, Germany

Abstract—Layered double hydroxides (LDH) are extremely important materials for industrial processes and in the environment, and their physical-chemical behavior depends in large part on their hydration state, but the characterization of these hydration effects on their properties are incomplete. The present study was designed to explore the interpolytype transitions induced by variation in the ambient humidity among LDHs. The cooperative behavior of intercalated water molecules resulted in a sudden, single-step, reversible dehydration of the [Zn-Cr-SO_4] LDH. The [Zn-Al-SO_4] LDH provided an interesting contrast with (1) the coexistence of the end members of the hydration cycle over the 40−20% relative humidity range during the dehydration cycle, and (2) a random interstratified intermediate in the hydration cycle. These observations showed that the [Zn-Al-SO_4] LDH offered sites having a range of hydration enthalpies, whereby, at critical levels of hydration (20−40%), the non-uniform swelling of the structure resulted in an interstratified phase. The variation in domain size during reversible hydration was also responsible for the differences observed in the hydration *vs.* the dehydration pathways. This behavior was attributed to the distortion in the array of hydroxyl ions which departs from hexagonal symmetry on account of cation ordering as shown by structure refinement by the Rietveld method. This distortion was much less in the [Zn-Cr-SO_4] LDH, whereby the nearly hexagonal array of hydroxyl ions offered sites of uniform hydration enthalpy for the intercalated water molecules. In this case, all the water molecules experienced the same force of attraction and dehydrated reversibly in a single step. The changes in basal spacing were also accompanied by interpolytype transitions, involving the rigid translations of the metal hydroxide layers relative to one another.

Key Words—Cation Ordering, Layered Double Hydroxides, Polytype Transformation.

INTRODUCTION

Layered double hydroxides (LDHs) are a class of inorganic solids also called anionic clays. The better-known cationic clays consist of negatively charged aluminosilicate layers and intercalated cations (Weiss, 1963). The LDHs consist of positively charged metal hydroxide layers with anions included in the interlayer region. The metal hydroxide layers are derived from the structure of the mineral brucite (Oswald and Asper, 1977) and have the composition $[M^{II}_{(1-x)}M'^{III}_{x}(OH)_2](A^{n-})_{x/n}\cdot yH_2O$ (M^{II} = Mg, Fe, Ni, Co, Cu, Zn; M'^{III} = Al, Cr, Fe; A = Anion; $0.2 \leqslant x \leqslant 0.33$) (Reichle, 1986). The present study dealt with LDHs having the layer $[Zn_{0.67}M_{0.33}(OH)_2]^{0.33+}$ (M = Cr, Al) (Boehm *et al*., 1977). Anions and water molecules were incorporated into the interlayer region to restore charge neutrality. Two questions are often asked: (1) Is the position of the M' ion ordered with respect to the divalent cation or is the metal hydroxide layer cation disordered (Serna *et al*., 1982)? (2) In what manner are the atoms packed within the interlayer?

Evidence in favor of cation ordering is provided by an array of techniques such as extended X-ray absorption fine structure (Vucelic *et al*., 1997; Bigey *et al*., 1997; Roussel *et al*., 2000, 2001), magic angle spinning-nuclear magnetic resonance (Sideris *et al*., 2008, 2012; Cadars *et al*., 2011), and X-ray diffraction (XRD) (Krivovichev *et al*., 2010; Radha and Kamath, 2013). Cation ordering generates a large unit cell with $a = \sqrt{n} \times a_o$ (n = 3 for x = 0.33) (Hofmeister and Platen, 1992).

The second question is more difficult to answer given the inherent disorder in the interlayer, the high symmetry of the host layer, and the low atomic scattering factors of anions comprising light atoms. Where structure models are offered, the anions are located in the sites of high degeneracy with low site-occupancy factors (Besserguenev *et al*., 1997). Simulations based on molecular dynamics generally predict that the anion occupies a site close to that of the trivalent cations, which is the seat of the positive charge on the metal hydroxide layer (Li *et al*., 2006). The locations of the intercalated water molecules are also not determined with certainty. The O atoms of the intercalated water are often shown to share the same crystallographic sites as those of anions in the interlayer (Evans and Slade, 2005). Further LDHs intercalated with sulfate ions exhibit basal spacings ranging from 7.8 to 11.2 Å, based on the

* E-mail address of corresponding authors:
josef.breu@uni-bayreuth.de, vishnukamath8@hotmail.com
DOI: 10.1346/CCMN.2014.0620105

amount of intercalated water (Drits and Bookin, 2001). Likewise, LDHs intercalated with organic anions such as carboxylates exhibit humidity-driven hydration-dehydration phenomena, owing to their large hydration enthalpies, a fact that has been exploited for the facile aqueous exfoliation of these materials (Hibino and Kobayashi, 2005). The hydration-dehydration behavior of many simple inorganic anions in the [Mg-Al] system with different compositions of the metal hydroxide layer were investigated thoroughly by Iye *et al*. (2007) who found that, among others, the [Mg-Al] LDHs intercalated with SO_4^{2-}, ClO_4^-, and I^- exhibited basal spacing variation on being exposed to different relative humidities. While I^-- and ClO_4^--intercalated LDHs exhibited an ordered interstratified intermediate phase during hydration, SO_4^{2-}-LDH showed a one-step change in the basal spacing. Similar studies of [Mg-Al] and [Li-Al] LDHs intercalated with different anions were reported by Hou and Kirkpatrick (2000, 2002) and Hou *et al.* (2003). Based on those observations with different anions, the hydration behavior among LDHs were classified into three types: significantly expandable, slightly expandable, and non-expandable.

The diverse behavior of intercalated water molecules in different LDHs is on account of the different bonding interactions operating on them in the interlayer. These include (1) the hydration enthalpy of the anions, (2) the strength of the H-bonding with the metal hydroxide layer, and (3) the hydrogen bonding between the intercalated water molecules.

Among these, the last factor can vary considerably with the degree of hydration, leading to cooperative effects at the extreme end.

Dehydration results in a decrease in the number density of atoms in the interlayer. The objective of the present study was to examine if dehydration of the interlayer leads to a change in the stacking sequence of the metal hydroxide layer, thereby bringing about interpolytype transitions. Another objective was to examine if the differences in the structures of the two LDHs [Zn-M-SO_4] (M = Cr, Al) affect their respective hydration behaviors.

EXPERIMENTAL

Preparation of LDHs

Reagents used without further purification were $ZnCl_2$ (95% $ZnCl_2$ and $\leqslant$5% zinc oxide chloride), Al_2SO_4 (98%), and $ZnSO_4$ (99.5%) from Merck, India, and $CrCl_3$ (99%) and Na_2SO_4 (99%) from Aldrich Chemical Co., USA. [Zn-Al-SO_4] and [Zn-Cr-SO_4] LDHs were prepared by coprecipitation at constant pH values of 10 and 5, respectively. In a typical preparation, 50 mL of the mixed-metal salt solution (sulfates in the case of the [Zn-Al] LDH and chlorides in the case of the [Zn-Cr] LDH; $[Zn^{2+}]/[M^{3+}] = 2$; M = Al, Cr, total metal concentration 0.4 M) was added at a dosing rate of 0.14 mL/min to a reaction vessel (volume 400 mL) containing Na_2SO_4 salt solution (100 mL) in 10-times excess of the stoichiometric requirement. A constant pH was maintained during the synthesis by simultaneous addition of 0.5 N NaOH using a Metrohm Model 718 STAT Titrino (Herisau, Switzerland) operating in the pH STAT mode. The temperature was kept constant at 60ºC and N_2 was bubbled continuously. Boiled, deionized, Millipore Academic Water Purification System (Molsheim, France)-water was used throughout the synthesis to avoid possible carbonate contamination. The resulting slurry was aged for 15 h and separated by centrifugation followed by repeated washing with decarbonated water and finally with acetone. The precipitate obtained was then dried at 60ºC and stored in a desiccator.

Characterization

Both the samples were characterized by X-ray powder diffraction (XRPD) using a Bruker D8 Advance powder diffractometer (Karlsruhe, Germany) (source CuKα radiation, λ = 1.5418 Å). Data were collected at a continuous scan rate of 1º2θ min^{-1}. For structure refinement by the Rietveld method, data were collected over a 2θ range of 5−70º (step size 0.02º2θ, counting time 10 s/step). *In situ* measurements of XRPD patterns at different relative humidities were carried out using a PANalytical X'pert X-ray diffractometer (Almelo, The Netherlands) (CuKα radiation, λ = 1.5418 Å, Bragg-Brentano geometry) equipped with an X'celerator Scientific RTMS detector and an Anton Paar temperature humidity chamber (Graz, Austria) driven by a VTI Corp. RH-200 humidity generator (Graz, Austria). Measurements were done at different relative humidity (RH) values ranging from <5% (referred to hereafter as 0%) to 98% (referred to hereafter as 100%) at intervals of 10%. The sample was allowed to equilibrate for a period of 60 min at each RH value before performing the XRD measurements. Data were collected from 5 to 70º2θ with a step size of 0.017º2θ at a scan rate of 1º/min.

Infrared spectra of the samples were recorded using a Bruker Alpha-P FTIR spectrometer (Ettlingen, Germany) (ATR mode, diamond crystal, 400−4000 cm^{-1}, 4 cm^{-1} resolution). Thermogravimetric analyses were carried out using a Mettler Toledo 851^e TGA/SDTA system (Schwerzenbach, Switzerland). The samples were dried at 100ºC for 30 min in the TG balance and then the temperature was ramped from 100 to 800ºC at a heating rate of 5ºC/min under N_2 flow. The Zn and Al contents in the LDH were estimated by means of atomic absorption spectroscopy using a Varian Model AA240 atomic absorption spectrometer (Victoria, Australia). The sulfate content present was estimated by wet chemical analysis by precipitation as $BaSO_4$. The [Zn]/[M] ratio (M = Al, Cr) was close to 2 in all the samples, which is consistent with earlier reports (Boclair *et al*., 1999). In all cases, the estimated sulfate content

was lower than the stoichiometric requirement to balance the positive charge. This deficiency was made up by the inclusion of carbonate ions to arrive at an approximate formula for each of the LDHs. In each case, the carbonate content was negligible (~0.02 mol per empirical formula unit) and, for all practical purposes, the LDHs were treated as though they were carbonate-free and abbreviated with the symbol [Zn-*M*-SO_4] (*M* = Cr, Al).

Computational studies

The powder patterns obtained were indexed using the program *PROZSKI* (Lasocha and Lewiniski, 1994) and the figure of merit (FM) obtained. *DIFFaX* (Treacy *et al*., 1991, 2000), a FORTRAN-based computer program, was used to simulate the XRPD patterns corresponding to different polytypes and model structural disorder where necessary. The *DIFFaX* formalism treats a solid as a stacking of layers of atoms. The position coordinates corresponding to atoms present in the metal hydroxide layer and the interlayer were defined according to the published structure models [CC no**:** 91860 (1*H* polytype); 91859 ($3R_1$ polytype)]. Different polytypes were simulated by varying the stacking vectors.

The XRPD patterns of different polytypes differed from each other in the positions and relative intensities of the reflections appearing in the mid-2θ region (30−55º2θ). Polytypes were identified primarily by comparing the observed peak positions with those expected of different polytypes. The reflections were also indexed to obtain the refined cell parameters, an exercise which yielded the crystal symmetry. The refined *c* parameter yielded the number of layers per unit cell. A full profile match of the observed pattern with that of the corresponding polytype was then attempted by *DIFFaX* simulations. Where the samples were ordered, a full profile match between the observed and calculated XRPD patterns was obtained. In some instances, there was a mismatch in the relative intensities of selected reflections. Such mismatch, if any, arose due to: (1) orientational effects of lamellar crystallites which accentuate the intensities of the basal reflections, and (2) structural disorder due to the incorporation of small proportions of stacking faults which affect reflections appearing in the mid-2θ region. In this work, minor variations in the relative intensities of reflections appearing in mid-2θ region were ignored for the purpose of polytype identification.

The structure of the [Zn-Al-SO_4] LDH was refined by the Rietveld method using the *GSAS* software package (Larson and Von Dreele, 2004). A TCH pseudo-Voigt line-shape function (Profile function 2) with seven variables was used to fit the experimental profile. The refinable profile parameters included asymmetric peak shape, sample displacement, and parameters U_G, V_G, and W_G and X_L and Y_L for Gaussian and Lorentzian contributions, respectively.

During refinement, restraints were placed on the S−O (1.4±0.1 Å) bond length and O−S−O bond angle (109±1º) in the initial cycles of the refinement. The position coordinates and SOF (Site occupancy factors) were refined one atom at a time, keeping the parameters of other atoms fixed in order to achieve a stable refinement. In the final cycles of the refinement, the restraints placed on the sulfate structure were removed while keeping the structure of the metal hydroxide layer fixed. Attempts to refine the structure by freeing up all the parameters at the same time did not lead to stable refinement.

RESULTS

[Zn-Cr-SO_4] LDH

The as-prepared [Zn-Cr-SO_4] LDH exhibited a basal reflection at 9.8º2θ. The observed reflections were indexed to a cell of hexagonal symmetry with a refined *c* = 8.93 Å (Table 1, Supporting Information SI 1, available from the journal's data depository at http://www.clays.org/JOURNAL/JournalDeposits.html) which shows that the compound belongs to the 1*H* polytype (see trace labeled 'Ambient' in Figure 1). Composition analysis yielded the approximate formula $[Zn_{0.67}Cr_{0.33}(OH)_2][(SO_4)_{0.148}(CO_3)_{0.018}]\cdot 0.4\ H_2O$.

The observed basal spacing corresponds to a hydrated structure with a layer of intercalated water molecules. Therefore, the sample was first dehydrated by equilibration at RH ⩽5% (3 h). The first basal spacing shifted to 8.6 Å (10.1º2θ). The reflections in the mid-2θ region

Table 1. Composition, relative humidity, corresponding cell parameters, figure of merit (FM), and polytype of the [Zn-*M*-SO_4] (*M* = Cr, Al) LDHs.

Composition (Relative Humidity)	*a* (Å)	*c* (Å)	FM	Polytype
$[Zn_{0.67}Cr_{0.33}(OH)_2][(SO_4)_{0.148}(CO_3)_{0.018}]\cdot 0.4H_2O$ (Ambient)	3.11	8.93	61.2	1*H*
0% RH	3.11	25.65	24.3	$3R_1$
10% RH	3.13	8.95	55.2	1*H*
100% RH	3.12	32.7	23.0	$3R_1$
$[Zn_{0.67}Al_{0.33}(OH)_2][(SO_4)_{0.144}(CO_3)_{0.02}]\cdot 1.03H_2O$ (Ambient)	5.34	11.14	23.39	1*H*
10% RH	3.06	25.77	18.6	$3R_1$

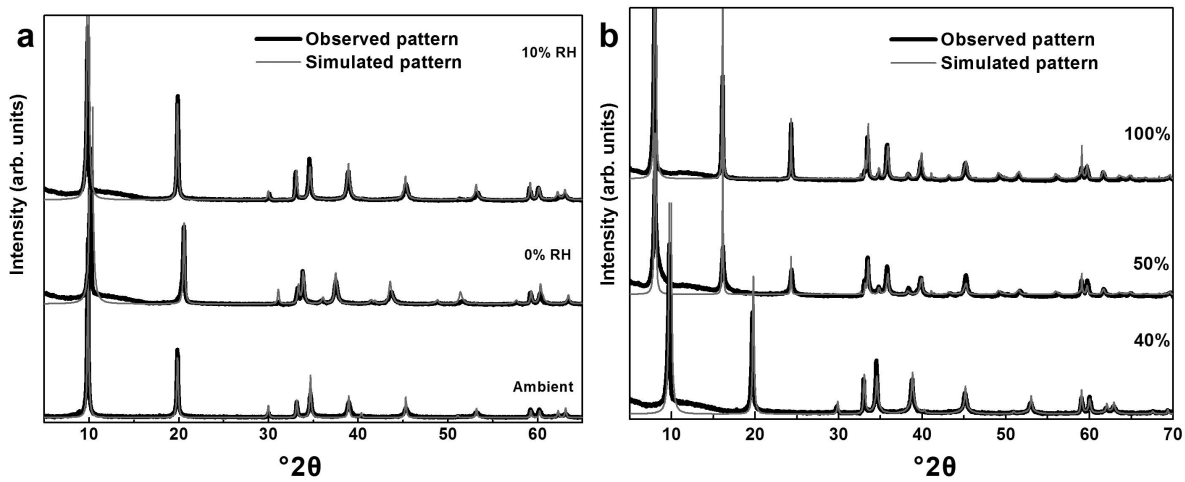

Figure 1. XRPD pattern of the as-prepared [Zn-Cr-SO_4] LDH and under various relative humidities from 0 to 100% obtained during the hydration cycle. In each case the observed pattern is overlain with the corresponding *DIFFaX* simulation.

shifted to new positions and were then indexed to a cell of rhombohedral symmetry (-h + k + l = 3n, Supporting Information SI. 1). The observation of the 012, 015, and 108 reflections, to the exclusion of the 104 and 107 reflections, was indicative of the 3R_1 polytype. The refined cell parameters (a = 3.11 Å, c = 25.65 Å; FM = 24.3) corresponded to a unit cell of three layers and this sample was, thus, referred to as an 8.6 Å-3R_1 polytype. On increasing the RH to 10% (Figure 1), the 8.6 Å-3R_1 phase reverted to the as-prepared 8.8 Å-1H phase, which remained stable with a slight increase in basal spacing to 9.0 Å until the RH reached a value of 40%. At 50% RH a sudden one-step increase in the basal spacing to 11 Å was accompanied by the structural transformation to a new 3R_1 phase. The 3R_1 polytype thus formed remained stable up to >98% RH (Table 1, Supporting Information SI. 1).

During dehydration, the 11 Å-3R_1 hydrated phase remained stable until 40% RH. At 30% RH, a sudden one-step decrease in basal spacing to 8.8 Å with the polytype transformation from 3R_1 to 1H was observed (Figure 2). Further decrease in RH stepwise to <5% generated the 8.6 Å-3R_1 phase as earlier. The transformations observed during the hydration cycle were, thus, reversible. The basal spacing variations occurring during the hydration process are shown in Supporting Information SI. 2 and the humidity-driven interpolytype transformations are summarized in Supporting Information SI. 3.

Some of the results described here are similar to the reports by Khaldi *et al.* (1997) which were *ex situ* measurements. Structural changes at different water-vapor pressures were reported by Mostarih and de Roy (2006) and compared to those under vacuum.

[Zn-Al-SO_4] LDH

The XRPD pattern of the as-prepared [Zn-Al-SO_4] LDH exhibited a basal spacing of 10.9 Å (8.1°2θ) (Figure 3a) corresponding to a bilayer arrangement of water molecules in the interlayer. The XRPD pattern is similar to that expected of a 1H polytype (a = 5.34 Å c = 11.09 Å, FM = 23.4, Table 1, Supporting Information SI.4). The approximate formula derived on the basis of composition analysis was $[Zn_{0.67}Al_{0.33}(OH)_2][(SO_4)_{0.144}(CO_3)_{0.02}]\cdot 1.03\ H_2O$.

The larger a parameter of this phase (a = 5.34 Å = $\sqrt{3} \times a_o$), compared to that of the more prevalent phases (a_o = 3.11 Å), corresponded to a cation-ordered cell and the corresponding supercell reflections 100 and 101 were observed at 19.2 and 20.8°2θ, respectively. The structure of this phase was refined using the cation-ordered structure model (space group $P\bar{3}$) proposed for the [Zn-Cr-SO_4] LDH (Radha and Kamath, 2013). Details of the structure (Supporting Information SI. 5–9) are available from the Cambridge Crystallography Data Centre (CCDC 975959).

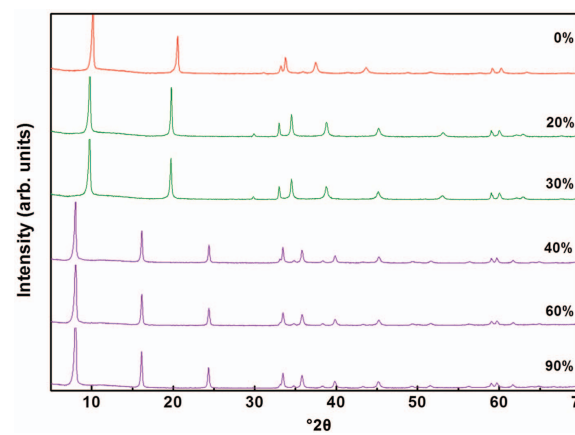

Figure 2. Evolution of XRPD patterns of [Zn-Cr-SO_4] LDH during the dehydration cycle as a function of varying relative humidity.

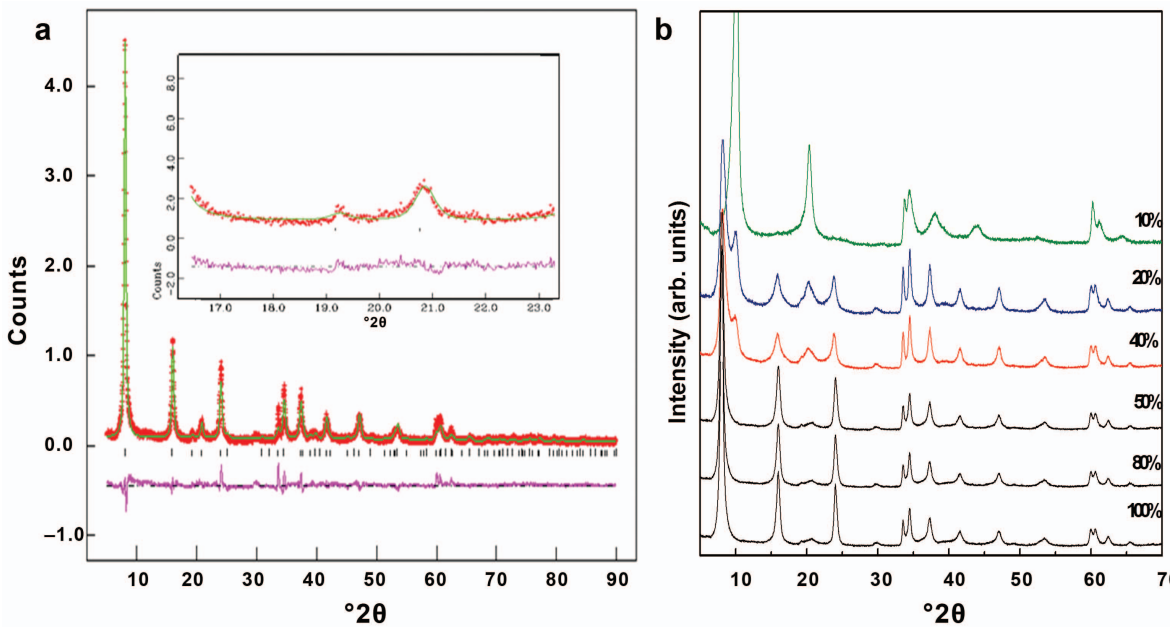

Figure 3. (a) Rietveld fit of the XRPD pattern of the [Zn-Al-SO_4] LDH. (Inset) Details of the fit of the supercell reflections. (b) Evolution of XRPD patterns of [Zn-Al-SO_4] LDH during the dehydration cycle as a function of relative humidity.

The as-prepared phase in the [Zn-Al] system is highly hydrated and on equilibration at RH ~98% for 3 h, no further hydration was observed. On step-wise reduction of the relative humidity, the 10.9 Å-1*H* phase was stable up to a RH value of 50%. At 40% RH, an 8.8 Å (10.1º2θ) reflection emerged along with the 10.9 Å peak, indicating the coexistence of two different phases (Figure 3b). The 8.8 Å peak and its higher order at ~4.4 Å (20.4º2θ) grew in intensity with further decrease in RH and continued to coexist with the 10.9 Å-1*H* phase up to 20% RH. The simultaneous appearance of the basal reflections of the end members showed that the sample at the 40−20% RH range is a physical mixture of hydrated phase and the dehydrated phase. At 10% RH the biphasic mixture was completely transformed into the 8.8 Å-3R_1 phase (Table 1, Supporting Information SI. 4). This 3R_1 phase remained stable below 5% RH with a slight decrease in basal spacing to 8.7 Å.

The dehydrated phase was then subjected to the hydration cycle, with a stepwise increase in RH from 10% to 100% (Figure 4). The 8.7 Å-3R_1 phase was observed until 10% RH. On increasing the RH to 20%, the basal reflection was split into two, indicating the coexistence of two phases corresponding to 8.8 Å and

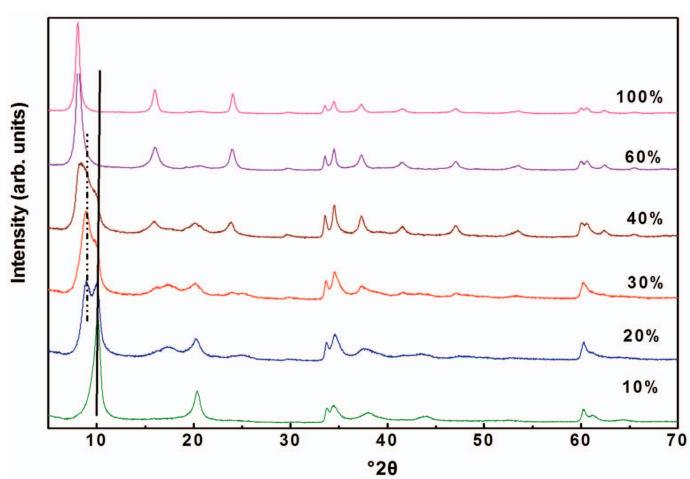

Figure 4. Evolution of the XRPD patterns of [Zn-Al-SO_4] LDH during the hydration cycle as a function of relative humidity. The solid vertical line corresponds to the basal spacing of the dehydrated phase. The broken vertical line corresponds to the peak due to the staged phase.

9.9 Å. The 9.9 Å phase observed here corresponded to a random interstratified phase of the two end members (c = 11 Å and 8.8 Å) with a ~1:1 ratio. At 30% RH the 9.9 Å phase was dominant. Further increase in RH merged the two basal reflections and then gradually shifted it toward higher d values and a series of irrational basal reflections observed at 10.5 Å (40% RH), 10.6 Å (50% RH), 10.7 Å (60% RH), and 10.8 Å (70% RH) corresponding to increasing amounts of the bilayer hydrate being incorporated into the stacking before forming a fully hydrated phase corresponding to 11 Å at ~98% RH (Supporting Information SI. 2 and 10). These are the various randomly interstratified phases corresponding to different proportions of the end members, demonstrating Mering's principle (1946) that is widely used among cationic clays to demonstrate interstratification phenomena. The stacking sequence of the adjacent metal hydroxide layers was different in the two end members of the hydration cycle. Consequently, at intermediate degrees of hydration, stacking modes corresponding to both end members coexisted as was shown by the presence of different *hkl* reflections of the two end members concomitantly with the irrational 00*l* series (Figure 5). The basal reflections in the observed pattern appeared at positions intermediate between those expected of the end members in keeping with the predictions made by Mering's rules for interstratified phases. These observations are unlike those in the dehydration cycle where only the two end members with basal spacings of 8.8 Å and 11 Å, respectively, coexisted.

To conclude, the [Zn-Cr-SO_4] LDH underwent a one-step reversible hydration while in the case of the [Zn-Al-SO_4] LDH the behavior during hydration was different from that during dehydration.

DISCUSSION

The two LDHs studied here have the same composition ([Zn]/[M] = 2; M = Al, Cr). Both the LDHs are cation-ordered. Cation ordering brings down the crystal symmetry to $P\bar{3}$, compared to the $R\bar{3}m$ crystal symmetry of the cation disordered phase. In a cation-disordered phase, the [$M(OH)_6$] coordination polyhedron is symmetric (coordination symmetry $\bar{3}m$, D_{3d}), with a single M(Zn, M^{III})−O distance, resulting in a perfectly hexagonal array of hydroxyl ions on either side of the cation layer.

In a cation-ordered metal hydroxide layer, the coordination polyhedron [$M^{III}(OH)_6$] is regular with a single M^{III}−O (M^{III} = Al, Cr) bond distance. The coordination polyhedron around [$Zn(OH)_6$] is greatly distorted with two different Zn−O bond lengths. The three long bonds define one triangular face of the polyhedron and the three short bonds define the opposite face; this pair of faces is perpendicular to the c crystallographic axis and the stacking direction.

As the position of the cations is centric (z is 0.0 for both Zn and M^{III}), the distortion in the coordination polyhedra is manifest in the distortion of the array of the hydroxyl ions. Three non bonded in-plane O1−O1 (O1: Hydroxyl O atom) distances exist, whereas for a perfectly hexagonal array, as in the $3R_1$ polytype (Radha and Kamath, 2013), only one distance exists at 3.12 Å (Figure 6). A comparison of the hydroxyl ion array in the two LDHs shows that the distortion from

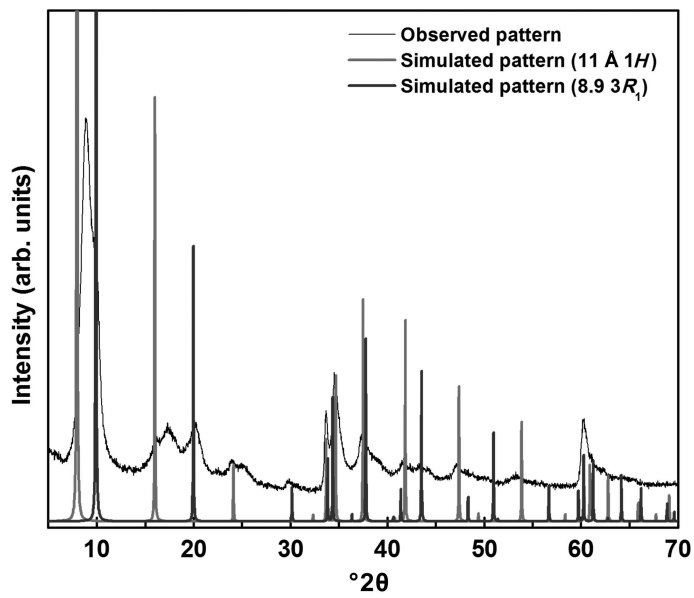

Figure 5. XRPD patterns of [Zn-Al-SO_4] LDH at 30% RH during the hydration cycle overlain with the simulated patterns of the two end members. Peaks unaccounted for by the simulated patterns correspond to the interstratified phase.

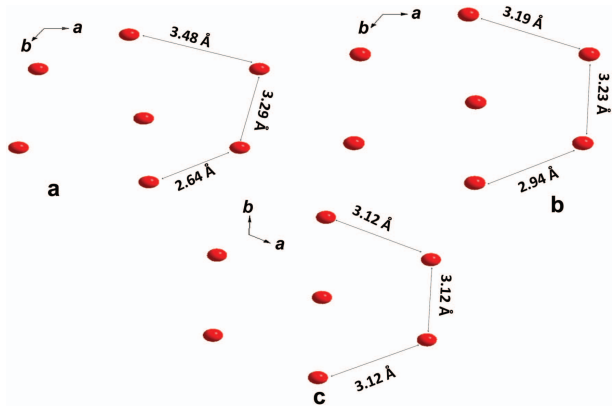

Figure 6. A hydroxyl array of (a) cation-ordered [Zn-Al-SO_4] , (b) cation-ordered [Zn-Cr-SO_4], and (c) cation-disordered [Zn-Cr-SO_4].

hexagonal symmetry is much less in [Zn-Cr-SO_4] (O1−O1: 2.93, 3.19, 3.23 Å) than in [Zn-Al-SO_4] (O1−O1: 2.64, 3.29, 3.48 Å).

The differences in the hydration-dehydration behavior of these two sulfate-intercalated LDH systems may be interpreted in terms of two competing interactions involving water molecules in the interlayer: (1) hydrogen bonding with the array of hydroxyl ions defining the surface of the metal hydroxide layers; and (2) hydrogen bonding interactions with other intercalated water molecules.

If the array of hydroxyl ions defining the surface of the metal hydroxide layer were to be of perfectly hexagonal symmetry as in a cation disordered structure or only slightly distorted as in [Zn-Cr-SO_4] LDH, the water molecule would encounter sites of a single hydration enthalpy as offered by a layer having a uniform charge distribution. This would lead to a single-step hydration with sudden and discontinuous swelling followed by single-step dehydration – the cooperative effects introducing hysteresis. Such behavior was observed in [Zn-Cr-SO_4] LDH and was similar to that observed for most of the synthetic clays (Breu *et al*., 2001).

In the [Zn-Al-SO_4] LDH, however, the highly distorted array of hydroxyl ions would offer sites with wide variations in the hydration enthalpy, arising out of a non-uniform charge distribution. The closely spaced hydroxyl ions (O1−O1: 2.64 Å) offer sites of greater hydration enthalpy compared to those more distant from one another (O1−O1: 3.48 Å). In such a situation the forces operating between the array of the hydroxyl ion and the intercalated water also vary with the degree of hydration. The incoming water molecules in the initial stage of the hydration cycle are predominantly influenced by the metal hydroxide layer. As hydration proceeds, the incoming water molecules interact increasingly with other water molecules and are screened from the metal hydroxide layer. Because the interlayer water molecules are disordered, the ingress of water molecules also takes place in a disordered fashion leading to randomly interstratified phases with irrational basal spacings. Once the LDH is fully hydrated, the $3R_1$ polytype completely transforms to the structure of the $1H$ polytype. The reversible $3R_1 \rightarrow 1H$ transformation is realized by the rigid translations of successive metal hydroxide layers relative to one another.

Another anion closely related to SO_4^{2-} is $S_2O_3^{2-}$. The reversible hydration behavior of the [Zn-Al-S_2O_3] LDH (Radha *et al*., 2013) offers an interesting comparison with two significant differences: (1) the end members of the hydration-dehydration cycle both adopt the structure of the $3R_1$ polytype and no detectable interpolytype transitions are noted; and (2) both end members coexist over a significant range of RH values (40−60%). Irrational basal reflections are not observed under any conditions, ruling out the possibility of the existence of interstratified phases. The coexistence of the end members was, therefore, attributed to kinetic factors (Radha *et al*., 2013).

An explanation based on factors related to kinetics is also plausible for the hydration behavior of the [Zn-Al-SO_4] LDH. The observation of irrational basal reflections (Figure 5) tilts the balance of judgment in favor of the stabilization of an interstratified phase, however. Why is the hydration cycle different from the dehydration cycle in the [Zn-Al-SO_4] LDH? Probably because of the domain-size variation which changes with the degree of hydration. A fully hydrated phase would have a larger domain size, due to the uniform and complete ingress of water, into the LDH crystal. As dehydration begins, the water molecules are lost from sites of low hydration enthalpy resulting in XRPD patterns akin to that of a mixed phase. On complete dehydration, the domain size decreases as uneven dehydration causes the breakup of domains. During rehydration, the domains are expected to grow again. Below an average critical domain size, less than the coherent scattering length of the X-rays, however, uneven hydration of the LDH crystallites yields an XRPD pattern akin to that of a randomly interstratified phase.

All these changes are also accompanied by interpolytype transformations between $1H$ and $3R_1$ which are realized by rigid translations of successive metal hydroxide layers relative to one another.

CONCLUSIONS

Structure refinement by the Rietveld fit of the XRPD patterns showed that the metal hydroxide layers are cation ordered in both the [Zn-Cr] and [Zn-Al] LDHs. Cation ordering induces a distortion in the array of hydroxyl ions and consequently in its charge distribution, generating sites of different hydration enthalpies within the interlayer. This distortion was more pronounced in the case of [Zn-Al] than in [Zn-Cr]. The [Zn-Al] LDH underwent non-uniform hydration, therefore, leading to a randomly interstratified intermediate over a range of relative humidity values, whereas the [Zn-Cr] LDH underwent a single-step hydration-dehydration.

ACKNOWLEDGMENTS

The authors from India thank the Department of Science and Technology (DST), and the University Grants Commission (UGC), Government of India (GOI) for financial support. S. R. thanks the German Research Foundation (SFB 840) for supporting a visit to the University of Bayreuth and the Council for Scientific Industrial Research, GOI, for the award of a Senior Research Fellowship. K.J. thanks the UGC, GOI, for a Project Fellowship. P.V.K. is a recipient of the Ramanna Fellowship of the DST, GOI.

Supporting Information: List of Bragg reflections, basal spacing dynamics, reversible dehydration schemes, plot of the crystal structures of [Zn-Al-SO_4] LDH, and the results of the Rietveld refinement.

REFERENCES

Besserguenev, A.V., Fogg, A.M., Francis, R.J., Price, S.J., and O'Hare, D. (1997) Synthesis and structure of the gibbsite intercalated compounds $[LiAl_2(OH)_2]X$ {X = Cl, Br, NO_3}and $[LiAl_2(OH)_6]Cl.H_2O$ using synchronton X-ray and neutron powder diffraction. *Chemistry of Materials*, **9**, 241–247.

Bigey, L., Depege, C., de Roy, A., and Besse, J.P. (1997) EXAFS and XANES study of layered double hydroxides. *Journal de Physique IV*, **7**, 949–950.

Boclair, J.W., Braterman, P.S., Jiang, J., Lou, S., and Yarberry, F. (1999) Layered double hydroxides stability. 2. Formation of Cr (III)-containing layered double hydroxides directly from solution. *Chemistry of Materials*, **11**, 303–307.

Boehm, H.P., Steinle, J., and Vieweger, C. (1977) $[Zn_2Cr(OH)_6]x.2H_2O$, new layer compounds capable of anion exchange and intracrystalline swelling. *Angewandte Chemie*, **16**, 265–266.

Breu, J., Seidl, W., Stoll, A.J., Lange, K.G., and Probst, T.U. (2001) Charge homogenity in synthetic fluorohectorite. *Chemistry of Materials*, **13**, 4213–4220.

Cadars, S., Layrac, G., Gerardin, C., Deschamps, M., Yates, J.R., Tichit, D., and Massiot, D. (2011) Identification and quantification of defects in the cation ordering in Mg/Al layered double hydroxides. *Chemistry of Materials*, **23**, 2821–2831.

Drits, V.A. and Bookin, A.S. (2001) Crystal structure and X-ray identification of layered double hydroxides. Pp. 39–92 in: *Layered Double Hydroxides: Present and Future* (V. Rives, editor). Nova Science, New York.

Evans, D.G. and Slade, R.C.T. (2005) *Structural Aspects of Layered Double Hydroxides in Layered Double Hydroxides* (X. Duan and D.G. Evans, editors). Springer, Berlin.

Hibino, T. and Kobayashi, M. (2005) Delamination of layered double hydroxides in water. *Journal of Materials Chemistry*, **15**, 653–656.

Hofmeister, W. and Platen, H.V. (1992) Crystal chemistry and atomic order structures in brucite-related double-layer structure. *Crystallography Reviews*, **3**, 3–26.

Hou, X. and Kirkpatrick, R.J. (2000) Solid-State ^{77}Se NMR and XRD study of the structure and dynamic of selenooxyanions in hydrotalcite-like compounds. *Chemistry of Materials*, **12**, 1890–1897.

Hou, X. and Kirkpatrick, R.J. (2002) Interlayer structure and dynamics of ClO_4^- layered double hydroxides. *Chemistry of Materials*, **14**, 1195–1200.

Hou, X., Bish, D.L., Wang, S.L., Johnston, C.T., and Kirkpatrick, R.J. (2003) Hydration, expansion, structure, and dyanamics of layered double hydroxides. *American Mineralogist*, **88**, 167–179.

Iye, N., Fujii, K., Okamoto, K., and Sasaki, T. (2007) Factors influencing the hydration of layered double hydroxides (LDHs) and the appearance of an intermediate second staging phase. *Applied Clay Science*, **35**, 218–227.

Khaldi, M., de Roy, A., Chaouch, M., and Besse, J.P. (1997) New varieties of zinc-chromium-sulfate lamellar double hydroxides. *Journal of Solid State Chemistry*. **130**, 66–73.

Krivovichev, S.V., Yakovenchuk, V.N., Zhotova, E.S., Zolotarev, A.A., Pakhomovsky, Y.A., and Ivanyuk, G.Yu. (2010) Crystal chemistry of natural layered double hydroxides. I. Quintinite-2H-2c from Kovdor Alkaline Massif, Kola Peninsula, Russia. *Mineralogical Magazine*, **74**, 821–832.

Larson, A.C. and Von Dreele, R.B. (2004) General Structure Analysis System (GSAS), Los Almos National Laboratory Report LAUR 86-748. Los Almos National Laboratory, Los Almos, NM.

Lasocha, W. and Lewiniski, K. (1994) PROSZKI, a system of programs for powder diffraction data analysis Version 2.4. Krakow, Poland.

Li, H., Ma, J., Evans, D.G., Zhou, T., Li, F., and Duan, X. (2006) Molecular dynamics modeling of the structure and binding energies of α-nickel hydroxides and nickel-aluminium layered double hydroxide containing various interlayer guest anions. *Chemistry of Materials*, **18**, 4405–4414.

Mering, J. (1949) L'interférence des rayons X dans les systèmes à stratification désordonée. *Acta Crystallographica*, **2**, 371–377.

Mostarih, R. and de Roy, A. (2006) Thermal behavior of a zinc-chromium-sulfate lamellar double hydroxide revisited as a function of vacuum and moisture parameter. *Journal of Physics and Chemistry of Solids*, **67**, 1058–1062.

Oswald, H.R. and Asper, R. (1977) *Preparation and Crystal Growth of Materials with Layered Structures* (R.M.A. Leith, editor). Riedel Publishing Company, Dordrecht, The Netherlands, pp. 71–140.

Radha, S. and Kamath, P.V. (2013) Polytypism in sulfate-intercalated layered double hydroxides of Zn and M(III) (M = Al, Cr): Observation of cation ordering in the metal hydroxide layers. *Inorganic Chemistry*, **52**, 4834–4841.

Radha, S., Milius, W., Breu, J., and Kamath, P.V. (2013) Synthesis and reversible hydration behavior of the thiosulfate intercalated layered double hydroxide of Zn and Al. *Journal of Solid State Chemistry*, **204**, 362–366.

Reichle, W.T. (1986) Synthesis of anionic clay minerals (mixed metal hydroxides, hydrotalcite). *Solid State Ionics*,

22, 135–141.

Roussel, H., Briois, V., Elkaim, E., de Roy, A., and Besse, J.P. (2000) Cationic order and structure of [Zn-Cr-Cl] and [Cu-Cr-Cl] layered double hydroxides: An XRD and EXAFS study. *Journal of Physical Chemistry B*, **104**, 5915–5923.

Roussel, H., Briois, V., Elkaim, E., de Roy, A., Besse, J.P., and Jolivet, J.P. (2001) Study of the formation of the layered double hydroxide [Zn-Cr-Cl]. *Chemistry of Materials*, **13**, 329–337.

Serna, C.J., Rendon, J.L., and Iglesias, J.E. (1982) Crystal-chemical study of layered $[Al_2Li(OH)_6]^+X^-{\cdot}nH_2O$. *Clays and Clay Minerals*, **30**, 180–184.

Sideris, P.J., Nielson, U.G., Gan, Z., and Grey, C.P. (2008) Mg/Al ordering in layered double hydroxides revealed by multinuclear NMR spectroscopy. *Science*, **321**, 113–117.

Sideris, P.J., Blanc, F., Gan, Z., and Grey, C.P. (2012) Identification of cation clustering in Mg-Al layered double hydroxides using multinuclear solid state nuclear magnetic resonance spectroscopy. *Chemistry of Materials*, **24**, 2449–2461.

Treacy, M.M.J., Newsam, J.M., and Deem, M.W. (1991) A general recursion method for calculating diffracted intensities from crystals containing planar faults. *Proceedings of the Royal Society*, *London*, **A433**, 499–520.

Treacy, M.M.J., Deem, M.W., and Newsam, J.M. (2000) *Computer Code DIFFaX*, *Version 1.807*. NEC Research Institute, Inc., Princeton, New Jersey, USA.

Vucelic, M., Jones, W., and Moggridge, G.D. (1997) Cation ordering in synthetic layered double hydroxides. *Clays and Clay Minerals*, **45**, 803–813.

Weiss, A. (1963) A secret of Chinese porcelain manufacture. *Angewandte Chemie*, **75**, 755–762.

(*Received 13 September 2013; revised 25 February 2014; Ms. 812; AE: M. Plötze*)

Clays and Clay Minerals, Vol. 62, No. 1, 62–73, 2014.

DIELECTRIC RELAXATION OF WATER IN CLAY MINERALS

Maria A. Vasilyeva[1], Yuri A. Gusev[1,*], Valery G. Shtyrlin[2], Anna Greenbaum (Gutina)[3], Alexander Puzenko[3], Paul Ben Ishai[3], and Yuri Feldman[3]

[1] The Kazan Federal University, Institute of Physics, Kremlevskaya st. 18, 420008, Kazan, Russian Federation
[2] The Kazan Federal University, A.M. Butlerov Chemistry Institute, Kremlevskaya st. 18, 420008, Kazan, Russian Federation
[3] The Hebrew University of Jerusalem, Department of Applied Physics, Edmond J. Safra Campus, Givat Ram 91904, Jerusalem, Israel

Abstract—The study of confined water dynamics in clay minerals is a very important topic in aluminosilicate-surface chemistry. Aluminosilicates are among the most technologically versatile materials in industry today. Dielectric spectroscopy is a very useful method for investigating the structure and dynamics of water adsorbed on solid matrix surfaces and water in the vicinity of ions in solutions. Use of this method for the study of clay minerals has been underutilized to date, however. The main goal of the present research was to understand the relaxation mechanisms of water molecules interacting with different hydration centers in clay minerals, with a view to eventually control this interaction. Two types of natural layered aluminosilicates (clay minerals) – montmorillonite with exchangeable K^+, Co^{2+}, and Ni^{2+} cations and kaolinite with exchangeable K^+ and Ba^{2+} cations – were examined by means of dielectric spectroscopy over wide ranges of temperature (from −121ºC to +300ºC) and frequency (1 Hz–1 MHz). An analysis of the experimental data is provided in terms of four distributed relaxation processes. The low-temperature relaxation was observed only in montmorillonites and could be subdivided into two processes, each related to a specific hydration center. The cooperative behavior of water at the interface was observed in the intermediate temperature region, together with a proton percolation. The dielectric properties of ice-like and confined water structures in the layered clay minerals were compared with the dielectric response observed in porous glasses. The spatial fractal dimensions of the porous aluminosilicates were calculated by two separate methods – from an analysis of the fractality found in photomicrographs and from the dielectric response.

Key Words—Adsorbed Water, Dielectric Spectroscopy, Exchangeable Cations, Fractal Dimension, Kaolinite, Montmorillonite.

INTRODUCTION

The large specific surface area, chemical and mechanical stability, variety of structural and surface properties, large values of cation exchange capacities, *etc.*, make the clay minerals an excellent group of adsorbents (Greg and Sing, 1967; Gupta and Bhattacharyya, 2012; Kiselev, 1986; Tarasevich, 1988; Tarasevich and Ovcharenko, 1975; Volzone *et al.*, 1999). Consequently, the hydration properties of clay materials are a fundamental problem in any field of their application.

One of the most useful tools for investigating the structure and dynamics of adsorbed water on solid matrix surfaces is Dielectric Spectroscopy (DS) (Gutina *et al.*, 2003; Saltas *et al.*, 2007; Spanoudaki *et al.*, 2005; Wander and Clark, 2008). Broadband Dielectric Spectroscopy (or impedance spectroscopy) occupies a special place among the numerous modern methods used for the physical and chemical analysis of materials. By measuring the electric polarization of a dielectric material under the influence of an external time-dependent electric field at different temperatures, investigation of relaxation processes with an extremely wide range of characteristic times (10^5–10^{-13} s) and monitoring different scales of molecular motions are possible (Kremer and Schoenhals, 2002; Feldman *et al.*, 2006). In particular, DS is sensitive to cooperative intermolecular interactions (Feldman *et al.*, 2006) and, thus, provides a link between the properties of the individual constituents of a complex material *via* molecular spectroscopy and the characterization of its bulk properties. Many key aspects of a material's properties can be derived from the complex dielectric functions, *e.g.* the strength and the shape parameters of molecular relaxations, the characterization of structural phase transitions, the activation energy of the relaxation process, charge mobility, *etc*. Moreover, this method is very sensitive to water dynamics in ionic aqueous solutions and can provide important information on the state of water in the vicinity of ions (Levy *et al.*, 2012).

The clay minerals represent a class of materials where the two types of water organization mentioned above can be observed simultaneously. Several attempts have been made to perform dielectric measurements of hydrated kaolinites and montmorillonites over narrow frequency and temperature ranges by changing the temperature at a fixed frequency or *vice versa* (Calvet, 1975; Hall and Rose, 1978; Hoekstra and Doyle, 1971; Lockhart, 1980a, 1980b; Mamy, 1968; Raythatha and Sen, 1986; Sposito

* E-mail address of corresponding author:
ygusev@mail.ru
DOI: 10.1346/CCMN.2014.0620106

and Prost, 1982). Recently, the increased interest in hydrated clay minerals has stimulated research in this field, primarily to correlate the electrical properties with their structural parameters and water content (Ishida *et al.*, 2000; Kaviratna *et al.*, 1996; Logsdon and Laird, 2002, 2004; Rotenberg *et al.*, 2005). The main aim of the present study was to examine the effect of various types of cations on the dielectric response of hydrated montmorillonite and kaolinite clay minerals over broad ranges of temperature (from −121ºC to +300ºC) and frequency (1 Hz−1 MHz), in order to obtain detailed information on the structure and the relaxation properties of water adsorbed by different hydration centers in the minerals. Preliminary results of the work were published by Vasilyeva *et al.* (2012a, 2012b).

EXPERIMENTAL

Materials

Two types of clay minerals were considered here: Oglanlinsky montmorillonite (from Turkmenistan) and Glukhovetsky kaolinite (from Ukraine). The clay minerals were treated in the Laboratory of Disperse Systems of the Institute of Colloid and Water Chemistry (Kiev, Ukraine) according to a procedure described by Tarasevich and Ovcharenko (1975, 1980). At first, impurities of other minerals, free oxides and hydroxides of Fe and Al, as well as other impurities and inclusions were removed from the raw clay. To obtain the purest samples possible, 3−5% aqueous suspensions of the clay mineral in question were mixed thoroughly until no agglomerates were visible and then kept at quiescence for ~30 min. A method of separating the solid clay particles from the liquid was chosen to elutriate the finest fraction: the precipitate was allowed to settle and the liquid settled or carefully decanted or filtered off through a siphon (Tarasevich and Ovcharenko, 1975, 1980). For kaolinite no other treatment was performed. Additional purification and centrifugation were required for montmorillonites. The purity (homogeneity) of the samples was checked by X-ray diffraction (XRD) and infrared (IR) spectroscopy. Then cleaned natural samples were treated 7−8 times with a 1 M NaCl solution at a solid:liquid (S:L) ratio of 1:20; each time the system was shaken, kept at quiescence for ~1 h, and then decanted. Afterward, the Na-saturated minerals were washed free of excess salts using distilled water. (resistivity not measured). Next, the clay minerals were treated 7−8 times in the same way with 1 N solutions of the required metal chlorides (KCl, $BaCl_2$, $CoCl_2$, $NiCl_2$) in the same S:L ratio. Finally, the samples were washed with distilled water until a negative reaction for chloride ion (with $AgNO_3$), dried for ~1 h at ~100ºC in air, then dried for ~1 h at ~50ºC in vacuum, and then stored at ambient air humidity until measured.

Table 1. Relative water content, *h*, in the samples studied.

Sample	*h* (%)
K-montmorillonite	13.7
Ni-montmorillonite	14.7
Co-montmorillonite	15.3
K-kaolinite	2.3
K,Ba-kaolinite	5.4

The relative water content, *h*, was determined by weighing the samples prior to and immediately after the dielectric measurements according to equation 1. The water content in a sample was calculated as a percent weight of the sample relative to the initial weight (Table 1):

$$h\ (\%) = 100 \times (m_{\text{initial}} - m_{\text{final}})/m_{\text{initial}} \quad (1)$$

Methods

The elemental composition of the samples was determined by X-ray fluorescence (XRF) analysis, using an energy dispersive X-ray spectrometer EDX 800HS2 (Shimadzu, Germany) (Table 2).

The morphology of the samples was examined using a field emission scanning electron microscope (FESEM) (Merlin, Carl Zeiss, Germany). Images of the morphology of some of the samples were collected using FESEM (Figure 1).

Powder XRD measurements were performed at room temperature using a D8 Advance diffractometer (Bruker AXS, Karlsruhe, Germany) with a goniometer radius of 217.5 mm, Göbel Mirror parallel-beam optics, 2º Sollers slits, and 0.2 mm receiving slit. Profile fitting, refinement of unit-cell parameters, and crystallite-size calculations were performed using the *EVA* software (Bruker, AXS). The crystallite sizes of monoclinic Ni- and Co-montmorillonite obtained were 251.5 Å and 199.1 Å, respectively; the crystallite size of triclinic kaolinite was

Table 2. Elemental compositions of the four studied samples.

Sample	Mg (%)	Al (%)	Si (%)	K (%)	Ti (%)	V (%)	Fe (%)	Ni (%)	Cu (%)	Zn (%)	Ba (%)
K-montmorillonite	1.8	11.3	74.7	8.7	0.4		2.9		0.2	0.1	
Ni-montmorillonite	2.4	13.6	71.5		0.5		3.1	8.5	0.4		
K-kaolinite		35.5	57.5	2.9	1.9	0.1	1.9			0.1	
K,Ba-kaolinite		37.0	57.3	1.0	2.3		1.2		0.1	0.1	1.0

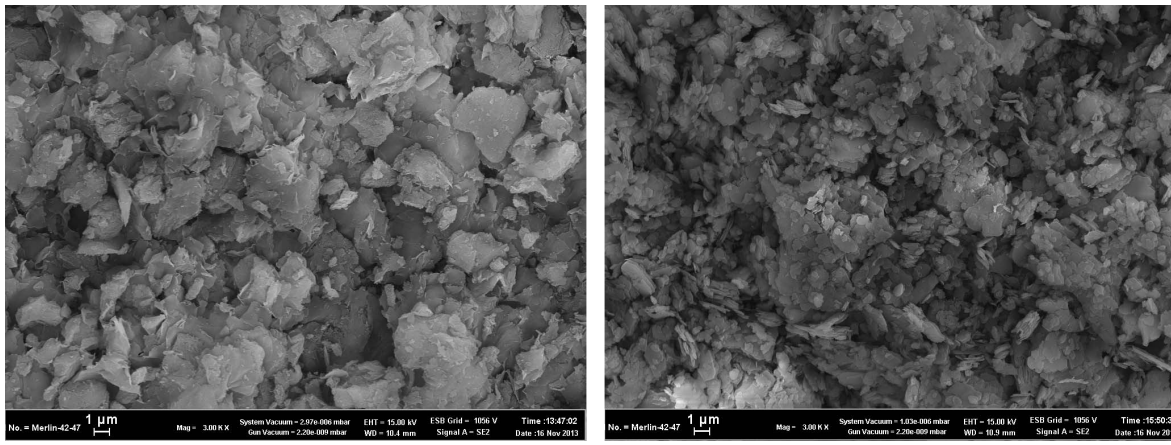

Figure 1. Electron micrographs of Ni-montmorillonite (left) and K-kaolinite (right).

382.7 Å. The kaolinite sample also contained some monoclinic sericite with a crystallite size of 409.1 Å.

Dielectric measurements in the frequency range of 1 Hz−1 MHz were performed using a BDS 80 Dielectric Spectrometer, based on an Alpha Impedance Analyzer (Novocontrol, Germany) with automatic temperature control by a Quatro Cryosystem, with a precision of 0.5ºC. The Alpha High Resolution Dielectric Analyzer can measure impedances from 10^{-2} to 10^{14} Ohms with a resolution in loss factor $\tan(\delta)<10^{-5}$ (Schaumburg, 1994; Kremer and Schoenhals, 2002). A voltage U_0 with a fixed frequency is applied to the cell which contains the material under investigation. The resulting current, I_0, has the same frequency but a phase shift between current and voltage described by the phase angle, φ. The ratio of U_0 and I_0 and the phase angle φ is determined from the electromagnetic and the geometric properties of the sample. The formulae for the voltage $U(t)$ and current $I(t)$ in their phasor notations can be represented conveniently by the following:

$$U(t) = U_0 \sin(\omega t) = I_m(U^* \exp(i\omega t))$$
$$I(t) = I_0 \sin(\omega t + \varphi) = I_m(I^* \exp(i\omega t)) \quad (2)$$

where $U^* = U' + iU'' = U_0$; $I^* = I' + iI''$; $I_0 = \sqrt{(I'^2 + I''^2)}$; $\tan(\varphi) = I''/I'$ where i is the imaginary unit and ω is the cyclic frequency. For a material with a linear electromagnetic response, the measured complex impedance of the sample capacitor is

$$Z^*(\omega) = Z' + iZ'' = U^*/I^* \quad (3)$$

This is related to the complex dielectric permittivity of the sample material by:

$$\varepsilon^*(\omega) = \varepsilon'(\omega) - i\varepsilon''(\omega) = \frac{1}{i\omega C_0}\frac{1}{Z^*(\omega)} \quad (4)$$

where $\varepsilon^*(\omega)$ is the complex dielectric permittivity, $\varepsilon'(\omega)$ and $\varepsilon''(\omega)$ are real and imaginary parts, respectively, of the $\varepsilon^*(\omega)$, and C_0 is the empty cell capacity.

A parallel plate capacitor with electrodes of 16 mm diameter and a spacing of ~0.5 mm between them was used. The study was carried out using the following protocol: Each of the samples was placed in the sample cell at room temperature and the measurements were then performed by quenching the samples down to −115ºC. Then the samples were measured upon heating to −58ºC with 3ºC intervals and then at intervals of 6ºC up to +300ºC. Afterward, annealing was performed inside the cryostat at 300ºC for 3 h. For montmorillonite with Co^{2+} as the exchangeable cation, the lowest temperature was −121ºC. After annealing, the samples were cooled to 25ºC and stored at this temperature in a nitrogen atmosphere until weighing. The montmorillonite samples with K^+ and Ni^{2+} as the exchangeable cations were also measured during the decrease in temperature down to 25ºC, in order to check the reversibility of the signal. All samples were weighed prior to and immediately after the experiments. The accuracy of the complex dielectric permittivity was better than 3%.

RESULTS

The complex non-Debye dielectric behavior of the clay minerals (Figures 2 and 3) can be described in terms of several distributed relaxation processes, separated by different frequency and temperature intervals, and marked as I−IV, according to their appearance during the heating experiment.

At low temperatures from −121ºC to −75ºC, the spectra of montmorillonites consisted of two relaxation processes marked I.1 and I.2, respectively (Figure 4). Both of these processes are characterized by a strong temperature dependence. In the kaolinite samples measured with the same protocol, the low-temperature process I was absent.

In the mid-temperature range from −90ºC to +150ºC, a relaxation process with a specific saddle-like shape and distinctive kink point was observed for mont-

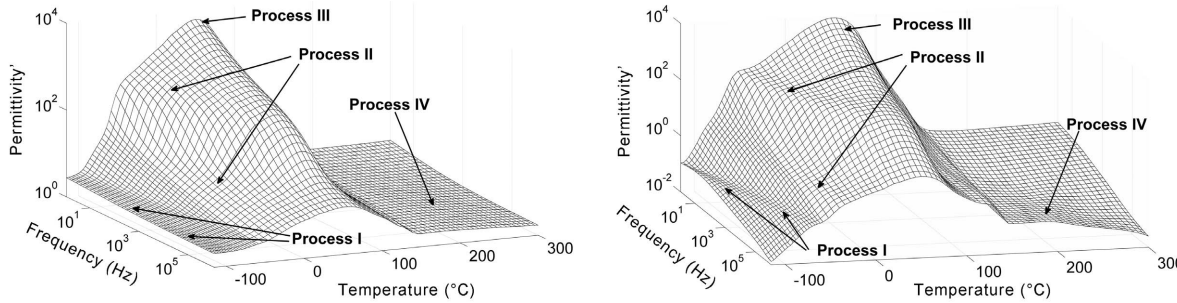

Figure 2. Typical 3D plots of the frequency and temperature dependences of the dielectric permittivity (left) and dielectric losses (right) for Ni-montmorillonite.

morillonite clay minerals at different frequency-temperature intervals simultaneously, while only one relaxation process, II, was observed in the case of kaolinite samples (Figure 5).

Relaxation process III was detected at temperatures from −50ºC to +70ºC for montmorillonites and from −70ºC to +40ºC for kaolinites. When viewed in an *ac*-conductivity presentation ($\sigma_{ac}(\omega)=(i\omega\varepsilon^*(\omega))$), typical *s*-like behavior of the low-frequency conductivity demonstrates the percolative nature of this process (Figure 6).

The amplitude of process III essentially decreased when the frequency increased and the maximum of the dielectric permittivity and losses *vs.* temperature had no temperature dependence (Figure 7) for all the clay-mineral samples.

The percolation temperature point, T_p, was determined by the maximum of the temperature dependence of the dielectric permittivity at the lowest measured frequency. The percolation temperature for montmorillonites was greater than for kaolinites (Table 3).

When the temperature rose above 100ºC, the samples became more electrically conductive. The relaxation processes were overlapped in the dielectric losses by a *dc*-conductivity. Some were even screened by the conductivity (Figure 8). A detailed investigation of the high-temperature region is the subject of a separate study.

After annealing the samples, the 3D plots of the dielectric losses *vs.* frequency and temperature changed dramatically (Figure 9). The relaxation processes previously observed in the mid-temperature window disappeared. Traces of the high-temperature spectrum were observed during the cooling measurement (Figures 8 and 9).

DISCUSSION

As shown above, all the samples lost some mass during the experiment. The clay-mineral samples demonstrated the absence of the dielectric relaxation processes at low- and mid-temperature levels after heating for extended periods of time at 300ºC (Figures 2, right and 9). As mentioned above, clay materials can adsorb water easily at their surfaces and around exchangeable cations, suggesting that water is the origin of the dielectric relaxation in these materials in the low- and mid-temperature intervals. Note that a similar conclusion was reported for porous glass systems (Gutina *et al.*, 2003).

From a structural point of view, the surface of the broken edges of the mineral layer has primary broken Al−O and Si−O bonds, resulting in polar sites. Water molecules form hydrogen bonds with surface oxygen atoms and exchangeable cations, to create new water structures very different from those of the bulk (Schoonheydt and Johnston, 2006; Sposito and Prost, 1982). In confined spaces or near interfaces, water forms distinctively layered structures with a restriction of water molecular mobility (Behnsen and Faulkner, 2011).

The minerals studied differ in their surface properties and exchangeable cations due to the differences in mineralogy and crystal structure, which lead to the variation in their affinity toward water.

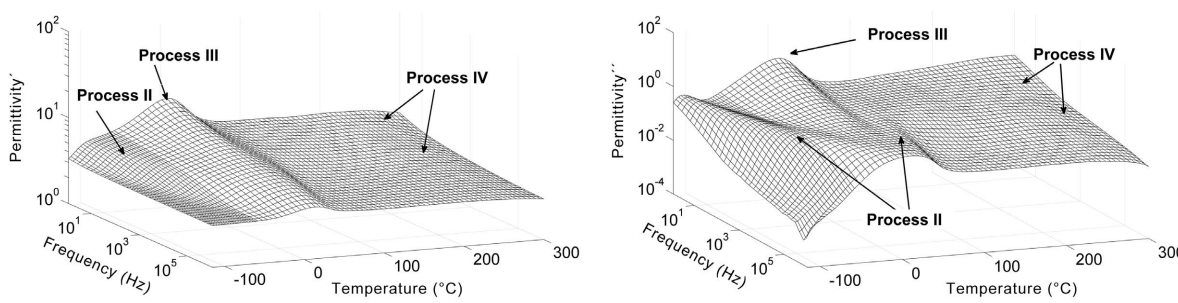

Figure 3. Typical 3D plots of the frequency and temperature dependences of the dielectric permittivity (left) and dielectric losses (right) for K-kaolinite.

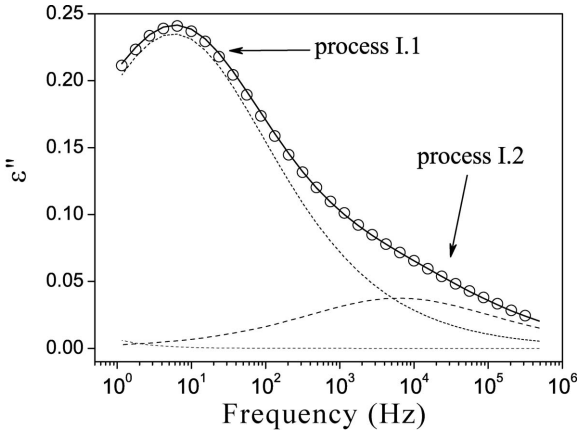

Figure 4. Measured dielectric losses *vs.* frequency at −121ºC for Co-montmorillonite. The dashed lines mark two Cole-Cole and Jonscher terms used for fitting the experimental data (open circles). The solid line is the superposition of the terms above.

The low-temperature dielectric relaxation

In the low-temperature interval (from −121ºC to −75ºC) the dielectric relaxation process (I) was observed for montmorillonites only. Therefore, this process must be associated with the relaxations of interlayer water molecules which are absent from kaolinites. Moreover, the dielectric spectrum of montmorillonites consists of two low-temperature relaxation processes (Figure 4).

Whenever water interacts with another dipolar or charge entity, a broadening of its Debye dielectric relaxation spectra occurs (Puzenko *et al.*, 2010; Levy *et al.*, 2012). In most cases this broadening can be described by the phenomenological Cole-Cole (CC) spectral function (Cole and Cole, 1941):

$$\varepsilon^*(\omega) = \varepsilon_\infty + \frac{\Delta\varepsilon}{1 + (i\omega\tau)^\alpha} \qquad (5)$$

where $\Delta\varepsilon = \varepsilon_s - \varepsilon_\infty$ is the dielectric strength of the relaxation process; ε_s and ε_∞ are the low- and high-frequency limits of the complex dielectric permittivity, respectively; τ is a characteristic relaxation time; and the exponent α is referred to as a measure of symmetrical broadening in the dielectric losses relaxation peak ($0<\alpha\leqslant 1$). A fruitful approach has been the application of fractional calculus to uncover a physical mechanism underlying the CC behavior in complex systems (Puzenko *et al.*, 2010; Levy *et al.*, 2012; Puzenko *et al.*, 2012). Taking into account that both low-temperature processes (I.1 and I.2) of montmorillonites are associated with the interaction of the water dipoles with the clay's mineral matrix, the quantitative analysis of the isothermal dielectric spectra uses a superposition of two CC functions, and an empirical Jonscher (J) term is convenient (Jonscher, 1996) (Figure 4):

$$\varepsilon^*(\omega) = \varepsilon_\infty + \sum_{j=1}^{2} \frac{\Delta\varepsilon_j}{1 + (i\omega\tau_j)^{\alpha_j}} + B \cdot (i\omega)^{n-1} \qquad (6)$$

where j denotes the number of the corresponding relaxation process and n is a Jonscher parameter for the high-frequency part of the respective relaxation process.

The temperature dependences of the relaxation times for the observed low-temperature processes demonstrated Arrhenius behavior (Figure 10). The activation energies of the low-temperature relaxation processes were then calculated (Table 4).

In montmorillonites the water molecules responsible for the low-temperature relaxations are located near the

Table 3. Values of the percolation temperature for the clay minerals studied.

Sample	T_p (ºC)
K-montmorillonite	40
Co-montmorillonite	40
Ni-montmorillonite	35
K-kaolinite	8
K,Ba-kaolinite	8

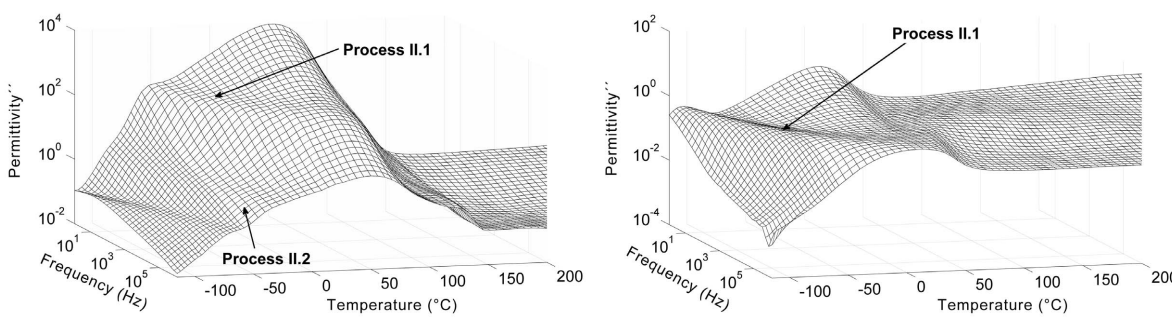

Figure 5. Typical 3D plots of the frequency and temperature behavior of the dielectric losses at a mid-temperature interval for Ni-montmorillonite (left) and K-kaolinite (right).

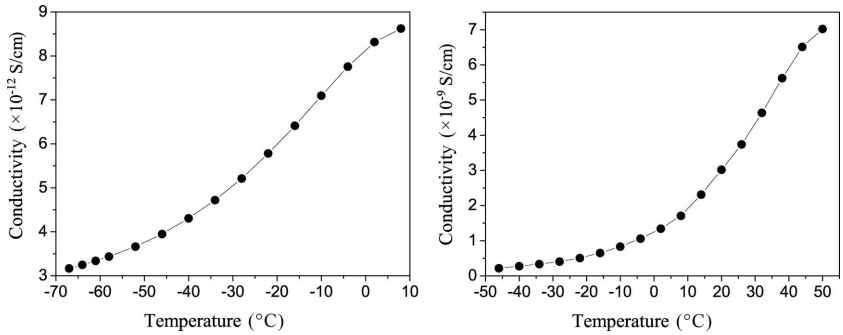

Figure 6. Temperature behavior of the low-frequency conductivity for Ni-montmorillonite (left) and K-kaolinite (right) in the mid-temperature region.

inner hydrophilic centers of interlayer channels (siloxane bonds and trapped cations) and around the interlayer cations (Salles *et al.*, 2008; Tarasevich and Ovcharenko, 1975). This is reflected by the formation of two types of structure in the low-temperature region. The slower relaxation process I.1 almost coincides with the low-temperature relaxation behavior of water adsorbed in porous silica glasses (Gutina *et al.*, 2003) (Figure 10). The activation-energy values of this process for montmorillonite samples are in the same range as that reported earlier for the porous glass materials (Gutina *et al.*, 2003; Ryabov *et al.*, 2001). The I.1 relaxation process was assumed, therefore, to correspond to ice-like water structures formed on the interior surface of interlayer channels. The second, faster, relaxation process I.2 reflects the water structures near the hydrated cations located in the interlayer channels. Thus, the nature of the hydration center plays an important role in the water dynamics of the adsorbed water in inorganic materials. Note that the type I.2 process in the glass materials (Gutina *et al.*, 2003) was not observed, but only one type of hydration center was observed in those materials. In both processes (I.1 and I.2) the activation energy depended on the type of interlayer cations and on the water content (Table 4). The detailed dielectric investigation of the formation of hydrated clusters and their structures as a function of the exchangeable cations and water content in the montmorillonites will be reported in a future study.

The mid-temperature relaxation process

Saddle-like relaxation processes were observed in the mid-temperature range from −90ºC to +150ºC for all the samples studied. Quantitative analysis of the mid-temperature relaxation process was performed based on the model described by Gutina *et al.* (2003) in which the

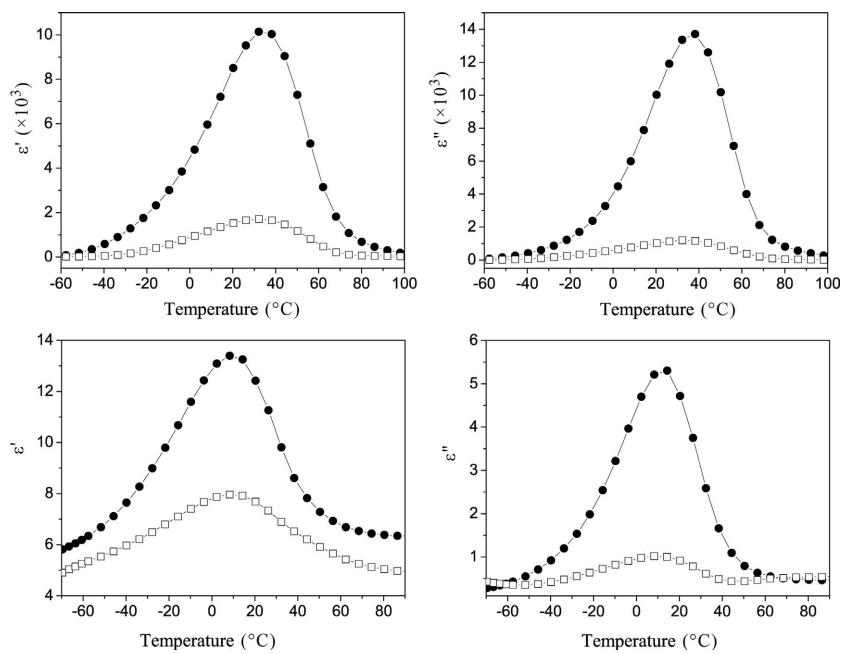

Figure 7. Typical temperature behavior of the dielectric permittivity (left) and dielectric losses (right) at percolation for Ni-montmorillonite (upper) and K-kaolinite (lower) at frequencies of 1 Hz (●) and 133 Hz (□).

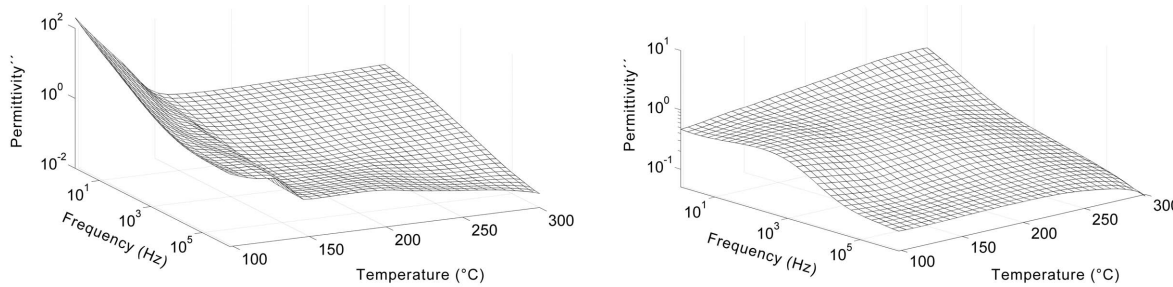

Figure 8. Typical 3D plots of the frequency and temperature dependences of the dielectric loss at high temperatures plotted for Ni-montmorillonite (left) and K-kaolinite (right).

act of relaxation was considered to be an occurrence of two simultaneous events: (1) reorientation of the molecule; and (2) the presence of a defect site in its vicinity. In the framework of the model, the temperature dependence of the relaxation time can be written in the form:

$$\tau = \tau_0 \exp\left\{\frac{H_a}{kT} + C\exp\left(-\frac{H_d}{kT}\right)\right\} \quad (7)$$

where H_a is the height of the potential barrier of the reorientation of water molecules; H_d is the energy of the defect formation; k is Boltzmann's constant and C is a number inversely proportional to the maximum possible defect concentration, η. The pre-exponential time constant, τ_0, can vary with temperature. The increase in temperature leads, on the one hand, to an increase in the probability of attaining sufficient energy to break the bonds between the reorienting molecule and its neighbors; or, on the other hand, it leads to a decrease in the probability of finding a defect in the vicinity of the moving molecule. The interplay of these two terms yields the appearance of the minimum observed in the temperature dependence of the relaxation time.

The temperature dependences of characteristic times corresponding to the frequency of the maximum of the relaxation loss peak (Figure 11) revealed that saddle-like process II.1 was observed in both kaolinites and montmorillonites (Figure 5), while an additional saddle-like process, II.2, was found only in the Co- and Ni-montmorillonites (Figure 11).

As discussed above, two main water-adsorption centers are present in the clay-mineral structure: (1) the basal oxygen atoms and cations trapped in hexagonal holes on the surfaces, and (2) exchangeable interlayer cations. Unlike the low-temperature processes I.1 and I.2 related to the relaxation of ice-like structures, the non-monotonous saddle-like processes, labeled II.1 and II.2 in Figure 5, can be assigned to the relaxation of confined water molecules (Gutina *et al.*, 2003; Feldman *et al.*, 2006). The two types of water structures characterized by different dynamics can coexist and that was recently confirmed by differential scanning calorimetry (DSC) experiments by Kozlowski (2011, 2012). The low-temperature exothermic peaks observed in the DSC measurements show that a significant amount of adsorbed water in clay minerals remains in an unfrozen state when cooling to −70ºC (Kozlowski, 2011, 2012), which confirms and follows the findings of Low *et al.* (1968a,b). The saddle-like relaxation process II.1 is clearly observed for both clay minerals (kaolinites and montmorillonites) and can be assigned to confined water between two interfaces (outer surface of powder granules on one side and air on the other). At the same time, no other saddle-like process II.2 was observed for kaolinites, which means that in the case of montmorillonites an additional source of confinement was present. The interlayer space of montmorillonite structures may have been the source of this extra second confinement. Exchangeable Co^{2+} and Ni^{2+} ions can form ion-water rigid structures in the interlayer gaps while the K^+ ion is known by its strong disordering effect on

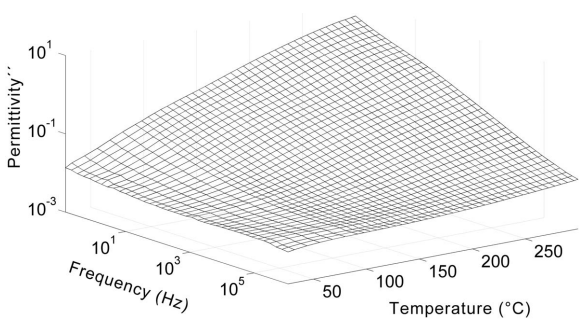

Figure 9. Typical 3D plot of the frequency and temperature dependences of the dielectric losses after annealing the sample for 3 h at 300ºC plotted for Ni-montmorillonite.

Table 4. Calculated activation energies, $E_{I.1}$ and $E_{I.2}$, of the low-temperature relaxation processes (I.1 and I.2) in the montmorillonite samples.

Sample	$E_{I.1}$ (kJ/mol)	$E_{I.2}$ (kJ/mol)
K-montmorillonite	35	31
Co-montmorillonite	49	25
Ni-montmorillonite	55	34

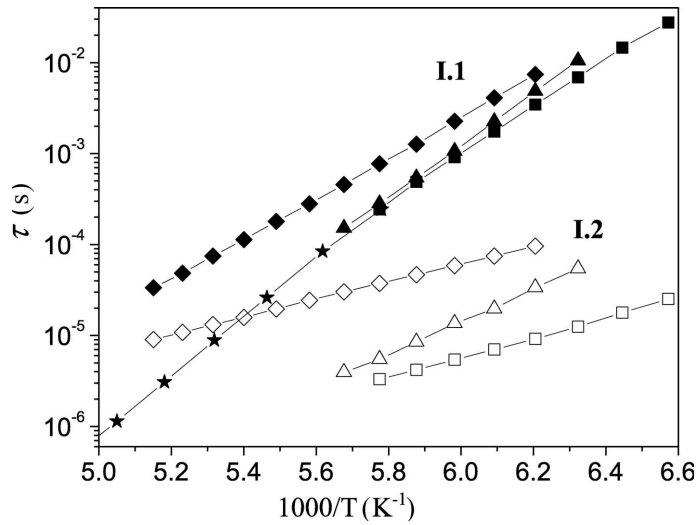

Figure 10. Temperature dependences of the relaxation times of the low-temperature processes for the montmorillonites (◆ K ◇; ■ Co □; ▲ Ni Δ). Filled symbols correspond to the I.1 process, open symbols to the I.2 process. Stars correspond to the temperature dependence of the relaxation time of the low-temperature process in glass (Gutina *et al.*, 2003).

unfrozen interlayer water. Indeed, the K^+ ion is characterized by hydrophobic properties ('negative hydration') at which the lifetime of water molecules to be in the immediate environment of the ion is less than that in the bulk solution (Krestov, 1991; Samoilov, 1957). Hence, the process II.2 is observed only for the Co- and Ni-montmorillonite samples.

The saddle-like process is shown (Figure 11) to depend heavily on the scale at which the relaxation takes place. Characteristic relaxation times for the process II.1 are slower than those for process II.2. The saddle-like behavior was fitted to equation 7 by means of a least-squares fit procedure. The fitting curves show good agreement with the proposed model (Figure 11). The resultant fit parameters are listed in Table 5.

The values of the activation energies H_{a1} and H_{d1} for the process II.1 for all clay minerals under study are in good agreement with the energies of molecular re-orientation and defect formation in confined water (Gutina *et al.*, 2003) but depend on the properties of individual ions. A more detailed investigation is required and may become a subject for further study.

The percolation process

At the mid-temperature range, all of the samples studied demonstrated typical percolation behavior of the

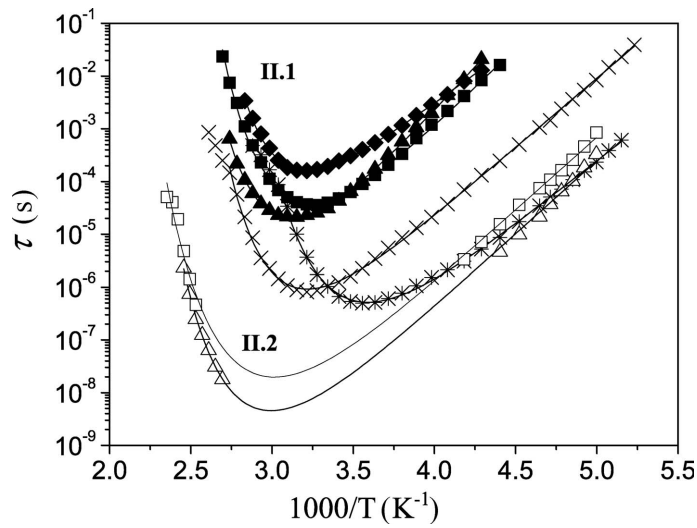

Figure 11. The temperature dependence of the characteristic times of the mid-temperature relaxation processes for montmorillonites (◆ K; □ Co ■; Δ Ni ▲) and kaolinites (* K; × K, Ba). Filled symbols for the montmorillonites correspond to the II.1 mid-temperature process and the open symbols to process II.2. The solid lines are the fitting curves according to equation 7.

Table 5. Fitting parameters obtained using equation 7.

Sample	Process II.1				Process II.2			
Fit parameter	τ_0 (s)	H_{a1} (kJ/mol)	H_{d1} (kJ/mol)	η	τ_0 (s)	H_{a2} (kJ/mol)	H_{d2} (kJ/mol)	η
K-montmorillonite	2×10^{-12}	43.2	36.0	7×10^{-7}	–	–	–	–
Co-montmorillonite	1×10^{-14}	53.2	41.6	1×10^{-7}	1×10^{-17}	53.0	24.0	7×10^{-5}
Ni-montmorillonite	1×10^{-14}	55.6	42.5	1×10^{-7}	3×10^{-18}	53.2	27.7	2×10^{-5}
K-kaolinite	2×10^{-16}	46.6	26.3	6×10^{-6}	–	–	–	–
K,Ba-kaolinite	6×10^{-16}	50.3	31.6	3×10^{-6}	–	–	–	–

dielectric spectrum as mentioned in the results section above. Such a process was previously associated with the percolation of an apparent dipole moment excitation, within a developed fractal structure of connected pores in a hydrated porous medium (Gutina *et al.*, 2003; Puzenko *et al.*, 1999). Note that the fractal geometry is a mathematical tool for dealing with the complex systems that have no characteristic length scale. Scale-invariant systems are usually characterized by a non-integer (so-called fractal) dimension (Bunde and Havlin, 1995). Similar to porous silica glasses, in the clay minerals the dipole excitation can also be linked to the self-diffusion along random paths of charge carriers within the channels. A transfer of the electric excitation along the developed fractal structure of the connected pores can be described by the normalized dipole correlation function (DCF), $\Psi(t)$. Note that a transfer of the electric excitation through the porous medium can occur even in the case of closed pores which are topologically not connected one to another. However, the distance between the neighboring pores filled with the dielectric or conductive material should be small enough to provide a 'physical' pore coupling *via* the electric interaction. A detailed description of the relaxation mechanism associated with an excitation transfer based on a regular fractal model was introduced by Feldman *et al.* (2006), where it was applied for the cooperative relaxation of ionic micro-emulsions at percolation. Based on percolation theory and the fractal characterization of the clay minerals, the DCF at the percolation threshold was represented by an asymptotic stretched-exponential term (Gutina *et al.*, 2003; Puzenko *et al.*, 1999):

$$\Psi(t) = \exp\left[-\left(\frac{t}{\tau_p}\right)^{D_p/3}\right] \quad (8)$$

where τ_p is an effective relaxation time and D_p is a fractal dimension of the media. In order to determine the value of D_p, the relaxation law (8) can be fitted to the experimental correlation functions. For this purpose the complex dielectric permittivity data were expressed in terms of the dipole correlation function using the Laplace transform.

Dielectric permittivity data were taken at the percolation threshold temperature for all studied samples. The DCF (Figure 12) values were then fitted to equation 8 after applying the Laplace transform. The D_p values obtained are presented in Table 6.

Note that the fractal dimension discussed here is the fractal dimension of the dipole excitation transfer paths connecting the different kinds of hydration centers located on the pore surface. The calculated fractal dimension of the pathways connecting the hydration centers lies between 1 and 2 (Table 6). Due to the relatively small water-content values of all the samples, the water molecules adsorbed by the materials are bound to these centers. The paths of the excitation transfer span the fractal pore surface and 'depict' the backbone of clusters formed by the pores on a scale that is larger than the characteristic distance between the hydration centers. Thus, a fractal dimension of the paths D_p approximates the real surface fractal dimension in the scale interval considered.

The values of the fractal dimension, D_p, of montmorillonites are a little larger than those of kaolinites (Table 6). This fact, as well as the increase in the percolation temperature values (Table 3) for montmorillonites, can be explained by the much more developed surface structure of this type of clay mineral due to the presence of interlayer spaces that are wide compared to kaolinites.

An additional method to quantify the structural information of the clay minerals using a fractal analysis of the SEM images was applied in the present study. Fractal analysis is a powerful approach for quantifying the structure of complex systems which exhibit a measure of self-similarity. Such similarity is usually reflected at different length scales, as discussed in detail

Table 6. Fractal dimensions of the montmorillonite and kaolinite samples.

Sample	D_p	D_f
K-montmorillonite	1.74	1.85
Co-montmorillonite	1.67	1.79
Ni-montmorillonite	1.75	1.80
K-kaolinite	1.48	1.66
K,Ba-kaolinite	1.30	1.81

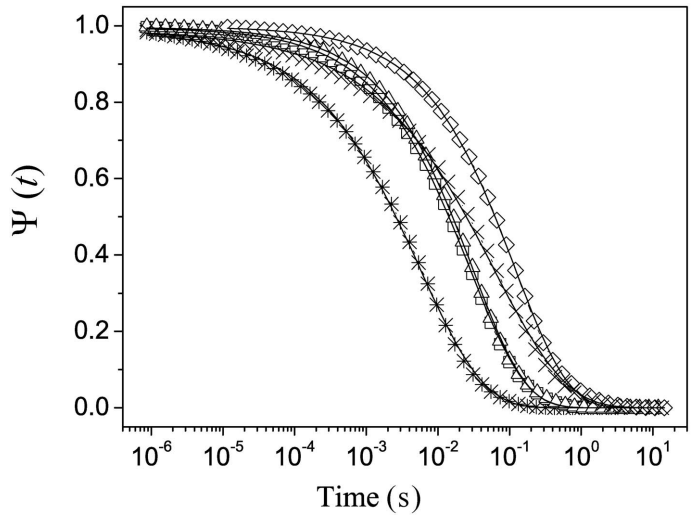

Figure 12. Semi-log plot of the dipole correlation function $\Psi(t)$ for montmorillonites ($\diamond$ K; $\square$ Co; Δ Ni) and kaolinites (* K; $\times$ K, Ba) at the temperatures corresponding to the percolation point. The solid line corresponds to the fit.

by Narine and Marangoni (1999) and by Tang and Marangoni (2006a, 2006b).

In an SEM image the grayscale intensity is proportional to the degree of electron scattering from the sample surface and particularly from areas of differing charge density. Consequently, an analysis of the fractality inherent in the image should reflect the underlying pathways of excitation. The fractality was calculated by counting the number of pixels, $S(N_j)$, in the image with a grayscale from 200 to 255, where the total number of pixels at level j of the recursive coarsening of the image is N_j. For simplicity, N_j was maintained as a power of 2. The detailed description of the calculations can be found in the study by Libster *et al.* (2008). The grayscale is presented below with the cutoff marked (Figure 13).

The image was coarsened by taking the average value of a moving square of four pixels, defining a reduced image. The count was then made again and the process repeated until the image size was too small. Mathematically, this is represented by the expression $N_j = 2^{2(l_{\max}-j)}$, where $l_{\max}$ is the maximum number of recursive stages for the image. A plot was then made in double log scale of the number of counts of white pixels against the image size in pixels.

Power-law behavior was observed and the slopes were calculated from the fitting, according to the relation

$$S(N_j) \propto N_j^D \quad (9)$$

where D is the boundary fractal dimension based on the SEM image depicting the different areas of charge density. This can then be related to the spatial fractal dimension, D_f, by the relationship $D_f = 3 - D$ (Wong and Cao, 1992). The results are summarized in Table 6. The agreement that is evident between these two separate methods of obtaining the spatial fractal dimension points toward the importance of the hydration centers. The D_f values are slightly greater than D_p, as expected, because they describe in more detail the surface structure rather than only the paths connecting the hydration centers.

CONCLUSIONS

Montmorillonites with exchangeable K^+, Co^{2+}, and Ni^{2+} cations and kaolinites with exchangeable K^+ and Ba^{2+} cations were examined by means of Broadband Dielectric Spectroscopy over wide temperature (−121ºC to +300ºC) and frequency (1 Hz−1 MHz) ranges. The rich dielectric spectra can be described in terms of four distributed relaxation processes. Over the low-temperature interval the two Cole-Cole-type dielectric relaxation processes (I.1 and I.2) were observed for montmorillonites only, associated with the interlayer ice-like water molecule relaxations linked to the two types of hydration centers that are located at the hydrophilic centers of interlayer channels (siloxane bonds and trapped cations) and around the interlayer cations.

Figure 13. The gray scale with divisions every eight shades of gray. (The gray scale from white to black, usually varies in 255 shades of gray. For clarity in the figure each division represents the average of eight shades of gray). The cut-off used for the analysis is marked.

The saddle-like behavior of water adsorbed in the mid-temperature interval has been ascribed to the relaxation of confined water molecules (process II.1). While an additional saddle-like process (II.2) related to the interlayer space confinement was observed for Co- and Ni-montmorillonites only. The absence of the II.2 process for K-montmorillonite is explained by strong disordering effect of the K^+ ion ('negative hydration').

The third relaxation process, occurring in both clay minerals, is associated with percolation of the electric excitation (the self-diffusion of the charge carriers) within the developed fractal structure of connected pores on the outer surface of the granules. The fractal dimensions of the electric excitation paths coming along the pore surface from one hydration center to another are between 1 and 2, consistent with fractal dimension calculated from micrographs for all the samples studied.

ACKNOWLEDGMENTS

The authors thank Prof. I.A. Litvinov and Dr I. Kh. Rizvanov of the A.E. Arbuzov Institute of Organic and Physical Chemistry of the Kazan Scientific Center of Russian Academy of Sciences for their XRF study of aluminosilicates. The authors gratefully acknowledge Dr Yu.N. Osin from the Institute of Geology and Petroleum Technologies of the Kazan Federal University for SEM measurements. The authors also thank Dr V. Uvarov of the H. M. Krueger Center for Nanoscience and Nanotechnology of the Hebrew University of Jerusalem for XRD analyses of the samples. The Israeli authors acknowledge the Israel Science Foundation (ISF), grant number 465/11, for the financial support of the research.

The work was performed in accordance with the Russian Government Program of Competitive Growth of Kazan Federal University.

REFERENCES

Behnsen, J. and Faulkner, D.R. (2011) Water and argon permeability of phyllosilicate powders under medium to high pressure. *Journal of Geophysical Research*, **116**, B12203.

Bunde, A. and Havlin, S. (1995) *Fractals in Science*. Springer-Verlag, Berlin, Heidelberg, New York.

Calvet, R. (1975) Dielectric properties of montmorillonites saturated by bivalent cations. *Clays and Clay Minerals*, **23**, 257–265.

Cole, K.S. and Cole, R.H. (1941) Dispersion and absorption in dielectrics. I. Alternating current characteristics. *Journal of Chemical Physics*, **9**, 341–351.

Feldman, Y., Puzenko, A., and Ryabov, Ya. (2006) Dielectric relaxation phenomena in complex materials. Pp. 1–125 in: *Fractals, Diffusion, and Relaxation in Disordered Complex Systems: a Special Volume of Advances in Chemical Physics* (Y.P. Kalmykov, W.T. Coffey, and S.A. Rice, editors). Volume **133**, part A, Wiley, New York.

Greg, S.J. and Sing, K.S.W. (1967) *Adsorption, Specific Area and Porosity*. Academic Press, London, New York, 303 pp.

Gupta, S.S. and Bhattacharyya, K.G. (2012) Adsorption of heavy metals on kaolinite and montmorillonite: a review. *Physical Chemistry Chemical Physics*, **14**, 6698–6723.

Gutina, A., Antropova, T., Rysiakiewicz-Pasek, E., Virnik, K., and Feldman, Yu. (2003) Dielectric relaxation in porous glasses. *Microporous and Mesoporous Materials*, **58**, 237–254.

Hall, P.G. and Rose, M.A. (1978) Dielectric properties of water adsorbed by kaolinite clays. *Journal of Chemical Society, Faraday Transactions 1*, **74**, 1221–1233.

Hoekstra, P. and Doyle, W.T. (1971) Dielectric relaxation of surface adsorbed water. *Journal of Colloid and Interface Science*, **36**, 513–521.

Ishida, T., Makino, T., and Wang, C. (2000) Dielectric-relaxation spectroscopy of kaolinite, montmorillonite, allophane, and imogolite under moist conditions. *Clays and Clay Minerals*, **48**, 75–84.

Jonscher, A.K. (1996) *Universal Relaxation Law*. Chelsea Dielectrics Press, London, 415 pp.

Kaviratna, P.D., Pinnavaia, T.J., and Schroeder, P.A. (1996) Dielectric properties of smectite clays. *Journal of Physics and Chemistry of Solids*, **57**, 1897–1906.

Kiselev, A.V. (1986) *Intermolecular Interactions in Adsorption and Chromatography*. Vyshzhaya shkola, Moscow (in Russian), 360 pp.

Kozlowski, T. (2011) Low temperature exothermic effects on cooling of homoionic clays. *Cold Regions Science and Technology*, **68**, 139–149.

Kozlowski, T. (2012) Modulated Differential Scanning Calorimetry (MDSC) studies on low-temperature freezing of water adsorbed on clays, apparent specific heat of soil water and specific heat of dry soil. *Cold Regions Science and Technology*, **78**, 89–96.

Kremer, F. and Schoenhals, A. (2002) *Broadband Dielectric Spectroscopy*. Springer-Verlag, Berlin, Heidelberg, New York, 729 pp.

Krestov, G.A. (1991) *Thermodynamics of Solvation: Solution and Dissolution, Ions and Solvents, Structure and Energetics*. Horwood, New York, 570 pp.

Levy, E., Puzenko, A., Kaatze, U., Ben Ishai, P., and Feldman, Yu. (2012) Dielectric spectra broadening as the signature of dipole-matrix interaction. II. Water in ionic solutions. *Journal of Chemical Physics*, **136**, 114503.

Libster, D., Ben Ishai, P., Aserin, A., Shoham, G., and Garti, N. (2008) Microscopic to mesoscopic properties of lyotropic reverse hexagonal liquid crystals. *Langmuir*, **24**, 2118–2127.

Lockhart, N.C. (1980a) Electrical properties and the surface characteristics and structure of clays. I. Swelling clays. *Journal of Colloid and Interface Science*, **74**, 509–519.

Lockhart, N.C. (1980b) Electrical properties and the surface characteristics and structure of clays. II. Kaolinite – a nonswelling clay. *Journal of Colloid and Interface Science*, **74**, 520–529.

Logsdon, S.D. and Laird, D.A. (2002) Dielectric spectra of bound water in hydrated Ca-smectite. *Journal of Non-Crystalline Solids*, **305**, 243–246.

Logsdon, S.D. and Laird, D.A. (2004) Electrical conductivity spectra of smectites as influenced by saturating cation and humidity. *Clays and Clay Minerals*, **52**, 411–420.

Low, P.F., Anderson, D.M., and Hoekstra, P. (1968a) Thermodynamic relationships for soils at or below the freezing point. I. Freezing point depression and heat capacity. *Water Resources Research*, **4**, 379–394.

Low, P.F., Hoekstra, P., and Anderson, D.M. (1968b) Thermodynamic relationships for soils at or below the freezing point. II. Effects of temperature and pressure on unfrozen soil water. *Water Resources Research*, **4**, 541–544

Mamy, J. (1968) Recherches sur l'hydration de la montmorillonite: propriétés diélectriques et structure du film d'eau. *Annales Agronomiques*, **19**, 175–246.

Narine, S.S. and Marangoni, A.G. (1999) Fractal nature of fat crystal networks. *Physical Review E*, **59**, 1908–1920.

Puzenko, A., Kozlovich, N., Gutina, A., and Feldman, Yu.

(1999) Determination of dimensions of pore fractals and porosity of silica glasses from the dielectric dispersion at percolation. *Physical Review B*, **60**, 14348–14359.

Puzenko, A., Ben Ishai, P., and Feldman, Y. (2010) Cole-Cole broadening and strange kinetics. *Physical Review Letters*, **105**, 037601-4.

Puzenko, A., Levy, E., Shendrik, A., Talary, Mark S., Caduff, A., and Feldman Y. (2012) Dielectric spectra broadening as a signature for dipole-matrix interaction. III. Water in adenosine monophosphate/adenosine-5-triphosphate solutions. *Journal of Chemical Physics*, **137**, 194502.

Raythatha, R. and Sen, P.N. (1986) Dielectric properties of clay suspensions in MHz to GHz range. *Journal of Colloid and Interface Science*, **109**, 301–309.

Rotenberg, B., Cadéne, A., Dufrêche, J.-F., Durand-Vidal, S., Badot, J.-C., and Turq, P. (2005) An analytical model for probing ion dynamics in clays with broadband dielectric spectroscopy. *Journal of Physical Chemistry B*, **109**, 15548–15557.

Ryabov, Y., Gutina, A., Arkhipov, V., and Feldman, Yu. (2001) Dielectric relaxation phenomena of water absorbed in porous glasses. *Journal of Physical Chemistry B*, **105**, 1845–1850.

Salles, F., Devautour-Vinot, S., Bildstein, O., Jullien, M., Maurin, G., Giuntini, J.-C., Douillard, J.-M., and Van Damme, H. (2008) Ionic mobility and hydration energies in montmorillonite clay. *Journal of Physical Chemistry C*, **112**, 14001–14009.

Saltas, V., Vallianatos, F., Soupios, P., Makris, J.P., and Triantisc, D. (2007) Dielectric and conductivity measurements as proxy method to monitor contamination in sandstone. *Journal of Hazardous Materials*, **142**, 520–525.

Samoilov, O.Ya. (1957) *The Structure of Aqueous Electrolyte Solutions and the Ion Hydration*. Akademie Nauk SSSR, Moscow (in Russian), 192 pp.

Schaumburg, G. (1994) Overview: Modern measurement techniques in Broadband Dielectric Spectroscopy. *Dielectrics Newsletter*, March issue, 4–7.

Schoonheydt, R. and Johnston, C. (2006) Surface and interface chemistry of clay minerals. Pp. 87–114 in: *Handbook of Clay Science* (F. Bergaya, B. Theng, and G. Lagaly, editors). Volume **1**, Elsevier, New York.

Spanoudaki, A., Albela, B., Bonneviot, L., and Peyrard, M. (2005) The dynamics of water in nanoporous silica studied by dielectric spectroscopy. *The European Physical Journal E: Soft Matter and Biological Physics*, **17**, 21–27.

Sposito, G. and Prost, R. (1982) Structure of water adsorbed on smectites. *Chemical Reviews*, **82**, 553–573.

Tang, D. and Marangoni, A.G. (2006a) 3D fractal dimension of fat crystal networks. *Chemical Physics Letters*, **433**, 248–252.

Tang, D. and Marangoni, A.G. (2006b) Microstructure and fractal analysis of fat crystal networks. *Journal of the American Oil Chemists' Society*, **83**, 377–388.

Tarasevich, Yu.I. (1988) *Structure and Surface Chemistry of Layer Silicates*. Naukova Dumka, Kiev (in Russian), 248 pp.

Tarasevich, Yu.I. and Ovcharenko, F.D. (1975) *Adsorption on Clayey Minerals*. Naukova Dumka, Kiev (in Russian), 351 pp.

Tarasevich, Yu.I. and Ovcharenko, F.D. (1978) A study of the nature of the active centers on the surface of layer silicates. Pp. 138–141 in: *Adsorbents, their Preparation, Properties, and Applications* (in Russian), Nauka, Leningrad.

Tarasevich, Yu.I. and Ovcharenko, F.D. (1980) *Adsorption sur des Minéreaux Argileux*. Institut Français du Pétrole, Rueil Malmaison, Paris, 449 pp.

Vasilyeva, M.A., Gusev, Yu.A., and Shtyrlin, V.G. (2012a) Two types of adsorbed water in natural montmorillonites at low temperatures by dielectric spectroscopy. *Journal of Physics: Conference Series*, **394**, 012027.

Vasilyeva, M.A., Gusev, Yu.A., and Shtyrlin, V.G. (2012b) Differences in behaviour of adsorbed water in kaolinites and montmorillonites in temperature range from −90ºC to +140ºC by dielectric spectroscopy. *Journal of Physics: Conference Series*, **394**, 012028.

Volzone, C., Thompson, J.G., Melnitchenko, A., Ortiga, J., and Palethorpe, S.R. (1999) Selective gas adsorption by amorphous clay-mineral derivatives. *Clays and Clay Minerals*, **47**, 647–657.

Wander, M.C.F. and Clark, A.E. (2008) Structural and dielectric properties of quartz–water interfaces. *Journal of Physical Chemistry C*, **112**, 19986–19994.

Wong, P. and Cao, Q. (1992) Correlation function and structure factor for a mass fractal bounded by a surface fractal. *Physical Review B*, **45**, 7627–7632.

(*Received 28 August 2013; revised 6 February 2014; Ms. 806; AE: M. Plötze*)

Clays and Clay Minerals, Vol. 62, No. 1, 74–78, 2014.

In Memoriam
Blair F. Jones (1934–2014)

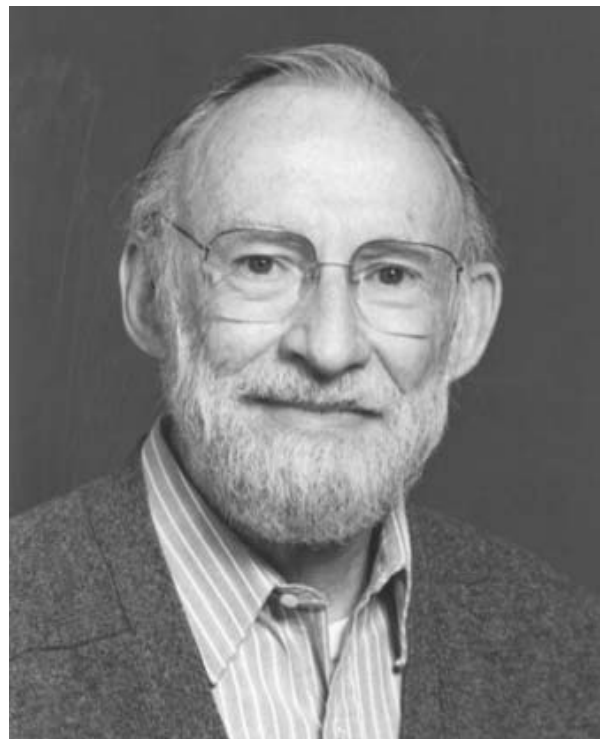

Blair F. Jones, our friend, colleague, and mentor, died on Sunday, March 30, 2014, at peace and surrounded by his family, following a stroke. Blair was a long-time member of The Clay Minerals Society, dating back to the late 1960s, and was a Sustaining Member. In addition to serving on numerous committees over the decades, he was also President of the Society in 2002.

Blair is widely recognized as a pioneer in the interdisciplinary investigation of earth-surface processes in mineralogy and geochemistry. Blair was one of the leading forces in developing and applying the first numerical codes to model chemical thermodynamics in surface and groundwater systems. Blair continued to contribute to these efforts over the years, and the WATEQ code that he helped develop lies at the heart of today's numerical modeling software such as PHREEQC. These codes are used by investigators worldwide to describe the speciation and thermodynamic state of fluids with respect to solid phases. After his profound initial contributions, Blair continued to use numerical modeling approaches in other areas, such as SNORM, the 'Salt Norm,' which calculates the normative salt assemblage produced by a water composition if evaporated to dryness; and SPREADBAL, a tool for constraining mass-balance calculations in weathering reactions.

These contributions are particularly valuable because Blair was far from simply a 'number-cruncher' – his extensive field experience and his intuitive grasp of the complexities of field conditions informed his numerical work. He always reminded us of the power as well as the limitations of numerical modeling. Throughout the community, Blair's colleagues have fond memories of mapping, sampling expeditions, and field trips to outcrops, closed basins, and mudflats around the world.

Blair was fondly known as the 'Brine Monster' because of his fascination with salty mud puddles. Blair made major contributions to our understanding of numerous saline systems around the world, including the Great Salt Lake, the Murray Basin in Australia, the Saline Valley of California, the Department of Energy's Waste Isolation Pilot Plant in New Mexico, Lake Abert in Oregon, and Lake Magadi in Kenya. Blair's work in these and other settings was central to the development

DOI: 10.1346/CCMN.2014.0620107

of the 'Eugster-Hardie' model of brine evolution, based on the principle of the chemical divide. This idea lies at the heart of thermodynamic modeling of brine geochemistry, and it has also impacted applications such as engineered salts, water-quality modeling, and the development of geothermal circulatory technologies.

In the realm of clay science, Blair made fundamental contributions to our understanding of the alteration of volcanic glass, the characterization of poorly crystalline clays, and silicate diagenesis in saline, alkaline environments. His work on these phases grew out of his aqueous geochemical studies of the evaporative evolution of brines. Blair demonstrated the importance of authigenic Mg-rich silicate phases in affecting brine evolution, particularly hydrous talc-like phases ('kerolite'), sepiolite and palygorskite-group minerals, and Mg-rich smectites. Blair's work was instrumental in demonstrating the potential for using thermodynamic approaches to modeling phase behavior in earth-surface environments, despite the biogeochemical complexities, poor crystallinity, and metastability or instability of solid phases.

Later in his career, Blair applied his expertise to understanding the behaviors of transition metals in the human brain. His cutting-edge contributions led to greater understanding of the role of metals in promoting or modulating cellular damage. In these efforts Blair spearheaded using national research infrastructure such as the Brookhaven National Laboratory synchrotron light source.

Blair selflessly and tirelessly served the discipline and the community with distinction as a leading senior scientist. At the United States Geological Survey, he served as the Water Resource Division's first Geochemistry Research Advisor for the National Research Program. He was awarded the Department of the Interior's Meritorious Service Award in 1981 and the Distinguished Service Award in 1986. Blair was recognized as a Fellow of the Geological Society of America and the Mineralogical Society of America, and was the Ingerson International Lecturer of the International Association of Geochemistry in 2002. In addition to his service to The Clay Minerals Society, he served on countless committees in public and society service. His leadership and mentorship touched countless people throughout the earth sciences and beyond. He was also known to quietly tutor disadvantaged urban youth in math and science, to volunteer, and to support many charities in his community.

Blair was born on the South Side of Chicago. He received his BA from Beloit College in 1955, and his Ph.D. from Johns Hopkins University in 1963. He was preceded in death by his first wife, Betty Foster Jones, who was mourned in the pages of The Clay Minerals Society Newsletter in 1993, the year of her death. Blair died the husband of Jane, father of Geoffrey and Sheryl, step-father of Susan, grandfather of Bryan, and brother of Ed. Blair's life, generosity of spirit, epic sense of humor, love of good wine and music, and his great many achievements were celebrated by friends and family at St. John's Episcopal Church in Chevy Chase, Maryland, on April 12, 2014.

Daniel M. Deocampo
Chair of the Department of Geosciences
Georgia State University
Atlanta, Georgia
USA

In Memoriam
Richard Warren Berry (1933–2014)

Dr. Richard (Dick) W. Berry, Professor Emeritus of Geological Sciences at San Diego State University, passed away suddenly at his home in Avon, Connecticut, on March 10, 2014, in the company of his wife, JoAnne. Dick had undergone heart surgery back in November 2013 but had been quite upbeat and positive about the results and seemingly on the mend. Around Valentine's Day he reported feeling great and was putting the final coat of polyurethane on a cabinet of drawers for his mineral specimens.

Dick enjoyed a rich academic career focused on clay mineralogy and was a long-time member and valued contributor to The Clay Minerals Society. He displayed bold insight in inviting the then 92 year-old Nobel Laureate Dr Linus Pauling to be the featured speaker at the Society's 1993 annual meeting in San Diego where Pauling delivered his last public lecture (available on DVD from the Society's office). This is a treasured moment in the Society's history, which traces its roots to Pauling's initial crystal-structure discoveries at Caltech.

Dick was also a dedicated educator determined to make a difference in students' lives. Amongst his many accomplishments he was the mainstay of the Department's mineralogy program for many years, developed a geology course for pre-service elementary school teachers, engaged in development of a new Science framework for public schools in 2000, and was instrumental in the acquisition of a new state-of-the art X-ray diffractometer in the Department in 2001.

Dick was born June 21, 1933, in Quincy, Massachusetts, to his father George – a naval architect – and mother Blanche. He received a BA in 1955 in Mining Engineering from Layfayette College in Easton, Pennsylvania, when it was still closely affiliated with the Presbyterian Church. He went on to receive his MS (Exploration Geophysics 1957) and Ph.D. (Geochemistry and Clay Mineralogy 1963) degrees from Washington University in St. Louis, Missouri, arriving in 1961 at SDSU as a faculty member. The ensuing 40 years, before his retirement from the University in 2001, were a time of growth, intellectually as a professor and scientific researcher, and spiritually as a Christian active in the Presbytery. Following his retirement in 2001 he continued to serve SDSU in an Emeritus capacity before moving back to Connecticut to be closer to family.

Dick valued family and church, enjoyed traveling, and contributing to the community. He is survived by three sons (one of them a Presbyterian Pastor) and two step-daughters. His wife, JoAnne, and he shared 11 grandchildren. He will be missed.

David Kimbrough
Department Chair, Geological Sciences
San Diego State University
California
USA

In Memoriam
José Fripiat (1923–2014)

Professor José J. Fripiat, the prominent scientist and teacher who contributed so much to the surface and solid state science of minerals and that of clay minerals in particular, died on February 17, 2014, in Mexico City at the age of 90.

Our community has lost one of the founders of modern clay science and one of the most versatile materials scientists ever.

Born in summer 1923, Prof. José J. Fripiat graduated in 1946 from the Université Catholique de Louvain (UCL), Belgium, in chemistry. His MS thesis was on the relationship between polarizability and molecular spring constants, illustrating at an early stage his lasting interest in physical chemistry, spectroscopy, and fundamental questions. Yet, it was not in a traditional university environment that he began his research career. The world was still in the final years of colonialism and he was offered the opportunity to join the National Institute for Agronomic Studies in what was then the Belgian Congo. We are lucky that he availed of this opportunity for it was there, in one of the hotspots of tropical agronomy, that he discovered the world of soil minerals and could express for the first time his talent for scientific excellence while addressing practical problems. Understanding and improving the mechanisms of soil fertility was a challenge where he felt physical chemistry would be helpful.

Fripiat returned to Belgium in 1949, where, after a doctorate degree obtained for his work on infrared spectroscopy, two awards by the Royal Academy of Sciences of Belgium, and a postdoctoral year with Peter Debye, then at Cornell University, he was appointed as assistant professor in physical chemistry of soils at the Agronomic Institute of UCL. Then began an incredibly productive period of over 20 years, during which the young laboratory of soil physical chemistry, hosting the first transmission electron microscope in Belgium in 1952, became the world-renowned Laboratoire de Physico-chimie Minérale. He was promoted to associate professor (‘chargé de cours’) in 1953 and full professor (‘Professeur Ordinaire’) at the Faculty of Agronomy in 1959. Fripiat authored and co-authored more than 200 scholarly papers during this period, applying surface chemical and spectroscopic methods to the study of clays and related silicates or oxides not only for soil science problems but also for catalysis, petroleum geochemistry, cement chemistry, glass science, and even the origin of life. Groundbreaking results were obtained in all these fields. Quite naturally in view of his past interests, infrared spectroscopy was the first spectroscopic method used intensively, in parallel with what was happening in Spain, the UK, and in the US. This was soon followed by nuclear magnetic resonance (NMR), a technique which at that time was still very

much in its infancy. Dielectric spectroscopy was used in parallel. Electron spectroscopy for chemical analysis (ESCA or, more precisely, X-ray photoelectron spectroscopy, XPS) was applied to clay science and catalysis a few years later. The mobility of protons in clay crystal networks, the mobility of protons in adsorbed layers at room or at high temperature (water, alcohol, ammonia), the adsorption and the reactivity of amino acids and peptides adsorbed on clay minerals, the use of clays for the synthesis of what would now be called hybrid or nanocomposite materials, the surface chemistry of silica and silico-alumina, and the role of clays in petroleum genesis and migration or in the origin of life were the main topics on which he concentrated his interests during those years.

In 1972, while still professor at UCL, Fripiat accepted a professor position at the University of Illinois, sharing his time and energy between Leuven and Urbana-Champaign. Two years later, in 1974, he was offered the opportunity to become Director of the 'Centre de Recherche sur les Solides à Organisation Cristalline Imparfaite' (CRSOCI) of the French 'Centre National de la Recherche Scientifique' (CNRS) in Orléans, France, which he accepted. Founded by Jacques Méring, the CRSOCI was a worldwide reference laboratory for the structural science of clays and carbons. Under the leadership of Prof. Fripiat, the center also became a standard for physical chemistry. Those were years of extensive collaboration with the late Maribel Cruz-Cumplido, then his wife, who died prematurely in 1981. In the context of a growing interest in renewable energies and solar energy in particular, he initiated work on the photochemistry and the photocatalytic properties of dye molecules and organometallic complexes adsorbed on clay minerals, while still going on with research on water in clay minerals and on organoclays. This work led to one of the very few photochemical systems showing some activity for the decomposition of water in sunlight. Prof. Fripiat was one of the three final nominees for the International BP prize for energy in 1982, among eighty selected candidates. In a different field, applying the recently developed theory of fractals, he proposed a theoretical model for multilayer adsorption on rough surfaces, which is an elegant extension of the celebrated BET theory for multilayer adsorption and surface-area measurements. It was also in Orléans that he started working on the so-called hydrogen bronzes of transition metal oxides.

This is the point where most of us would have enjoyed retirement or emeritus status, but this was way too early for José Fripiat. In 1986 he became distinguished professor of chemistry at the University of Wisconsin, Milwaukee (UWM), and started a second career in the field of materials for catalysis. Twelve more years of intense work passed, devoted to the synthesis and the structural or surface chemical study of zeolites and mesoporous solids, mainly by high-resolution NMR spectroscopy.

That was not the end of the story – Fripiat retired from UWM and chose to continue in the same field at the Mexican Institute of Petroleum in Mexico City, working in collaboration with Graciela Pacheco at the University of Mexico who became his wife.

In early 2014 Prof. Fripiat was still looking forward to beginning research on mineral–bitumen interfaces.

Professor Fripiat was the author of more than 300 scientific papers and two books. He received numerous awards, among which was the Francqui prize, the highest scientific award in Belgium. He was a member of the Belgian Academy of Sciences and foreign member of the French Academy of Agriculture. He was President of the Association Internationale Pour l'Etude des Argiles (AIPEA) from 1973 to 1975 and was made AIPEA Fellow in 2005.

A demanding but also generous and inspiring teacher, mentor, and leader, a man of heart and action, Professor Fripiat was an exceptionally strong personality who has left his imprint on generations of colleagues and students all over the world. Looking for honors was never his motivation. Doing good and useful science has always been his passionate driving force. His work will resonate for many years.

José Fripiat is survived by his wife Graciela, three sons, three daughters, sons-in-law, daughters-in-law, and fifty grandchildren and greatgrandchildren. We express our deepest sympathy to them and to all his relatives and friends.

Henri van Damme and Faïza Bergaya
(edited version of original which was published in *Applied Clay Science*. Reprinted with permission.)